Chapter V

Dynamic Contact Lines and Angles

G. Smedley and D. Coles
Graduate Aeronautical Laboratory
California Institute of Technology
Mail code: 205-45
Pasadena, CA 91125
U.S.A.

Abstract

The work reported here involves an experimental study of the dynamic contact line, with the intention of making accurate measurements of the contact angle. The contact angle is a critical parameter in the consideration of liquid behavior. A technique based on laser light refraction was developed to measure it. Dynamic contact line experiments were conducted at various velocities, both advancing and receding, using an immiscible liquid pair (nonane/formamide) in contact with glass. An interesting binary behavior of the interface is found that is dependent upon the liquid that is first in contact with the glass plate. Capillary numbers from 4.2×10^{-4} to 8.4×10^{-3} were studied (Contact-line velocities from 0.05 to 1.00 mm/sec).

1 Introduction

The work reported here involves an experimental study of the dynamic contact line, with the intention of making accurate measurements of the contact angle. The literature on this topic reveals an area of research that is plagued by problems of contact angle sensitivity and lack of repeatability (Bikerman 1970, Dussan 1979). The contact angle depends on surface cleanliness, surface roughness, temperature, liquid purity, and other variables, including velocity. The work has involved the design of an instrument for the specific task of measuring the velocity dependence of the contact angle. The apparatus uses refraction of laser light to determine contact angles at the intersection with a transparent solid of the interface between two transparent immiscible liquids.

The technique used is based on the refraction of light at liquid-vapor or liquid-liquid interfaces. In principle, a plate partially immersed in a liquid distorts the interface, which adjusts its shape so as to meet the plate at a prescribed contact angle. If the plate angle is changed, the shape of the surface also changes. At a particular plate angle, called the contact angle, the interface should be horizontal. As light passes through the surface from above, it is refracted. Ray tracing indicates that parallel incident light produces distinctive final light distributions. Fig. 1 depicts three plate angles and three characteristic signatures that the surfaces produce, given that the lower liquid has a higher index of refraction than the upper liquid. If the upper liquid has a higher index, the right and left signatures are interchanged. The dark portion of the signatures lies between the dividing rays that pass on either side of the contact line.

The apparatus, which is described in Sections 2 and 3, employs a motor mounted prism and a lens to produce a uniform parallel scan of laser light. The scan is used to illuminate the interface from above and expose a 1024 element photodiode array below to record the light-intensity signature. The laser scan crosses the array in about 1.4 msec at a repetition rate of 15 Hz. In addition, the apparatus employs a double-acting piston to move the interface at a wide range of speeds, both advancing and receding. The combination of short exposure and reasonably fast repetition rate enables the apparatus to be used to measure dynamic contact angles. The choice of liquids for use in the apparatus is discussed in Section 4. The

experimental procedure is described in Section 5. The data processing, results, and discussion are given in Sections 6 through 8.

2 Experimental Apparatus

The Cell and Rotation Mechanism: The experiments were conducted inside a sealed stainless-steel cell shown in Fig. 2. The inside diameter is 3.000 inches and the inside surface is honed to a 6-8 micro-inch finish. Optical windows, 6 mm thick, on the top and bottom of the cell provide laser-scan passage through the cell. The windows are sealed against internal pressure by spring-loaded teflon face seals and against internal vacuum by back-up rubber O-rings. A glass plate, 50 mm square and 6 mm thick, clamped to a rotatable shaft, provides the solid surface for the study of contact-line and contact-angle phenomena. The shaft passes through the cell from one side to the other with spring-loaded teflon seals and back-up rubber O-rings for sealing. All wetted surfaces are either stainless steel, glass, or teflon.

The angular range of the glass plate is 90°, from perpendicular to parallel with the incoming laser scan. A commercially available 100:1 elliptical-bearing reducer (Harmonic Drive Model HDUS-18-100) provides the means for changing the angle of the glass plate. The output shaft of the reducer is coupled to one end of the shaft supporting the glass plate. A handwheel, a marked dial (100 divisions), and a rotation counter on the input shaft together provide an angular positioning accuracy better than 0.036° for the glass slide. The backlash of the reducer is quoted by the manufacturer to be less than 0.033°.

Double-acting Pistons: The double-acting stainless-steel piston assembly shown in Fig. 3 is employed to displace equal volumes of fluid in order to move the interface vertically inside the cell. The piston bore and the cell bore were honed as one solid tube prior to machining into individual pieces, to ensure that the inside diameters were identical. Once again seals for internal pressure are spring-loaded teflon, and seals for internal vacuum are rubber O-rings.

The piston rod, which is attached to a piston at each end, is itself attached to a precision linear traverse (Aerotech, Inc. Model ATS303M). One revolution of the input shaft to the traverse moves the piston 2 mm with an accuracy of 1 micron/cm, with a total range of 75 mm.

A microstepper motor (Compumotor Corporation Model LE57-83) is used to drive the input shaft. The stepper motor has 25000 steps/rev, with an accuracy of 0.08°. The stepper motor is controlled by a computer over an RS-232 interface to a Compumotor 2100-1 indexer. A check on the movement of the traverse is made by employing a long range (5 inch) Starret dial indicator. Fig. 3 shows its position along with the traverse and motor.

Optical Bench: An optical bench was designed specifically for these experiments. The design employs three shelves for the location of laser, optics, mechanical components, sensors and scanning motor (Fig. 4). The cell and double-acting pistons are located on the second shelf, to accommodate transmitting the laser scan vertically through the cell and sensing the light intensity distribution on the lower side. The laser scan is produced by a prism mounted on the shaft of a hysteresis synchronous motor (Hurst Model HB 900 RPM) located on the upper shelf. The polarized light (λ = 632.8 nm) from a He-Ne laser (Spectra-Physics Model 120) is focused and located on the reflecting surface of the prism using lens 1 and the periscope. A small portion of the total arc of laser light is intercepted by lens 2, which is adjusted to produce a parallel scan. The large prism directs the scan down through the cell to the photodiode array on the lower shelf.

A beam splitter, located just after lens 2, redirects half of the light toward lens 3, where it is focused onto the laser-power monitor. This arrangement enables synchronous measurement of the laser-light intensity that exposes the photodiode array. Adjustment of the intensity of the polarized laser light, to prevent saturation of the photodiode array, is achieved by adjusting the polarization angle of the single polarizer on the top shelf.

Liquid Reservoirs and Plumbing: The liquids are kept in commercially available 500ml HPLC reservoirs (Kontes Article 953980-0502) prior to being transferred into the piston/cell system. These reservoirs facilitate storage under nitrogen. The plumbing used to connect the reservoirs, pistons, and cell is constructed of precision 316 stainless-steel pipe fittings and teflon valves (Fig. 5). A flexible connection between the pistons and cell is provided by including some flexible teflon tubing in the plumbing. Connection to the reservoirs is also through flexible teflon tubing.

3 Instrumentation

Photodiode Array: A photodiode array (EG&G Reticon Model 1024G) is used to detect the light-intensity distribution of the laser scan after passing through the cell. The one-dimensional array has 1024 elements, each 25 micrometers wide. The sensitivity of the array, as rated by the manufacturer, is 2.5 picoamps/microwatt/cm^2. However, the uniformity of response is ±14 percent. The saturation exposure is 1.8 microjoules/cm^2. The array is accompanied by two circuit boards (RC-100B and RC-106) that produce a sample and hold boxcar output. Two inputs, +5 and -14 volts d.c., from a triple-output power supply (Hewlett Packard Model 6236A) were originally used to power the array boards. Noise reduction was achieved by substituting a 5-volt d.c. supply to the array board (RC-106) from three large dry cells in series. This 5-volt supply is used by the board to recharge the photodiode array during each read/recharge cycle. The array requires two signal inputs, a clocking signal and a start pulse. The outputs from the array that are used in this application are the sample-and-hold boxcar signal and the blankout signal. The boxcar signal records the intensity of light on each pixel of the array. The blankout signal is low during the output of the boxcar signal on the video line (Fig. 9). More information about the instrumentation is given in the section that addresses system integration on the next page.

Laser-Power Monitor: The laser-power monitor consists of a phototransistor (Siemens BPX-81) configured according to Fig. 6. For best stability and reduced noise, a 1.5-volt dry cell is used to provide power for the monitor. The signal produced by this monitor is a reference for the temporal variation of the laser power.

The Data-Acquisition System: Contact-line motion and data acquisition are controlled by a laboratory computer system (Data Translation Lab-Datax model DT4236). The system has a DEC LSI-11/23 CPU with 256 kilobytes of RAM and a Winchester hard/floppy disk storage system (Scientific Micro Systems model FWT01177) with 35.6 megabytes of storage available on the hard disk and 1 megabyte of storage available on the floppy. User interface is provided through a DEC VT240 graphics terminal and a Diablo 630/ECS printer. The computer also contains a fast floating point processor (DEC FPF11), a line time clock (DEC KPV11-A), four serial interface ports (DEC DLV11-J), and several data-acquisition boards;

1. 8-channel 12-bit A/D converter (DT3382)
2. 2-channel 12-bit D/A converter (DT3371)
3. Programmable real-time clock (DT2769)
4. 32-line parallel digital I/O (non-DMA) (DT2768)
5. 32-line parallel digital I/O (DMA) (DRV11-B)
6. IEEE-488 GPIB interface (DT2791)

System Integration: It is useful to refer to the block diagram of the system in Fig. 7 and the associated timing diagrams in Fig. 8 and Fig. 9 for the following discussion. The 200 kHz clock pulses, used for the entire experiment, are generated by the programmable real-time clock (DT2769). The start pulses are produced by two phototransistors, mounted inside the box that houses the rotating prism, on the top shelf of the optical bench (Fig. 10). As the laser beam passes across each phototransistor, a TTL pulse is generated.

The motor that creates the laser scan rotates at 900 rpm; therefore, one rotation is completed in approximately 66 msec. During this time, the laser power is measured synchronously with the exposure of the Reticon array, the Reticon array is read, and the data are sent to the disk. Due to slow disk access time, it is necessary to double buffer the output to disk; take one scan and send it to disk while taking the next one.

Two digital outputs, Cntrl 1 and Cntrl 2 from the D/A converter, are used to clear and load the digital long delay. As the beam passes phototransistor 1 (Figs. 7, 10) the computer and the long-delay box are notified by a negative going TTL pulse. Software is used to prepare the A/D converter for the laser-power monitor data on channel 1. Meanwhile, the pulse is synchronized with the clock and used to start the long-delay box, which counts clock pulses to create a delay long enough to allow the laser scan to reach the scan aperture. The laser-power-gate pulse is then switched low to allow the A/D trigger to pass long enough for the A/D converter to record the laser power synchronously with the exposure of the Reticon array. After recording the laser power, software is used to prepare the A/D converter for the Reticon array data on channel 0. The second start pulse, created by phototransistor 2, is synchronized with the clock and sent to the Reticon array. The Reticon simultaneously outputs a low blankout signal and the video data. The blankout signal is used to gate the A/D trigger pulses so that the A/D converter can

record the array output. The A/D converter, which samples once per trigger pulse, takes data at 200kHz only while the array board is sending its video box-car signal. The trigger signal to the A/D board is delayed by approximately one half of a clock period to avoid sampling the switching noise on the box-car signal (Fig. 9). This delay also causes the first pixel to be missed by the A/D converter, however, 1024 values are still recorded. The last recorded value, always near 0, is used as a sychronization indicator. The data acquired from the laser-power monitor and the Reticon array are written to the disk while the next scan is being recorded.

Synchronization of interface motion and data acquisition is achieved by software control. The piston motion is started using the RS-232 interface and data acquisition is initiated after a variable delay loop in the software is completed. This delay is determined by counting the ST2-trigger inputs from phototransistor 1. This delay allows the interface to accelerate to speed and to come into view before data are collected, thus minimizing the number of empty frames that are recorded. The software programmable delay is also useful for the careful timing of delays between recorded scans for generating longer time series.

4 Liquid Pair Decision

The immiscible liquid pair that was used in the apparatus was chosen from Smedley and Coles (1990). Finite time and money would not allow more than a one of the 121 pairs listed in the table to be tested.

To facilitate the study of the interface shape near a moving contact line, the scale of the region of interest should be maximized. The capillary length δ is a suitable choice of length scale;

$$\delta = \left[\frac{\sigma}{\Delta\rho\, g} \right]^{1/2} \tag{1}$$

Consider a contact line in steady-state unwetting motion (Fig. 11), where the length scale δ is a rough measure of the distance from the contact line to the horizontal liquid surface. An arc of radius δ is drawn that encompasses a volume/unit length $\delta^2\gamma$ of liquid. The shear force acting on this volume of liquid is

$$F_\tau = \delta\tau = \delta\mu\frac{U}{\Delta} \tag{2}$$

where Δ is the thickness of the contact region. Assume that the bulk liquid moves at a characteristic velocity U roughly parallel to the solid surface and that $\Delta \approx \delta \sin\gamma$. Therefore,

$$F_\tau \approx \frac{\mu U}{\sin\gamma} \tag{3}$$

The force that produces this motion is the surface-tension force per unit length,

$$F_\sigma = \sigma\cos\gamma \tag{4}$$

In steady-state motion the surface-tension force and the shear force should be balanced, the wetting force is neglected. Thus

$$\sin 2\gamma \approx \frac{\mu}{\sigma} U \quad \text{(the capillary number)} \tag{5}$$

This relationship suggests $\gamma = f\left[\frac{\mu}{\sigma} U\right]$ as measure of the velocity dependence of the contact angle near U = 0. A generic plot of this relationship might look like the one shown in Fig. 12. Provided this non-dimensionalization is the proper one for this problem, the above argument indicates that better resolution of the transition can be obtained by minimizing $\frac{\mu}{\sigma}$ through a careful choice of liquids. If results regarding the behavior at the higher values of $\frac{\mu}{\sigma} U$ are wanted, it may be best to choose a liquid pair with a large $\frac{\mu}{\sigma}$. To recapitulate, liquids that facilitate the study of interface shapes have large capillary length (δ) and small $\frac{\mu}{\sigma}$. To maximize δ, $\frac{\sigma}{\Delta\rho}$ must be maximized. The average viscosity ($\bar{\mu}$) of the liquid pair is used for μ. In addition, a reasonable difference in the index of refraction is required by the diagnostic technique.

Table 1 shows the 15 liquid pairs from Smedley and Coles (1990) having the smallest values of $\frac{\bar{\mu}}{\sigma}$. The pairs are listed in order of increasing $\frac{\bar{\mu}}{\sigma}$. Note that each of the 15 pairs includes formamide, which has the lowest viscosity of the eight hydrophilic liquids listed in Smedley and Coles (1990). Fortunately, formamide is available in very high purity (99$^+$%). The value of δ, the difference in index of refraction, and the available purity of the second liquid if obtained from Aldrich Chemical Company (1989) are also included as important elements of the selection procedure. The largest value of δ found for the liquid pairs listed in Smedley and Coles (1990) was 0.74 cm for 1-bromooctane over formamide, which is ranked twelfth in Table 1. The first two pairs on the list have sizable δ and very high purity. However, the second pair, nonane over formamide, was selected due to the larger difference in the index of refraction for this pair. Despite the fact that this liquid pair has the second lowest value of $\frac{\mu}{\sigma}$ in Table 1, it is still a factor of six larger than the value of $\frac{\mu}{\sigma}$ for water (0.14 x 10^{-3} sec/cm).

5 Experimental Procedure

Cleaning Procedure: Prior to filling the reservoirs or assembling any part of the apparatus, a careful cleaning procedure was followed. It is common experience that contact angles are strongly affected by contamination. For this reason, the following procedure was employed, which is a slight variation of Procedure 'C' as specified by Scientific Specialities Service (1989):

1. Rinse with Freon 113 (1,2,2-trifloro-1,1,2-trichloroethane)
2. Scrub and/or ultrasonic bath with a biodegradable phosphate- free detergent (Chemsolve laboratory glassware cleaner, Malinckrodt)
3. Rinse thoroughly with tap water
4. Rinse with 1:1 nitric acid

5. Rinse with double-distilled deionized water

6. Air dry in an organic-free environment

Prior to assembly, all components were also flushed with high purity nitrogen to eliminate dust particles.

Liquid Transfer to HPLC Reservoirs: Transfer of liquids was achieved as shown in Fig. 13 by inserting one end of flexible tube 2 (carrying nitrogen) and one end of flexible tube 3 into the original bottle of liquid. The other end of tube 3 was located in the HPLC reservoir that was previously flushed with nitrogen using tube 1. By pulling vacuum on tube 4, with tube 1 closed off, the liquid was transferred into the HPLC reservoir through tube 3. When the desired volume of liquid was transferred, vacuum was removed. Nitrogen flow was continued and the vacuum tube was used as a vent. This procedure was used for both liquids. In addition, a small amount ($\approx$ 5 percent) of each liquid was transferred into the reservoir containing the other liquid. The two HPLC reservoirs were then shaken vigorously several times, over several days, to emulsify the liquids and promote mutual saturation. The reservoirs were finally connected to the apparatus through tube 3.

Filling and Emptying Apparatus: Prior to filling, the apparatus was carefully cleaned, flushed with nitrogen, and evacuated through the vacuum connections shown in Fig. 5. The tubing connecting the reservoirs to the apparatus also contained nitrogen. It was therefore necessary to pull vacuum on the reservoirs long enough to eliminate the nitrogen from the tubes. The following procedure was employed:

1. Move piston to minimum B.

2. Evacuate system with 1, 4 closed; 2, 3, 5, 6 open.

3. Bleed nitrogen into system through valve 1 to flush.

4. Connect reservoir that was removed for step 3.

5. Continue evacuating, pull vacuum on reservoirs long enough to eliminate nitrogen from flexible tubes connecting the reservoirs to the apparatus.

6. Close 2, 5.

7. Slowly open 4 to fill lower part of cell, up to the shaft, and small space B with liquid B. If any of the liquid splashes onto the upper window it is removed by heating the window with a blow dryer.

8. Close 4, 6.

9. Slowly open 1 to fill the space A with liquid A.

10. Open 2, to fill the rest of the cell with liquid A.

11. Close 1.

12. Get rid of the air bubble in the cell by first moving the piston to the minimum A position. Tilt the cell to move the bubble near the inlet to the tube leading to piston A. Now, by moving the piston toward minimum B, the bubble is withdrawn from the cell and rises into the purge valve.

13. Open 1 and the purge valve; pressurize reservoir B to push air out of purge valve.

14. Close purge valve, close 1; the system is full.

The following emptying procedure was employed:

1. Move piston to minimum B.

2. Attach low pressure nitrogen to vacuum valves 5 and 6.

3. Close 2, open 1 and 5.

4. Open 2 slowly to allow liquid A to be pushed out of the cell into reservoir 1, then close it.

5. Move piston to minimum A, thus pushing liquid A into reservoir 1 and drawing nitrogen into the apparatus through 5.

6. Open 6 to push liquid A out of the tubes from reservoir 1.

7. Close 1.

8. Close 5, open 4.

9. Move piston to minimum B, thus drawing nitrogen into side A while pushing liquid B and nitrogen into reservoir 2.

10. Open 2, thus pushing liquid B from the cell into reservoir 2.

11. Close 3, open 5 to push liquid B out of the tubes from reservoir 2.

If experiments were to be conducted with one liquid rather than two, the same procedure could be used. However, the low pressure nitrogen would be left attached to valve 1 in step 4 of the filling procedure. In addition, purging of air bubbles from the system would not be necessary.

Cell and Plate Alignment: The cell is aligned with the incoming laser scan to ensure that the scan enters normal to the upper window. This alignment is achieved by stopping the scan motor and tracing the reflection of the beam from the window back to the phototransistor housing. By adjusting the height of the four legs supporting the cell, the reflected beam is made coincident with the incoming beam. This technique achieves normal incidence with an estimated accuracy of ±0.05°. A similar reflection from the liquid-liquid interface is aligned with the incoming beam by shimming the optical bench to tilt the liquid interface in the desired direction, this is the least accurate alignment.

The reflection-alignment procedure is also used to calibrate the angle of the plate inside the cell. In this case, alignment is achieved by changing the plate angle with the handwheel (Fig. 2). The aligned condition is noted on the counter and marked dial and used as the $\theta = 0°$ reference. The estimated accuracy of this alignment technique is very good for the upper window and the glass plate (±0.05°.), however, the alignment of the interface may be off by as much as ±0.2°.

Interface Reference Level: With the plate set at $\theta = 0°$, the interface is raised by manually rotating the compumotor shaft until the interface makes contact with the lower side of the plate. At this point, the compumotor power is turned on and the liquid interface is raised the thickness of the glass plate, taking its volume displacement into account. This final position is noted using the dial indicator pictured in Fig. 3, and defined to be the reference level of the interface.

Plate Measurement Region: A given glass plate may have regions on its surface where the contact angle is different from other portions of the plate surface. Due to the possibility of contact-angle variation over the surface of the plate, all measurements are centered on the same part of the plate. In addition, this position is chosen such that it is visible over a large range of plate angles (Fig. 14).

For a given plate angle, the interface is moved from its reference level (described in the last section) to the starting position on the glass plate. Measurements are made as the interface is moved from the start position to the end position and back at a given velocity. The definition of the reference level makes it possible to locate the starting point on the plate fairly accurately ($\leq$ 1 mm) for most plate angles. Larger errors were found for the smallest plate angles, since a small error in the position of the reference level translates to a large error in the contact-line position in these cases. A greater concern in accurate positioning of the interface is the volume displacement of the glass plate; failure to correct properly for this displacement easily results in positioning errors of the order of half the plate length at small angles.

Distance and Velocity Along Plate: Desired distances and velocities along the plate can only be achieved if the presence of the plate is considered when setting the motor speed and the number of steps. Velocity must be corrected for blockage area at the height of the interface. Distance must be corrected for the amount of liquid volume displaced by the glass plate for the distance of motion desired. These corrections are relatively straightforward, provided the interface makes contact with the front and back surfaces of the glass plate. After the interface passes the bottom corner of the plate, on the shaft end, the blockage area is no longer constant as the interface moves, therefore, for a fixed motor speed, the V_{cl} changes with interface height.

The stepper motor has 25,000 steps per revolution and one revolution moves the double-acting piston a distance of 2 mm. The motor has a restricted range of speeds from 0.001 revs/sec to some torque-limited speed (maximum speed tried was ≈ 0.8 revs/sec) in steps of 0.001 revs/sec. The maximum motor speed is also limited by the fact that the liquid being forced into the cell causes interface disturbances at higher speeds. The velocity of the interface inside the cell, taking into account the area blockage, is

$$V_{pist} = \left[\frac{A_{cell} - A_{glass}}{A_{pist}} \right] V_{int} \tag{6}$$

$$A_{cell} = A_{pist} = \pi r^2_{pist} \tag{7}$$

Where V_{pist} is the velocity of the piston, V_{int} is the vertical velocity of the interface inside the cell, A_{cell} is the cross sectional area of the cell, A_{pist} is the area of the piston, and A_{glass} is the blockage area of the glass at the current interface height. The blockage area is dependent upon a blockage length L_{block} that varies with the plate angle θ, and the width w of the glass plate. L_{block} is the horizontal length of the plate at a given plate angle θ for a given plate thickness T.

$$A_{glass} = L_{block} w = \left[\frac{T}{\sin\theta} \right] w \tag{8}$$

In addition, contact line velocity V_{cl} is related to the vertical velocity of the interface V_{int} by the sine of the plate angle θ.

$$V_{cl} = \frac{V_{int}}{\sin\theta} \tag{9}$$

Therefore, the piston velocity is related to the interface velocity by

$$V_{pist} = V_{cl} \left[\sin\theta - \frac{T w}{\pi r^2_{pist}} \right] \tag{10}$$

The distance that the interface moves inside the cell D_{int} relative to the distance the piston moves D_{pist}, is also dependent upon the presence of the glass plate. This relationship is easily found by multiplying the above expression for the velocity relationships by time.

$$D_{pist} = D_{cl}\left[\sin\theta - \frac{T w}{\pi r^2_{pist}}\right] \tag{11}$$

At small plate angles, the correction for velocity and distance changes when the contact line on the lower side of the plate reaches and passes the bottom corner of the plate on the end that attaches to the shaft. In this case, the correction is essentially the same; however, the blockage length L_{block} is different. As smaller angles are approached, the blockage length goes to infinity according to the given equation. However, the plate is of finite length L, and the maximum possible blockage is the diagonal length of the plate. As the interface approaches the shaft, the blockage length decreases and the speed of the contact line therefore decreases. In these cases, L_{block} was taken as the blockage length at the center of the desired travel. Under these circumstances, the contact-line velocity would be higher than desired when the interface was moving below the midpoint and lower than desired when the interface was moving above the midpoint.

$$L_{block} = \frac{L_{plate}}{\cos\theta} \tag{12}$$

Where L_{plate} is the distance along the plate from the top corner of the plate, near the shaft end, to the center of the desired travel.

Experimental Protocol: The interface was moved and data were collected under programmed control. Manual intervention was required only to adjust the plate angle and enter it into the computer (Fig. 15).

Prior to moving the interface from its reference position to the start position, a 3 second tare was recorded with the plate in the scan. After arriving at the start position, the interface was moved from the starting position to the end position and back at a contact-line velocity of 0.1 mm/sec. This motion was executed so as to define an initial condition on the plate. After this

conditioning stroke, the contact-line velocity was set at the desired value and the receding motion was started. Data were recorded while the interface was in motion. The speed was then changed and the procedure repeated until all the desired contact-line velocities had been recorded for a given plate angle. Upon completing the final velocity, the interface was returned to the reference position. The program then waited for the plate angle to be changed and entered and the procedure was repeated. The above regimen was followed until the desired portion of (plate-angle, velocity) space had been recorded.

The recording of data was performed in several different ways. In earlier experiments, 3 seconds of data, centered on the midpoint of the motion, were recorded at a rate of 15 scans/sec. In other experiments, 2 scans, 1/15 second apart, were recorded at 26 equally spaced intervals of the entire motion. In the latest experiments, single scans were recorded at 52 equally spaced intervals of the entire motion ($\approx$ 1 scan/0.5 mm) in order to generate an extended time history of the contact line motion. In all cases, required delays were implemented by counting motor rotations via the ST2 input to the programmable real-time clock (see *System Integration* in Section 3). Due to the extensive use of software control, these modifications were relatively easy to implement.

6 Processing the Data

Data Storage: The data were stored in binary form in directed-access files, i.e. data were stored and read in blocks of 512 bytes and each block of data has a number associated with it. The first block of each file contains run information for the file, such as date, time, plate angle, interface motion, etc. The remainder of each file contains several scans of data. Each scan consists of a 1 kilobyte record, from the laser-power monitor, of the laser-light intensity that exposed the array, followed by a 2 kilobyte record of the light intensity recorded by the 1024 pixels in the array. Each file is devoted to a single velocity and plate angle, and the files are numbered sequentially in the order that they were taken.

File Handling: All files were stored on the hard disk of the Lab Datax system and copied to 8 inch floppies when the disk became full. Single-sided 8 inch floppies were used to transfer the data files through HYDRA5 to the microVAX cluster (HYDRA0). All data processing was

performed in this environment due to the speed and power available in the cluster, despite the inconvenient data transfer procedure. All data were finally archived to tape storage.

Data Reduction: Fig. 16 shows the light-intensity signature produced by the presence of the optics and the windows of the cell. The array response is not uniform. However, it is within the uniformity specified by the manufacturer (see *Photodiode Array* in Section 3). The RMS deviation Fig 17 computed from an average of 50 scans shows that this response is constant for each pixel to within one percent of the intensity recorded; therefore, a single scan provides a reasonably good record of the light-intensity signature. Note that the light intensity is given in counts from the A/D converter (1 count = 4.8 mV). The dynamic range of the array output is approximately 530 counts. The light-intensity signatures shown have been inverted. The output from the array is actually negative for high light intensity and approximately zero or slightly positive for no light. The inverted view makes the light-intensity signatures easier to interpret, since large numbers represent high light intensity and low numbers represent low light intensity. The base-line intensity is set by adjusting the polarizer on the top shelf of the optical bench (Fig. 4).

A tare level was recorded with the interface at the reference level for each plate angle (Section 5). The tare is the initial picture. An example of tare data is shown in Fig. 18 for a plate angle of approximately 48° and should be compared to the data for the case without a plate in Fig. 16. Note that the plate introduces a few peaks and some optical noise. The deep valley on the right is caused by reflective loss of the light illuminating the end of the plate. Fig. 19 shows a raw light-intensity signature produced by a contact line that is receding at 0.05 mm/sec; note the continued presence of the valley on the right. The raw signature in Fig. 19 is corrected by subtracting the tare in Fig. 18 to produce the result pictured in Fig. 20. The operation of subtraction produces a signature that is corrected for non-uniformity of pixel response and for optical distortions caused by the plate and windows. Note that the valley at the interface has become more noisy in Fig. 20 than it was in the raw trace pictured in Fig. 19. This lack of correction is due to the fact that pixel nonuniformity is greatly reduced at zero light intensity, therefore, the tare (Fig. 18) reintroduces the noise when it is subtracted. It is also important to note that the corrected signature in Fig. 20 is more noisy to the left of the contact

line than to the right of the contact line. The tare was recorded with the interface at the reference position; i.e. formamide in contact with the plate. However, nonane is in contact with the plate to the left of the contact line. Therefore, the correction is not as good to the left of the contact line as it is to the right of the contact line. This fact is of no consequence, since only changes in the part of the signature to the right of the contact line are being considered here (Fig. 1). All signatures shown throughout the rest of this chapter have been subjected to the subtraction correction. In addition to this subtraction correction, many signatures from a given run were shifted and averaged to determine an average profile, on the right side of the contact line, for a particular velocity at a particular plate angle. This procedure of shift-averaging is discussed further in the section: *Try "Sticky" Plate Again* since this processing was only used on the "sticky"-plate data.

7 Discussion of Results

Introduction: During an earlier stage of the experiments, the liquid interface position, during the off state of the apparatus, was not carefully controlled. The signatures that were observed as the contact region traveled along the upper portion of the plate were very different from those that were seen as the contact region traveled along the lower portion of the plate. As the contact region advanced up the plate, initially no lack of light was seen in the signature, however, as the dividing line between the binary states of the surface was crossed, the signature developed first a distinct valley followed by a large peak as shown by the generic light intensity distribution pictured at the right in Fig. 1.

By looking into the cell through the upper window, the contact region on the plate could be observed. During the approach to the dividing line, the contact region was barely visible. However, as the dividing line was met and passed, the contact region became very well defined and thus easily visible. The contact line looked as though the contact angle changed drastically as the dividing line was met and crossed. Before and after crossing this line, the signature remained essentially unchanged as it traveled. Due to the fact that this binary behavior, at least visually, appeared to occur along the full width of the plate, it was assumed that there was some hysteresis effect, perhaps caused by leaving the glass plate partially immersed in the interface at

that level. In an attempt to rid the glass plate of this binary behavior, the interface was moved to the reference point and left for a period of one month. A quick test after this period of time revealed that the binary behavior was essentially unchanged. At this point, new optical quality windows and a thicker glass plate were obtained (the previous plate-glass windows introduced a lot of optical noise). The question before installation, of course, was how the glass plate should be treated prior to installation and during residency in the cell.

In an attempt to understand the effect of pretreatment of the glass plate, a short series of surface treatment tests were conducted.

One spare 2-mm thick glass plate was cleaned according to the procedure outlined at the beginning of Section 5. The plate was then suspended, partially immersed, in an interface between nonane and formamide. After 6 hours in the liquid, the plate was manually moved in and out of the interface while visually observing the behavior of the contact line. Indeed, it was seen to behave in the same binary fashion observed on the plate inside the cell of the apparatus.

Two spare 2-mm thick glass plates were cleaned according to the procedure outlined at the beginning of Section 5. One plate was soaked in nonane and the other was soaked in formamide for a period of 24 hours. When tried in the interface, the formamide-soaked plate was completely "slippery" (smooth contact-line motion) whereas the nonane-soaked plate was completely "sticky" (lack of smooth contact-line motion, a lot of interface deformation). Following this observation, both plates were then suspended, partially immersed, in the interface for 24 hours. A visual check the next day indicated that the binary behavior had set in for the formamide-soaked plate, whereas the nonane-soaked plate remained entirely "sticky".

The hypothesis was that perhaps a thin film of formamide made the plate "slippery". Suspending the plate in the interface caused the film to drain off the portion of the plate located above the interface. The conclusion was to soak the plate in formamide prior to installation into the apparatus and to ensure that the plate was always fully immersed in formamide during the off state of the apparatus. It was felt that this procedure would prevent the occurrence of the binary behavior. It was also expected that the plate could be changed from "slippery" to "sticky" by letting it drain while still inside the cell.

Three types of experiments were conducted with the "slippery" plate. One experiment tested the repeatability of the motion, the second experiment examined changes that occurred throughout (plate angle, velocity) space, and the third experiment examined the higher contact-line velocities. In addition to these experiments, some ray-tracing was done to develop an intuitive feeling for the light-intensity signatures. The results from this work are discussed in the section: *Ray Tracing*.

After completing the first two experiments with the "slippery" plate, an attempt was made to produce a sticky plate by moving the interface to the bottom edge of the plate. The results obtained from these trials are outlined in the section: *Try "Sticky" Plate*. However, the plate did not become "sticky", as expected, except in a very small region. In order to produce a "sticky" plate, the plate had to be removed, cleaned, and soaked in nonane. Results obtained from the "sticky"-plate experiments exhibited the types of light-intensity signatures shown in Fig. 1, and are presented in the section: *Try "Sticky" Plate Again*. Therefore, it was possible to determine the contact angle for various contact-line velocities only on the "sticky" plate.

Repeatability Experiment: The repeatability experiment was conducted after the apparatus was dormant for 12 hours with the liquid interface at the reference position (i.e. plate fully immersed in formamide). The protocol involved moving the interface from the reference position to the start position, then recording data as the interface was moved from the start position to the end position and back at a contact-line speed of 1.0 mm/sec. The interface was moved back to the reference position and the experiment repeated for a total of nine trials at a constant plate angle of 15°. For these experiments, no conditioning stroke was used.

The corrected light-intensity signatures for this experiment are given in Figs. 21-25. Each figure shows nine signatures, each from a different trial. The plots in each figure are read in order from top to bottom and then left to right. The successive figures represent later times in the procession of the advancing contact line across the illuminated portion of the glass plate. The results for the receding portion are not shown, since they are less distinctive and will be seen in the tour of (plate angle, velocity) space that follows. Fig. 21 depicts scan 9 from all nine trials, Fig. 22 depicts scan 19 from all nine trials, and so on to scan 49 in Fig. 25. For this experiment, 2 scans were recorded 1/15 second apart, with a delay of 13/15 seconds between

the pairs of scans. Therefore, a total of 5 seconds has elapsed between scan 9 and scan 19 and thus between each pair of figures.

A general observation is obvious. The nine trials produced light-intensity signatures that are nearly identical at equivalent times. The shape of the moving interface that produced these signatures is essentially repeatable. As the interface advances from right to left there are a few distinguishable features. An intensity maximum leads the intensity minimum. The light intensity changes more abruptly from the maximum to the minimum than from the minimum to the mean level established at the right of each plot. Note that the absence of light is represented by approximately -300 counts for this experiment.

A general consideration required for the understanding of these light-intensity signatures is as follows: if the interface is concave upwards, the light is spread out as it is for a negative lens and if the interface is concave downwards, the light is concentrated as it is for a positive lens. The light intensity signatures seen here indicate that there is a small portion of the interface that is concave downward followed by a larger portion of the interface that is concave upward.

As the interface moves, the signature to the right of the contact region appears to be less noisy than that to the left of the contact region. A tare has been subtracted from the original raw data. That tare was taken with the contact region off the left side of the plot; therefore, optical noise introduced by optical inhomogeneities is better corrected when formamide is in view, than when nonane is in view. In addition, optical noise is better corrected in the flat region of the signature to the right of the contact region, because the curved region introduces a shift in the optical noise that prevents its correction by the subtraction technique. Optical noise on the curved portion of the contact region is worse in Fig. 22 than in Fig. 23 or Fig. 24, since the optical noise on the tare signal is not uniform across the observed area. Fig. 25, which depicts scan 49 from each of the nine trials, does not demonstrate the same degree of repeatability seen in the previous figures. At this point in its travel, the interface interacts with the shaft holding the glass plate, this interaction produces a large dimple in the surface that is seen in six out of the nine trials at scan 49. However, this is an end effect that occurs at the end of the motion and is not the central issue here.

During the repeatability trials the contact line on the back side of the plate passed the lower corner of the plate at the end connected to the shaft. This event, which is not noticeable in the data presented thus far, was easily observed on an oscilloscope that displayed the light intensity signatures in real time. When the contact line passed the corner of the plate, a wave caused deformation of the intensity trace. Passing this point means that the velocity is no longer constant, since the blockage length decreases as the interface moves upwards (see *Distance and Velocity along Plate* in Section 5).

The change in contact-line velocity can be detected from the data by plotting the scan number against the location of the minimum of each corrected light-intensity scan. Fig. 26 depicts these minima for every second scan from the first trial pictured at the upper left of each of Fig. 21-25. Every second scan was used in the mode 1(2)51, since two scans were recorded at each of 26 equal time intervals. Fig. 26 shows that the velocity (pixels/scan), which is the local slope (dx/dy) of this set of points, changes at approximately pixel 350. Note that a steeper line on this plot represents a slower velocity. The dotted line in the figure is the expected slope of the contact-line motion based on the motor speed and the angle of the plate. Scatter in the points is due to optical noise that interferes with the determination of the actual minimum. Regardless of scatter, however, this type of plot offers a means for determining where to observe the interface as well as a means for determining the local velocity of the interface. Fig. 27 depicts sets of tracked minima for each of the nine trials, demonstrating once again the high degree of repeatability. Just as it is possible to track minima, it is also possible to track maxima, as shown in Fig. 28. However, noise interferes more in the case of maxima, since the difference between the maximum and the mean light intensity is smaller than the difference between the minimum and the mean. The change in velocity of the contact region is not as easily seen on the plots of the maxima as it is on the plots of the minima.

Tour of (Plate Angle, Velocity) Space: The experiment involving a tour of (plate angle, velocity) space was conducted to determine any variations in interface shape that might occur as the plate angle and contact-line velocity were changed. Previous test experiments, at larger plate angles, up to 40°, indicated that if a peaked profile were to be seen, such as the one depicted in the diagram on the right in Fig. 1, it should be in the part of parameter space

indicated in Fig. 29. The numbers of each of the following figures that correspond to particular regions in parameter space are inside the circles in Fig. 29. The protocol involved in this experiment is described in Section 5. The recording means used here was the same as for the repeatability experiments just described. Velocities of ± 0.1, 0.2, 0.5, 1.0, 2.0, 5.0 mm/sec were recorded for plate angles of 15°(2°)3°, a total of 84 data files, one for each velocity, and 7 tare data files, one for each plate angle.

Figs. 30-35 depict typical receding signatures, while Figs. 36-41 depict typical advancing signatures. Each plot in each of these figures represents the corrected signature from scan 25 for the receding cases and from scan 41 for the advancing cases. Immediately noticeable is the fact that the receding profiles seen in Figs. 30-35 are very distinct from the advancing profiles seen in Figs. 36-41. Note that absence of light is represented by approximately -225 counts for this experiment.

The advancing profiles are qualitatively similar to those seen in the repeatability experiments with a leading maximum and trailing minimum. Some aspects of these features change with plate angle and advancing speed. As the interface is moved at higher speeds, the maximum is seen to increase in magnitude, and the recovery from the minimum occurs over a smaller spatial scale. This change indicates that the distance along the interface that is affected by the moving contact line decreases with increasing speed. In addition, whatever is causing the maximum, perhaps a leading bump or wave, must be increasing in curvature to focus more light at the maximum intensity point on the array. Another noticeable feature of these profiles is that the minimum is deeper for higher speeds at a given plate angle. The minimum is also deeper for a given speed at larger plate angles.

Note that the signature shown for a plate angle of 7° and velocity of 0.1 mm/sec in Fig. 37 is shifted from the others due to a roundoff error involved in the calculation of the delay between pairs of recorded scans because the motor speed was so low. This error also occurs for all scans taken at a plate angle of 3° in Figs. 38 and 41. Otherwise, despite their recorded position, these signatures are essentially unchanged as they cross the illuminated region, as seen earlier with the repeatability data in Figs. 21-25. This same error made itself apparent in the -0.1 mm/sec signature for 7° in Fig. 34 and at 3° in Figs. 32 and 35.

The receding profiles seen in Figs. 30-35, although less distinctive than the advancing ones in Figs. 36-41, still have characteristics that change with speed and plate angle in a manner very similar to the advancing ones. The minima are larger at lower speeds, opposite to the advancing case, and at larger angles, just as in the advancing case. In fact, at smaller angles and higher speeds, the signatures seem independent of speed (Fig. 34 for 7° and 5°). In all receding cases, the fall from average light intensity to the minimum appears to occur over the same spatial scale as the rise from the minimum back up to the average. This fall and rise were different in the advancing cases. In addition, there are no detectable maxima in the receding cases.

Plots of tracked minima for various plate angles and advancing speeds are shown in Figs 42-45. Note that all of the plots tend to have similar slope, despite widely varying speeds. This similarity in slope is testimony to the accuracy of delay between pairs of scans, such that a complete record of the moving interface is obtained. To determine the time between plotted points, add 2 to the value of DELTA (given below each plot) to get the number of scans between recorded ones and divide by 15 scans/sec to get the time. Note, that calculated delays yield even samples across the array at larger angles in Figs. 42 and 44. Fig. 43 depicts plots that demonstrate absence of minima for early times. This anomaly is due to a offset in space caused by an error in the known position of the interface at the start reference level. Despite this positioning error, a sizable number of the scans recorded the interface. Similar positioning error is seen for all speeds at a given angle. However, the middle figure in the left column of Fig. 43 is distinctly different from the others in the same row, due to the error in the calculation of the delay between scans discussed above for 7° at 0.1 mm/sec.

The plots of minima yield information regarding the passage of the interface beyond the lower corner at the end of the plate attached to the shaft. In the repeatability experiments, which were conducted at a plate angle of 15°, the velocity change was seen to occur somewhere near pixel 350. As the angle is decreased, it is expected that this break point should move to the right. Indeed, at 13° this point appears to be near pixel 500, at 9° it is near pixel 750, and at 5° it is probably off the right side of the array.

Try "Sticky" Plate: After obtaining the previous data and not finding the expected light intensity profiles (Fig. 1), the plate was left hanging for 24 hours with the interface at the bottom edge of the plate. The hope was to produce a "sticky" plate that would then yield different light-intensity signatures from those seen with the "slippery" plate.

The only evidence of "sticky"-plate behavior was found at the left-most extent of the illuminated region of the plate. A time series of the results for a plate angle of 5° and a speed of 0.1 mm/sec is shown in Figs. 46-47. Once again, plots are read from top to bottom, left to right in order of increasing time. Approximately 11 seconds elapsed between the plots shown. Notice that the contact region advances in the expected way in the plots shown in Fig. 46. However, the behavior changes dramatically in the plots shown in Fig. 47. A distinct valley forms, indicating a distinct lack of light, then in a short moment between scans 43 and 45, the contact region pops back into a near normal shape. As this was observed on the oscilloscope, the return to a near-normal state occurred on a time scale on the order of 1/15 second. This behavior was seen to occur in this region for all speeds and angles tested that day, except however, at larger angles where it moved out of the field of view. The example shown for 5° was chosen since it presents the best view of this region of the plate. A slow speed was chosen so that the transition could be more carefully observed. Aside from this anomaly, no other effect was seen as a result of the overnight drainage.

Higher Speeds: No other part of the plate appeared to be affected by the hanging of the plate, therefore, some runs were made at high speeds on the "slippery" part to see if any further change in signature occurred. This set of experiments was conducted at 5° because slower motor speeds are required for a given contact-line speed if the angle is smaller and the amount of liquid that needs to be moved to produce the 25-mm motion of the contact line is also smaller at small angles. A summary of the results is shown in Fig. 48. Note that the scans have been chosen such that the contact region is in nearly the same place for all speeds. Plots of increasing speed are presented from top to bottom and then left to right. Plots of signatures obtained from speeds of 0.1, 0.2, 0.5, 1.0, 2.0, 5.0, 10.0, 20.0, and 25.0 mm/sec are presented. Note, once again, that as the speed is increased, the valley gets deeper, but fails to reach the no-light level of plots seen in Fig. 47. In addition, the leading maximum, seen before, increases

in size up to 5.0 mm/sec but seems to remain relatively unchanged at the three highest speeds. A very well defined broad maximum is seen on the trailing portion of the valley. This trailing maximum was not as visible at the highest speeds shown in Figs. 39-41, but a second look now makes it more evident. This is evidence that the curvature of the surface has changed sign in this region, as is discussed further in *Ray Tracing* below.

The plate was left hanging vertical with the interface at the bottom edge of the plate for a period of 5 days. Perhaps more time was required for the formamide to drain off the plate. A set of runs was done at a plate angle of 15° and revealed that the contact-line behavior was essentially the same as it had been for the 24 hour case discussed earlier. Apparently the reversible nature of the plate surface, discussed in the introduction to section 7, would not occur for the plate inside the cell.

Ray Tracing: In order to develop a better understanding of the light intensity signatures that were observed experimentally, a ray tracing program was written to compute trajectories of light rays passing through the cell. For the calculations, handbook values were used for the indices of refraction of nonane, formamide, and optical glass. The interface on the lower side of the plate was assumed to be out of the light path (a very good assumption for small plate angles). The glass window at the bottom of the cell was included, since a large amount of refraction occurs at the glass-air interface where the largest change in the index of refraction is found. The program was designed to compute refraction for arbitrary interface shapes provided they are defined by an equation that is single valued. Distances from the plate to the window and from the window to the sensing element were not scaled, but chosen to be reasonable.

Fig. 49 depicts a light-ray pattern produced by a logarithmic interface. The interface is concave downward and produces a concentration of light at the bottom edge of the plot. A discontinuity in the slope at the contact line produces a diverging set of rays and an unlighted region. The light intensity in these ray-tracing diagrams is roughly proportional to the inverse of the spacing of adjacent rays. If this inverse were plotted, the light intensity distribution for this case would look much like that seen in the right diagram of Fig. 1.

A flat interface is shown in Fig. 50 and demonstrates a diverging set of rays at the contact line. Elsewhere, the intensity of light is uniform, just as depicted in the center diagram of Fig. 1. Fig. 51 shows the light intensity pattern produced by an interface that is concave upwards, in this case a decaying exponential with the slope at the glass surface chosen to represent an angle of 10°. Once again, the discontinuity in the slope produces a valley. Less noticeable is the fact that the rays to the right of the valley actually diverge slightly and become uniformly spaced near the right extent of the light scan. This behavior represents a long climb out of the minimum intensity at the valley before uniform intensity is reached. This result is similar to that seen in the left diagram of Fig. 1.

Note that in the three cases outlined above and depicted in Figs. 49-51, a discontinuity of slope exists where the interface meets the surface of the glass plate. In each case, this discontinuity produced a diverging set of rays and an unlighted region. If no discontinuity in slope occurs, i.e. the interface is tangent with the glass plate, the void no longer occurs. Fig. 52 shows an interface that generates a light distribution with a slight valley that has a slow recovery back to uniform light intensity. In all the observations of moving contact regions on the "slippery" plate, no lack of light was found. This lack of a distinct valley indicates that no discontinuity of slope was produced at the contact region, or that a very small and therefore undetectable discontinuity was produced. If no discontinuity exists, the contact angle must be 0° or very close to 0°.

Observed signatures for larger advancing velocities on the "slippery" plate have a trailing maximum that suggests the presence of negative curvature in the corresponding region of the interface. A possible shape consisting of a parabola that meets the glass plate at 0° and a smoothly connected logarithm produces the light intensity profile pictured in Fig. 53 that resembles slightly that seen in the experiments.

As yet unresolved is the meaning of the leading maximum for advancing cases. For the presence of this maximum, an area of negative curvature must exist that precedes the contact region. Perhaps a thin film of formamide is resident on the plate. This film would remain undetected as long as the surface of the film remained parallel to the glass plate. However, if the film were to bulge upward, forming a surface that is concave downward, a concentration of

light would be found on the detector. Perhaps a small wave is being pushed out ahead of the contact region as it moves, and it becomes larger as the interface moves at higher speeds. Similarly, the slow decrease in light intensity on the trailing side of the intensity minimum in the receding signatures is also not explained by the ray tracing.

Try "Sticky" Plate Again: The plate was removed, cleaned according to the cleaning procedure and soaked in nonane for a period of 12 hours. The plate was then installed in the apparatus and the interface was always left below the plate. After about 20 hours of soaking in nonane, a set of runs was made at 1.0 mm/sec for plate angles of 40°(5°)15°; 45°(5°)60°; 40° to see if "sticky"-plate behavior would be seen. Indeed, the plate was found to be sticky, and profiles like the ones shown in Fig. 1 were seen. The flattest intensity signature appeared to be at a plate angle of about 18° for this contact-line velocity. Two days later a more refined set of experiments was conducted that included plate angles of 25°(2°)11° and speeds of ±0.05, 0.1, 0.2, 0.5, and 1.0 mm/sec. However, the intensity signatures seen during this experiment were not the same as they had been 2 days earlier. The signatures suggested that the receding contact angle was much larger. The experiment was continued from 27°(2°)35°, 40°(5°)50°, for the same speeds. These signatures suggested that the receding angle was larger than 40°. The next day, another set of experiments for angles of 38°(2°)56° confirmed the results of the previous day. Apparently the condition of the plate surface had stabilized. Six days later, after adjusting the apparatus for larger angles, a set of experiments was conducted for plate angles of 66°(2°)38° and the same 5 speeds. These data demonstrated qualitatively similar behavior to those obtained 6 days earlier; therefore, these data are described below.

Light-intensity signatures for these cases are shown in the standard form in Figs. 54-74. Fig. 54 indicates the samples recorded in (velocity, plate angle) space; the numbers inside the circles are the numbers of the corresponding figures that follow. Therefore, each figure of Fig. 55-74 depicts a block out of the parameter space. For this presentation, scan 34 was selected, since it was the first scan within which the receding interface becomes visible at the left edge of the signature for the largest plate angle, see top signatures Fig. 55 and Fig. 60. Note, that a very distinct valley is present in the signature, indication of a discontinuity at the contact line that produces a pair of diverging rays. Advancing signatures have a very strong peak seen in

Figs. 65-74; whereas receding signatures seen in Figs. 55-64 do not. Note that absence of light is represented by approximately -125 counts for this experiment.

There are some notable features of the light-intensity signatures pictured in Figs. 55-74. At large plate angles, the end of the glass plate is very close to the left extent of the light-intensity signature. This presence is easily seen in Fig. 55 and Fig. 60 as a flat region approximately 200 pixels long, bordered on each side by upward and downward pointing spikes. The spikes are indicators of poorly corrected window presence due to curvature of the interface in that region. This is especially notable for the advancing cases in Fig. 65 and Fig. 70. As the plate is moved to smaller angles, follow through Figs. 55-59 or Figs. 60-64, its presence becomes less notable. Another effect that causes distortion of the corrected light-intensity signature is waves on the liquid interface. These waves are caused by interference from the jet of liquid entering the cell as the liquid interface is moved at high speeds at large angles (see Fig. 55 for V_{cl} = -1.0 mm/sec at a plate angle of 64°). Despite the problems inherent with distorted interfaces caused by these effects, they are easily recognizable and therefore easily avoided or noted.

Note that the width of the no-light region is smaller in the receding cases seen in Figs. 57-59 and Figs. 61-64 than in the advancing cases seen in Figs. 67-69 and Figs. 72-74. The no-light region for the receding cases is approximately 200 pixels wide whereas it is approximately 300 pixels wide for the advancing cases. This difference in width indicates that there is a greater discontinuity in slope at the contact line for the advancing cases.

A closer look at the receding signatures in a given column of parameter space indicates how the signature changes as the plate angle is varied. A sample of receding signatures for a contact-line velocity of -0.05 mm/sec and plate angles from 54° to 38° is shown in Fig 75. The vertical scale of these signatures has been magnified from 600 counts to 300 counts to better illustrate the change in shape of the signature. The upper left plot in Fig. 75 is for a plate angle of 54°. Note that the part of the signature to the right of the valley is concave downward, indicating that it is produced from an interface that is concave upward in this region (see Fig 1). The lower right plot is for a plate angle of 38°. Note that part of the signature to the right of the valley is concave upward, indicating that the interface is concave downward in this region, see Fig. 1.

The range of angles shown in Fig. 75 demonstrates the change in concavity of the interface as the plate angle is changed for a given speed. Judging from the signatures shown, one might guess that the contact angle for this speed is about 45° based on the fact that the signatures indicate that a flat signature should be found for this angle. However, there is some change in the signature as the interface moves across the plate that is not evident in a single scan. In some areas of the plate, the interface was seen to stick momentarily, thus changing the signature, while in other areas the interface moves very smoothly, with little change in the signature. Sticky regions of the plate were avoided by locating the right edge of the no-light region of the signature and tracking its progress. In order to locate the right edge, each signature was searched until a threshold of -20 was crossed. The pixel locations were plotted against the scan number as shown in Fig. 76. The upper plot is representative of the receding cases, and the lower plot is representative of the advancing cases. The dotted line in each plot is the expected slope computed using the motor speed and plate angle for each case. The slope of the dotted line agrees quite well for the later scans in the advancing case, whereas the receding interface is moving slower than expected. This discrepancy in slope is relatively small, but unresolved, it may be an optical effect. A line drawn through the points was used to indicated regions of constant velocity. Points that were not on the line indicated regions of non-constant velocity. For each velocity, at each plate angle, up to three sets of scans were chosen that lay on a line. The upper plot in Fig. 77 shows all the suitable scans from a plate angle of 48° and velocity of -0.05 mm/sec that were shifted and averaged. The lower plot shows the same for an advancing velocity of +0.05 mm/sec. In addition, each plot in Fig. 77 also shows an envelope of the minimum value and the maximum value at a given pixel to give some idea of the variation in the shape of the signature as the contact line moves across the plate. In some cases, a few scans were thrown out if they were located at the beginning or end of a set of scans and were significantly different from the average scan. In other cases, at the larger plate angles, many of the later receding scans and earlier advancing scans were thrown out due to interference caused by the presence of the shadow from the end of the glass plate. This culling procedure was performed by plotting the average, the minimum, and the maximum values at a given pixel on a single plot as shown in Fig. 77, and by plotting the individual scans that were at the beginning or end of a set of scans selected from Fig. 76. The remaining sets of

scans were shifted and averaged. Each of the shifted and averaged scans was visually checked on the terminal and was manually cut using cross hairs to remove the tail end of the averaged record. The trace in the upper plot of Fig. 77 was cut at pixel 351 and the trace in the lower plot was cut at pixel 553. The cutting of the record further removed interference from the shadow of the end of the plate. The remaining data were fitted by a decaying exponential using a nonlinear-least-squares subroutine from Numerical Recipes (1986) that was modified, to be more robust, by Phillip Tokumaru. The first 9 points of each averaged signature were ignored to eliminate interference from a small peak on the profile on the right side of the valley that is visible in Fig. 75. In addition, the origin of the exponential was shifted to x=10, the location of the first point. The multiplier of the exponential was plotted against plate angle for each receding velocity in Figs 78 to 82, to determine the zero crossing that indicates a flat signature. The equation of the least-squares fit to the data is given in the legend of each figure. The zero crossing for each velocity represents the contact angle for that velocity. It is interesting to note that the slope of the fitted line is apparently independent of the velocity, since the data overlap when plotted together in Fig. 83.

The above procedure was also employed to determine the contact angles for the advancing cases. The motion in these cases was much more stable, therefore, not as much culling of the signatures had to be done, aside from omitting scans at the larger angles that suffered from glass-plate interference. However, in the advancing cases, the light-intensity signature contained a peak at all angles and velocities measured since the maximum angle attainable by the apparatus was 66°. Therefore, it was necessary to extrapolate to find a zero crossing for the multiplier of the exponential fit to the advancing light-intensity signatures. Plots of the multipliers are given in Figs. 84 to 88. A quadratic fit was found to be appropriate for these data. The quadratic coefficients are given in the legend for x^0, x^1, and x^2. Once again, when all the velocities are plotted together, in Fig. 89, they overlap just as they did in the receding case. The extrapolated zero crossings were determined by solving for the largest root of the quadratic fit for each velocity. It is important to note that this is a distant extrapolation and is therefore not claimed to be very accurate, however, the result is a consistent one and therefore worth mentioning.

The end result of the data processing is the plot of contact angle vs. velocity given in Fig. 90. It is found that the contact angle depends only on the sign of the velocity and not on its magnitude for the range of velocities studied. The dashed line in the figure represents the maximum limit of the plate angle. The receding contact angle is approximately 50° whereas the advancing angle is approximately 78°. The capillary numbers varied from: $\frac{\mu}{\sigma}V = 4.2 \times 10^{-4}$ to 8.4×10^{-3}.

8 Conclusions and Recommendations

The results obtained for the "slippery" plate indicate a difference in the interface shape depending upon whether the interface is advancing or receding. Intuition and ray tracing indicate that the contact region must be concave upward in both cases. In addition, the radius of curvature of the interface in the advancing case must be smaller than it is for the receding case, since the advancing signature recovers from the minimum more quickly than the receding one. The minimum is deeper in the advancing case, indicating a faster change of slope near the glass plate than for the receding case. Results for the "sticky" plate indicate a behavior that is very different from that seen on the "slippery" one. There is a great difference between the advancing and receding velocities. Experiments conducted with the "sticky" plate yielded the change in light-intensity signatures that was expected from Fig. 1. Decaying-exponential curve fits to shift-averaged signatures yielded the dependence of the contact angle on the velocity. For receding velocities ranging from 0.05 mm/sec to 1.00 mm/sec, the contact angle was found to be independent of the speed with a value of 50°. For the advancing velocities, the contact angle was also independent of the speed with an extrapolated value of 78°. The contact angle depends only on the sign of the velocity for the velocities studied.

Recommendations: It would be useful to try different liquid pairs to check for a dependence of the contact-angle behavior on $\frac{\mu}{\sigma}$, and to find out whether the binary surface behavior that was observed with nonane/formamide is a general result or not. A thin plate is better used for work at small angles, since the interface on the lower surface goes beyond the bottom corner at the shaft-end of the plate at a later time. The thick plate, which yields a greater physical

separation between the contact line on the front and the back of the plate, is better suited for larger angles because it eliminates the problem of light interference from the contact line on the lower side of the plate.

A longer plate would facilitate experiments at smaller plate angles. In the current arrangement, at the smaller plate angles ($\theta < 10°$), the velocity of the interface decreased as the interface advanced up the plate. This change in velocity was caused by the fact that the interface was unable to make contact with both the front side and the back side of the plate at any interface height. Therefore, when the interface was on the front side of the plate, it was also above the lower corner of the plate at the shaft-end. As a result, as the interface moved, the blockage area changed and therefore the velocity of the interface changed. A longer plate would enable the experimenter to move the interface at a constant velocity near the end of the plate opposite the shaft. A longer plate would also enable the end of the plate to remain in the field of view at larger angles. In addition to the longer plate, a longer scan would also help to enlarge the usable angle range of the apparatus. It is important to note that the portion of the laser scan that extends beyond the ends of the Reticon array should be masked at the scan aperture. There is also a large reflection from one corner of the end of the plate opposite the shaft that can be removed by masking that portion of the scan at the large prism with a thin strip of tape.

Changing of test plates located inside the cell is a difficult task that could be simplified slightly if the cell were designed such that each lid is secured to the cell separately. In the current design, the two lids are held in place by four long pieces of rod, threaded on the ends, that pass from top to bottom through both lids. Removal of one lid requires the other lid to be removed also.

Another observation amounting to hindsight is that it is not necessary to have the inside diameter of the piston equal to the inside diameter of the cell when trying to determine the velocity of the contact line. The important aspect of these dimensions is that they be accurately known. The current setup has a minimum contact-line speed of about 0.002 mm/sec if the glass plate is vertical. This minimum speed increases with decreasing plate angles. However, the apparatus would yield lower speeds if a second double-acting piston, smaller in diameter, were

added in parallel with the large one. The large piston would be used for rough positioning of the interface and the small piston would be used to pump smaller amounts of liquid enabling slower speeds to be achieved.

References

"Aldrich Catalog Handbook of Fine Chemicals (1989-90)", Aldrich Chemical Co., Milwaukee, Wisconsin, 1989.

Bikerman, J. J. (1970) *Physical Surfaces*, Academic Press, New York.

Dussan, E. B. (1979) On the spreading of liquids on solid surfaces: Static and dynamic contact lines. In: *Annual Reviews of Fluid Mechanics* **11**, 371-400.

"Numerical Recipes The Art of Scientific Computing", Cambridge University Press, New York, NY, 1986.

Smedley, G. and Coles, D. Some transparent immiscible liquid pairs. J. of Colloid and Interface Science (To appear 1990).

Scientific Specialties Service Inc. Randallstown, MD 21133. Pre-Cleaned Bottle Book, 1988, p.16.

Table 1. Liquid pairs with small $\frac{\bar{\mu}}{\sigma}$

Liquid pair $\left[\frac{\text{liquid 1}}{\text{liquid 2}}\right]$	$\frac{\bar{\mu}}{\sigma} \times 10^3$ $\left[\frac{\text{sec}}{\text{cm}}\right]$	δ (cm)	Δ i.r. (i.r.$_2$ – i.r.$_1$)	Purity (Aldrich)
formamide / 1–bromobutane	0.54	0.55	-0.007	99$^+$%
nonane / formamide	0.84	0.26	+0.042	99$^+$%
1–chlorohexane / formamide	1.09	0.29	+0.027	99%
isopropyl benzene / formamide	1.20	0.27	-0.045	99%
dihexyl ether / formamide	1.32	0.24	+0.027	---
formamide / bromocyclohexane	1.42	0.33	+0.049	95%
ethyl caprylate / formamide	2.11	0.22	+0.029	99$^+$%
butyl benzoate / formamide	2.16	0.32	-0.049	99%
2,6–dimethyl – 4 –heptanone / formamide	2.22	0.18	+0.034	90%
butyl butyrate / formamide	2.27	0.20	+0.039	98%
butyl acrylate / formamide	2.40	0.20	+0.028	99$^+$%
1–bromooctane / formamide	2.44	0.74	-0.005	99%
1–decene / formamide	2.80	0.15	+0.025	94%
methyl caprylate / formamide	2.92	0.20	+0.030	99%
methyl benzoate / formamide	3.11	0.47	-0.069	99%

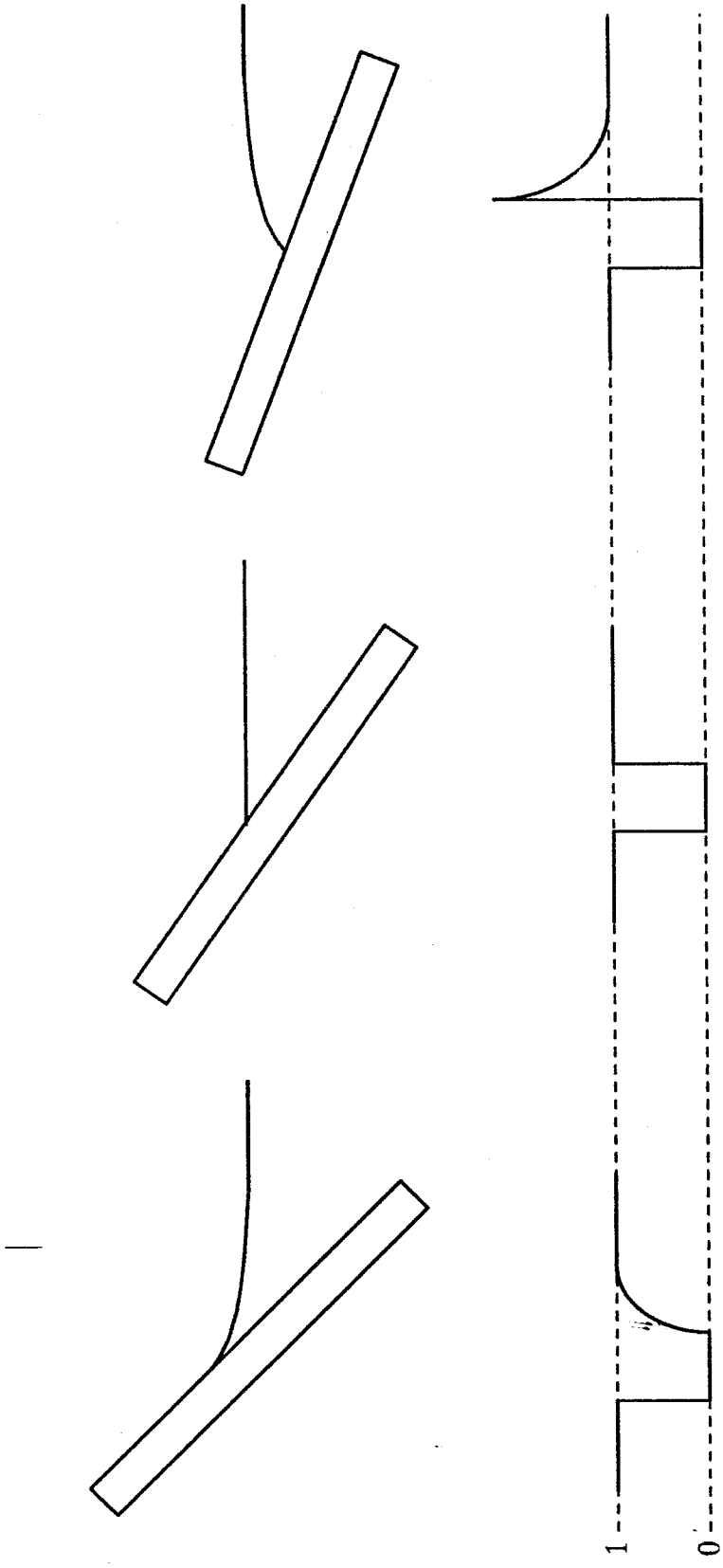

Fig. 1 Generic light intensity distributions

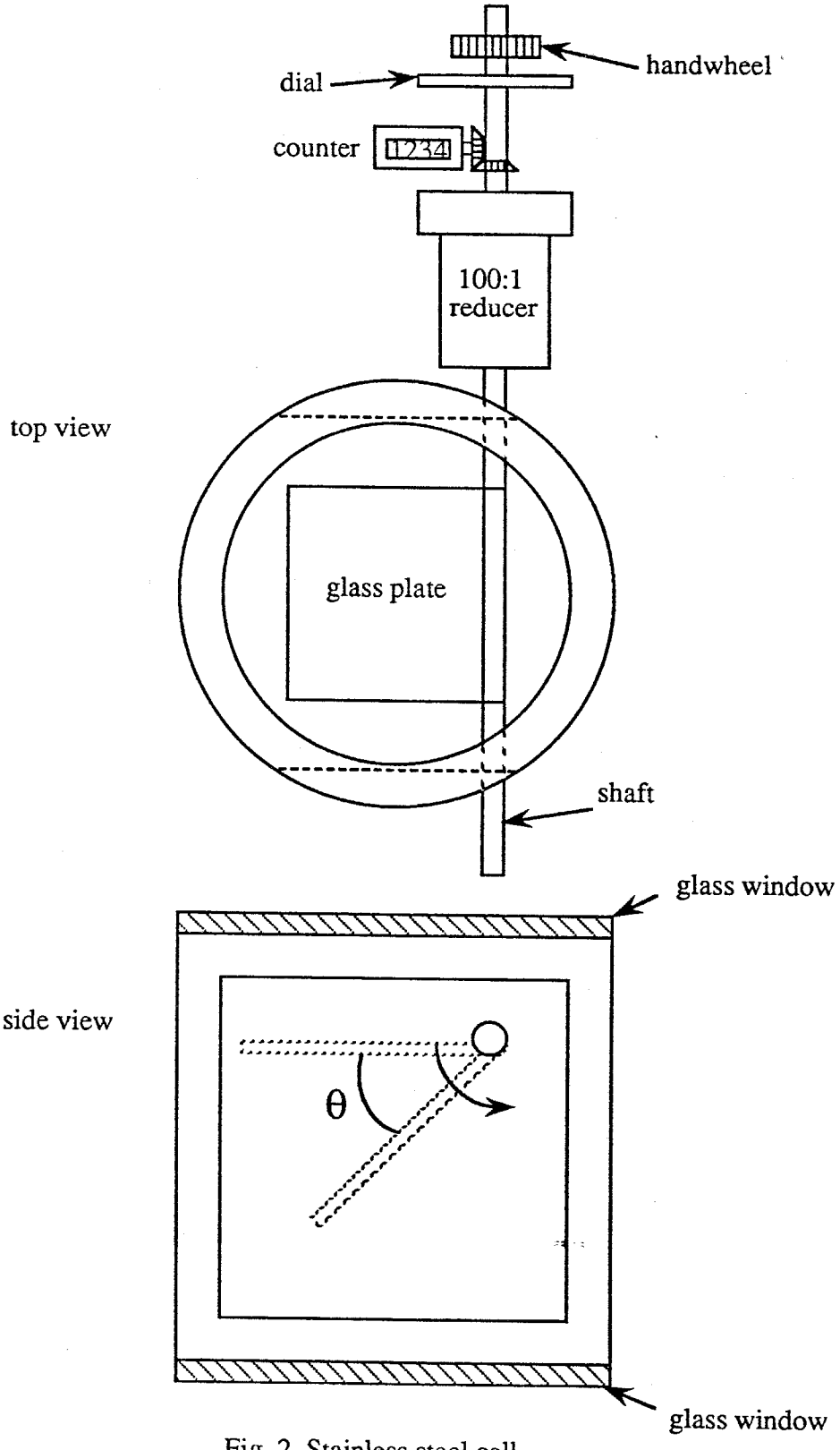

Fig. 2 Stainless steel cell

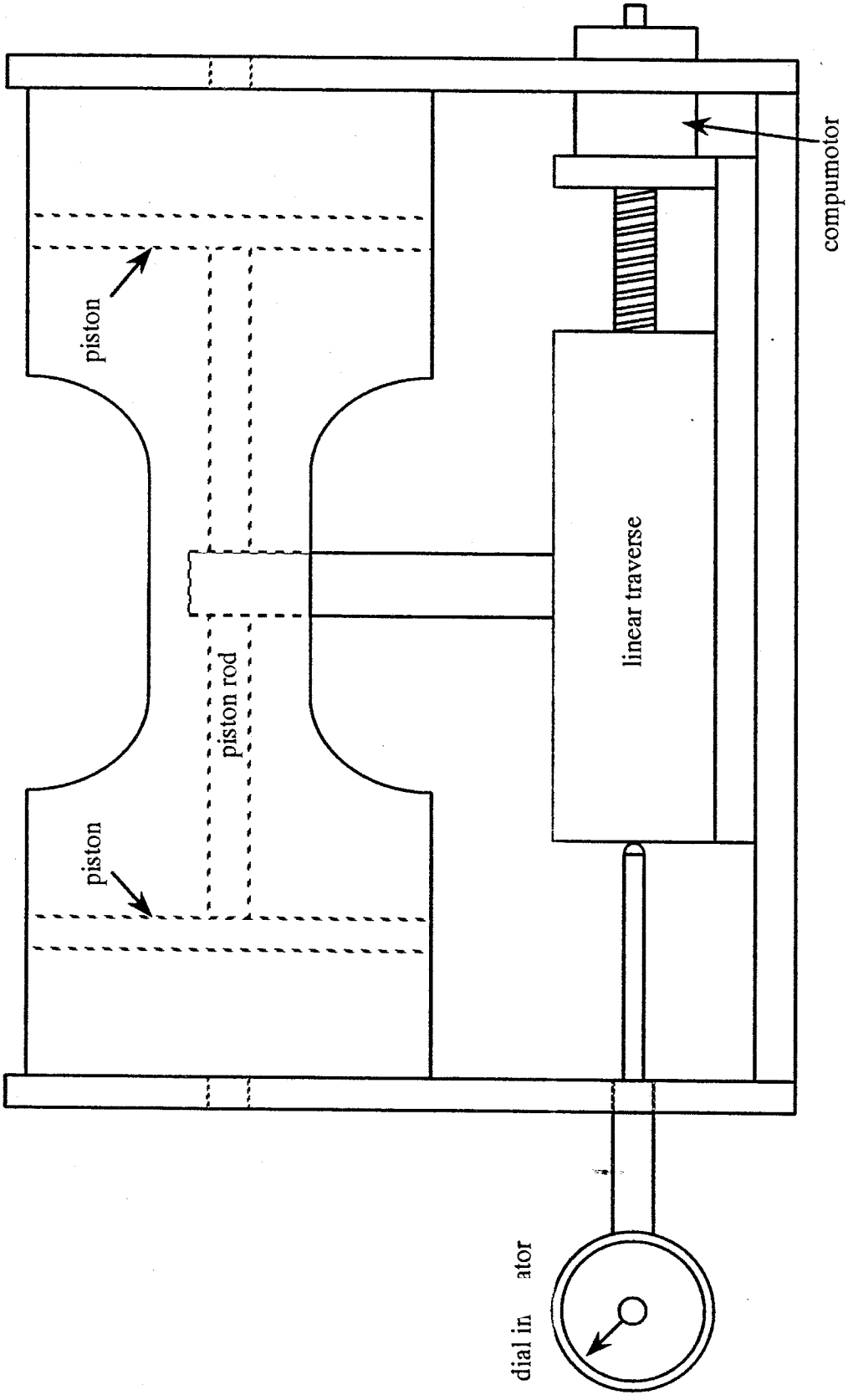

Fig. 3 Piston assembly

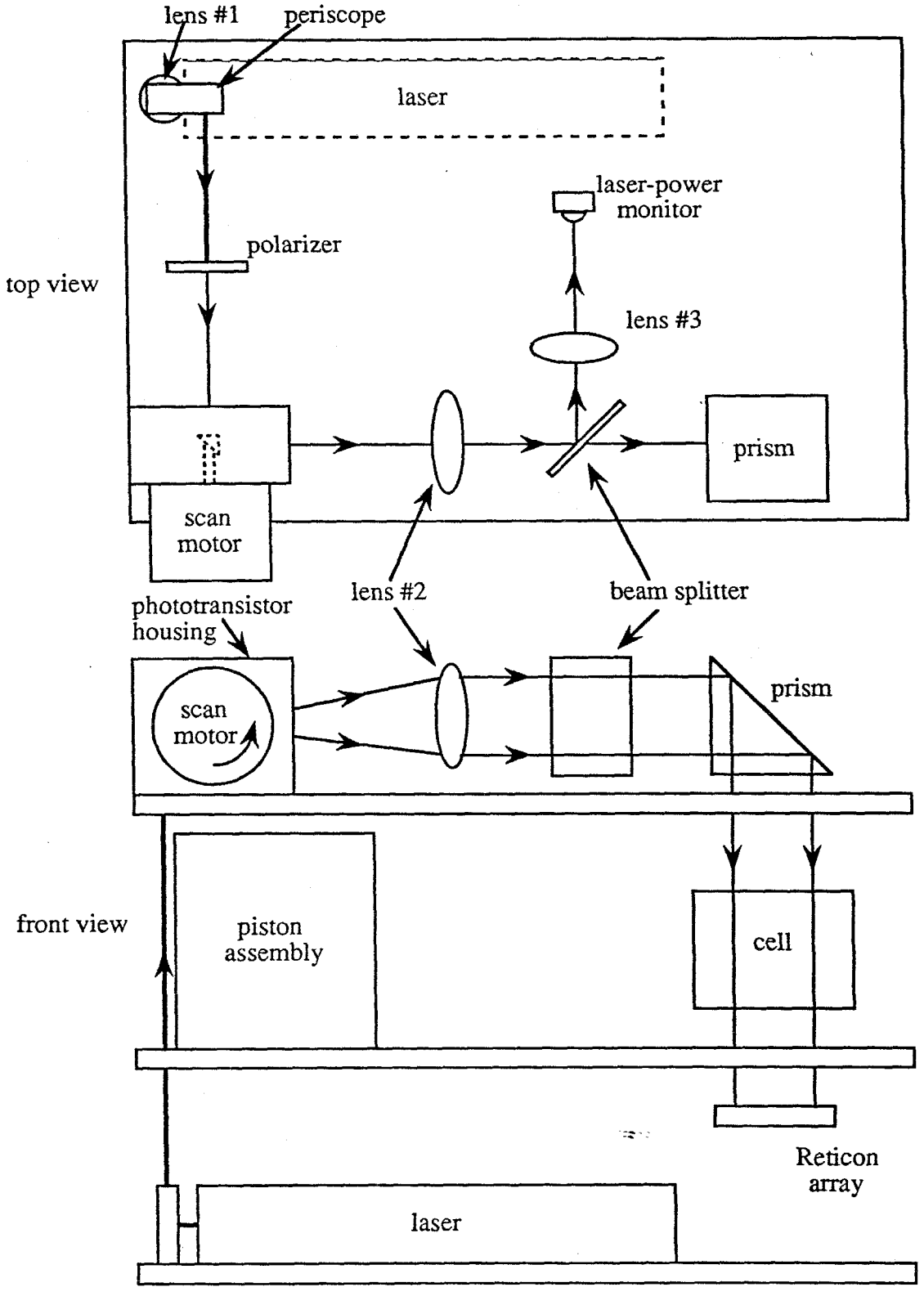

Fig. 4 Optical bench

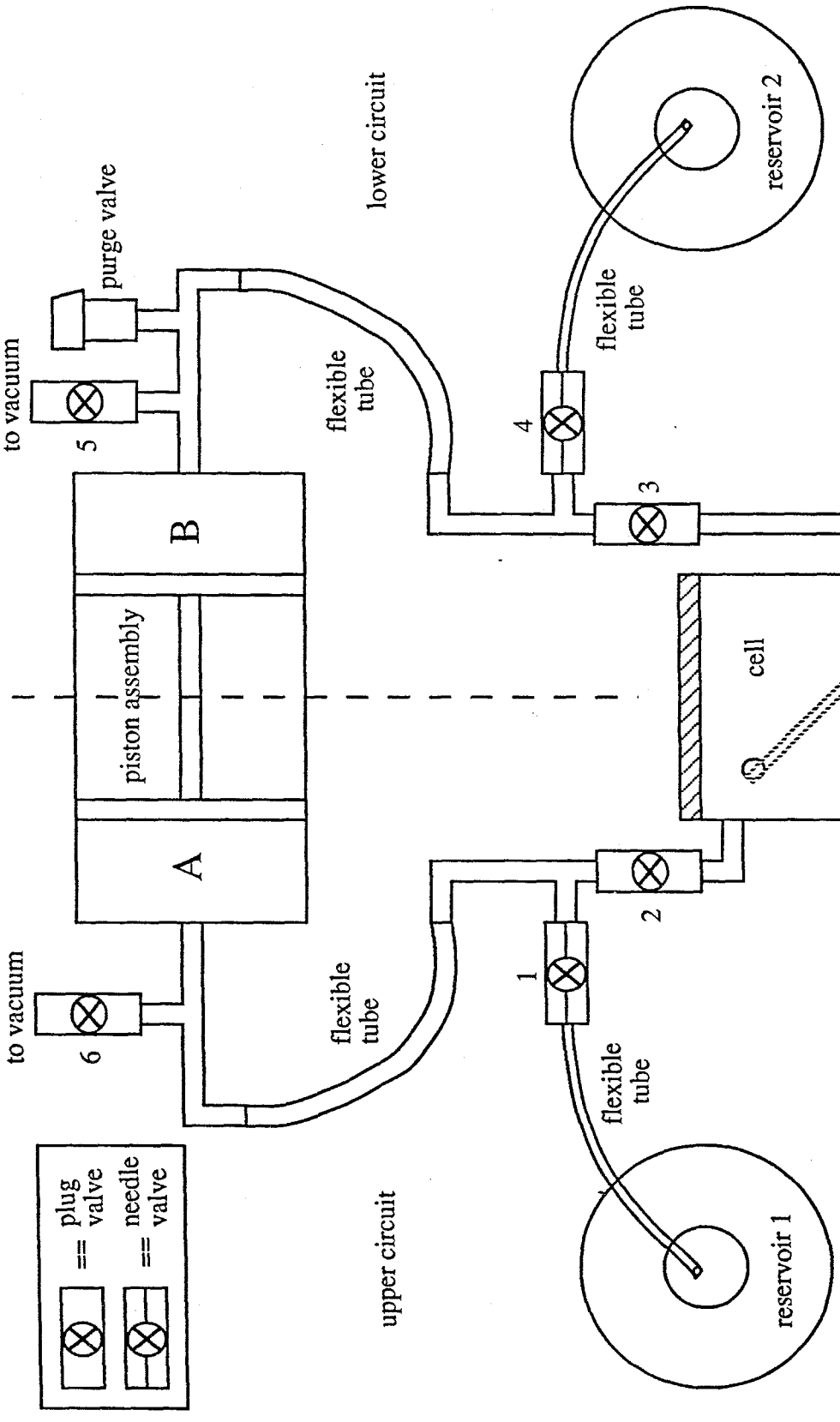

Fig. 5 Plumbing connections

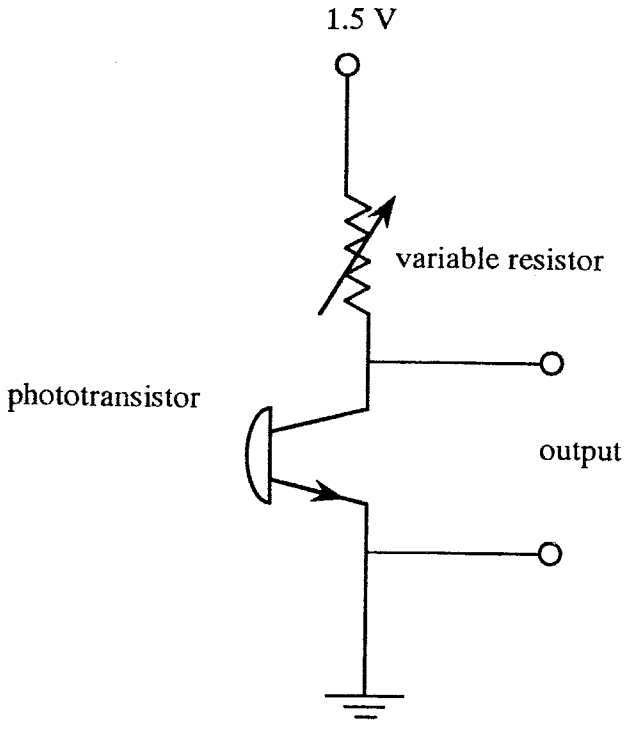

Fig. 6 Laser-power monitor circuit

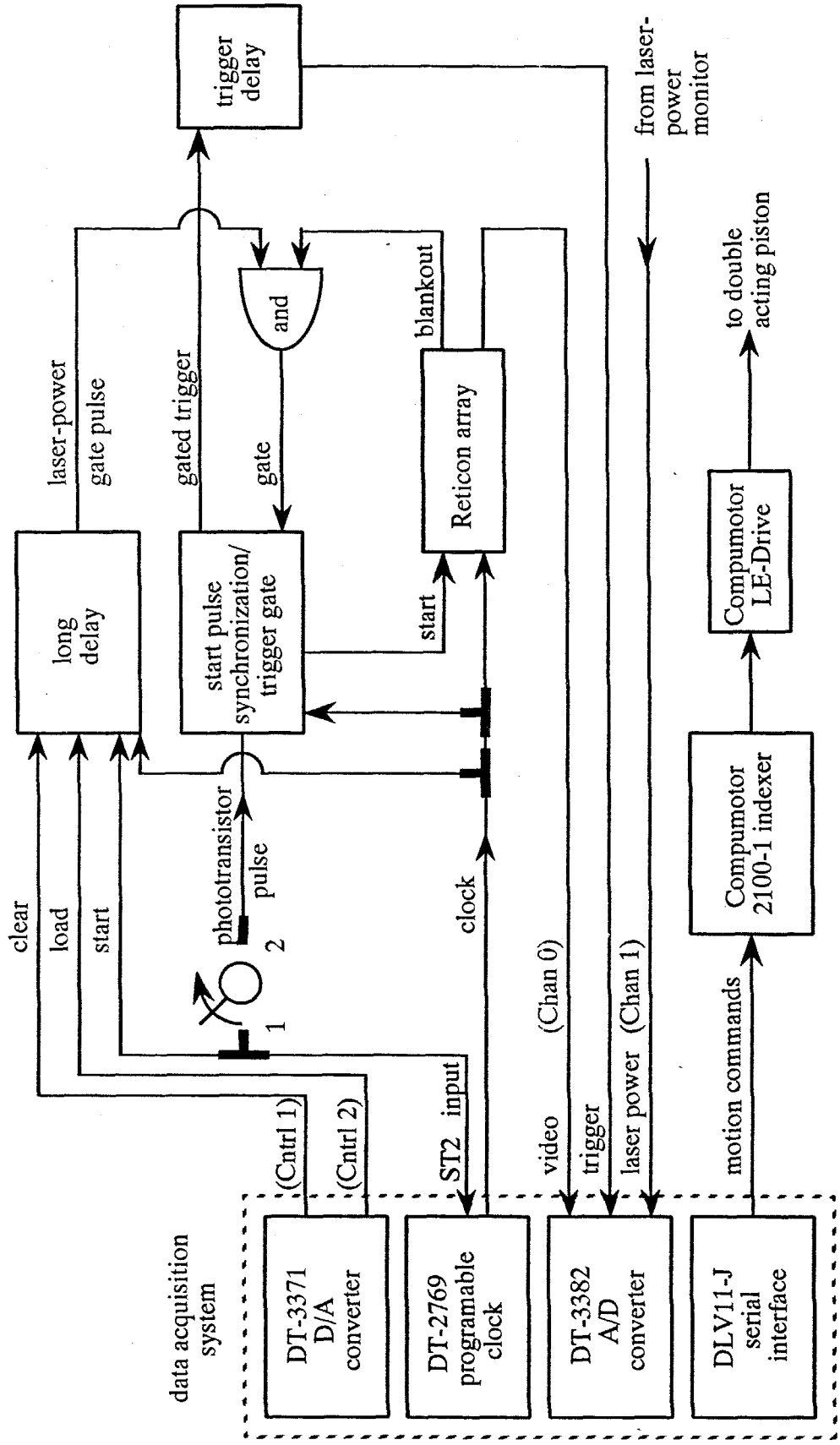

Fig. 7 Block diagram of device interconnection

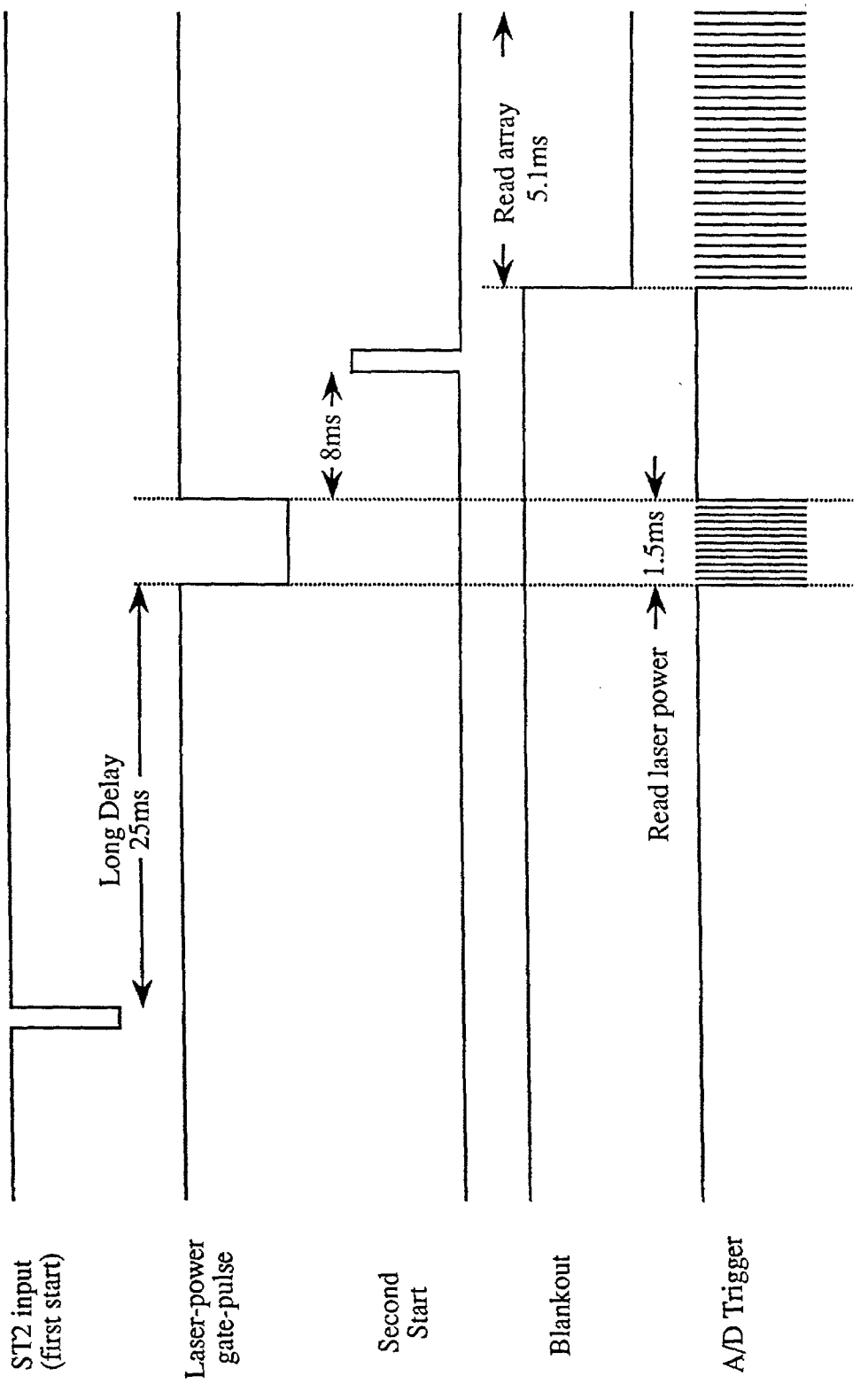

Fig. 8 Timing diagram for data acquisition

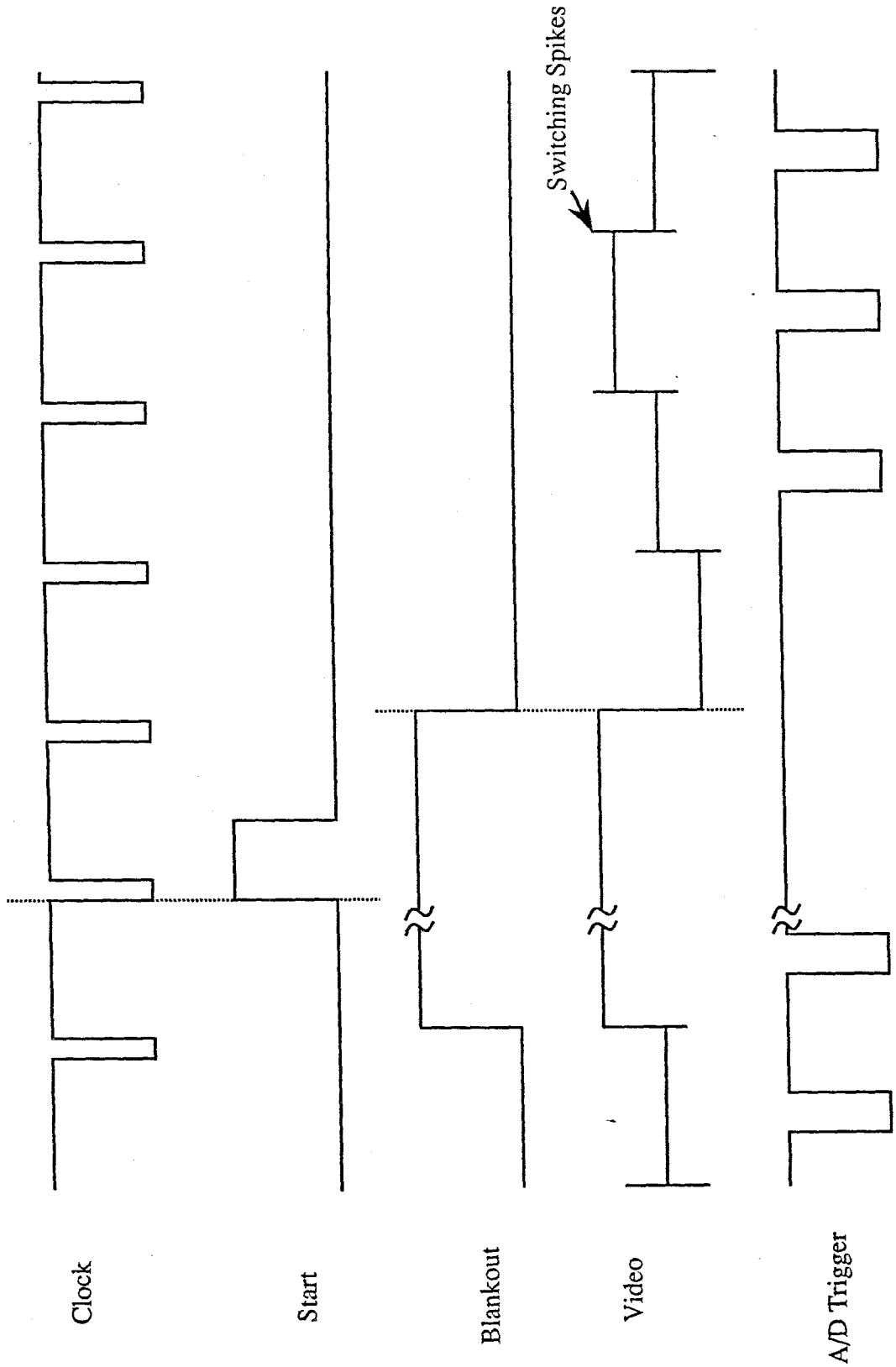

Fig. 9 Detail of Timing diagram for data acquisition

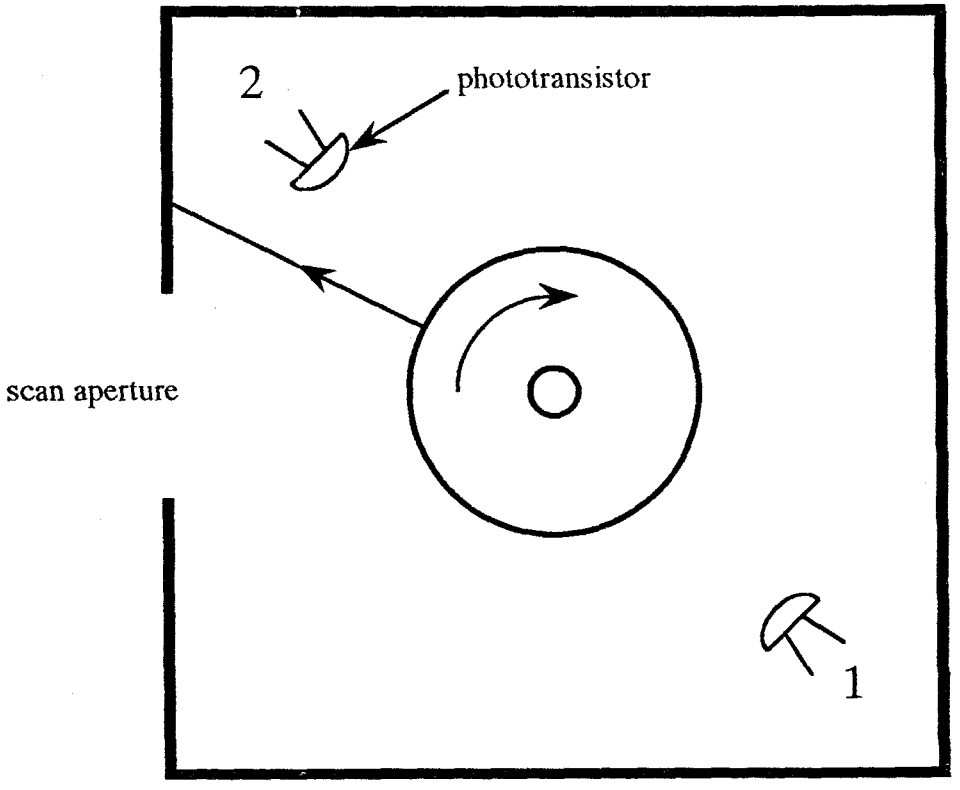

Fig. 10 Detail of phototransistor position

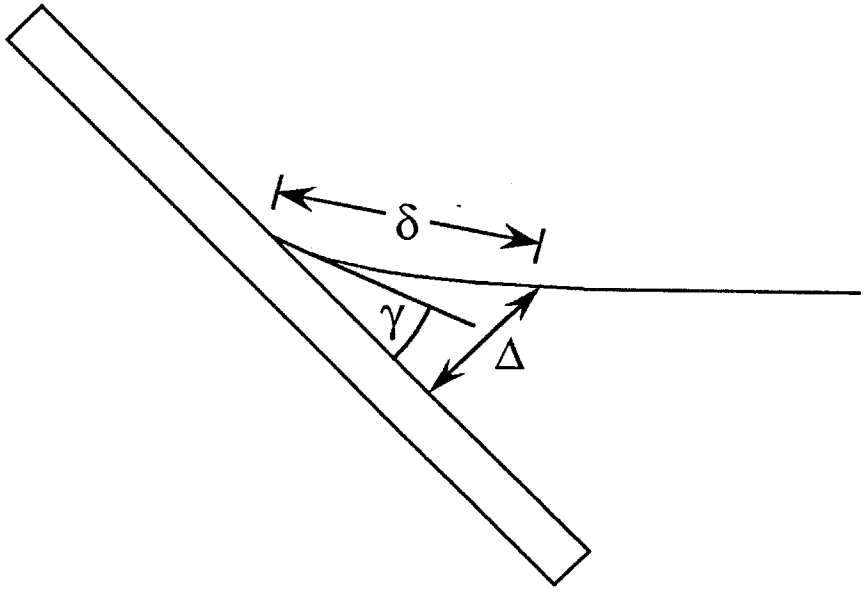

Fig 11 Contact line unwetting

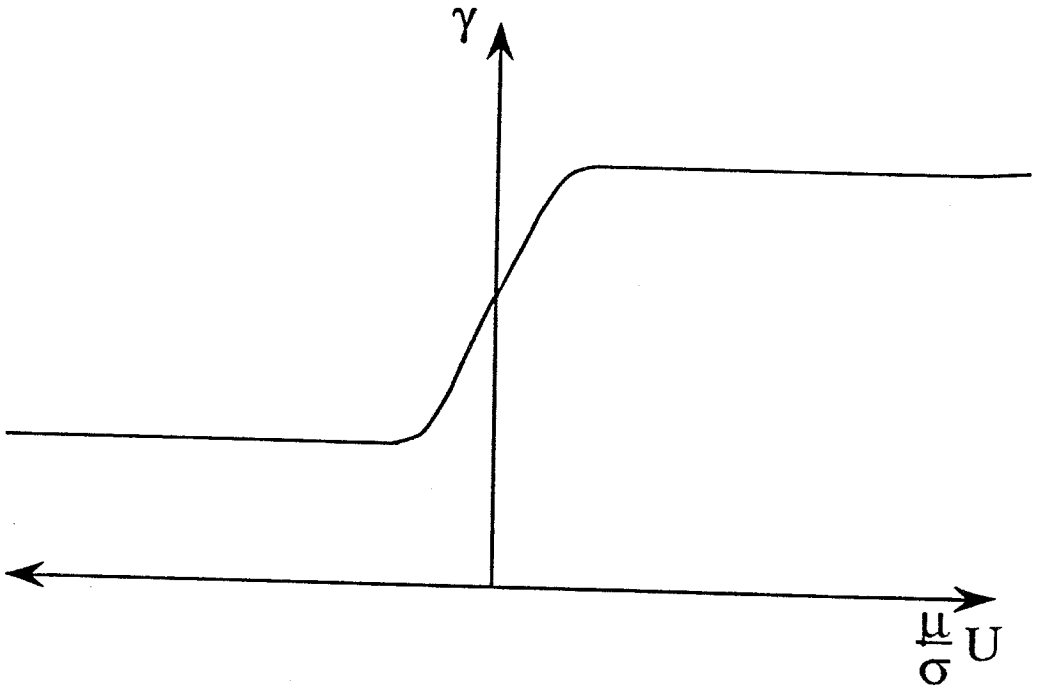

Fig. 12 Generic plot of contact angle vs. velocity

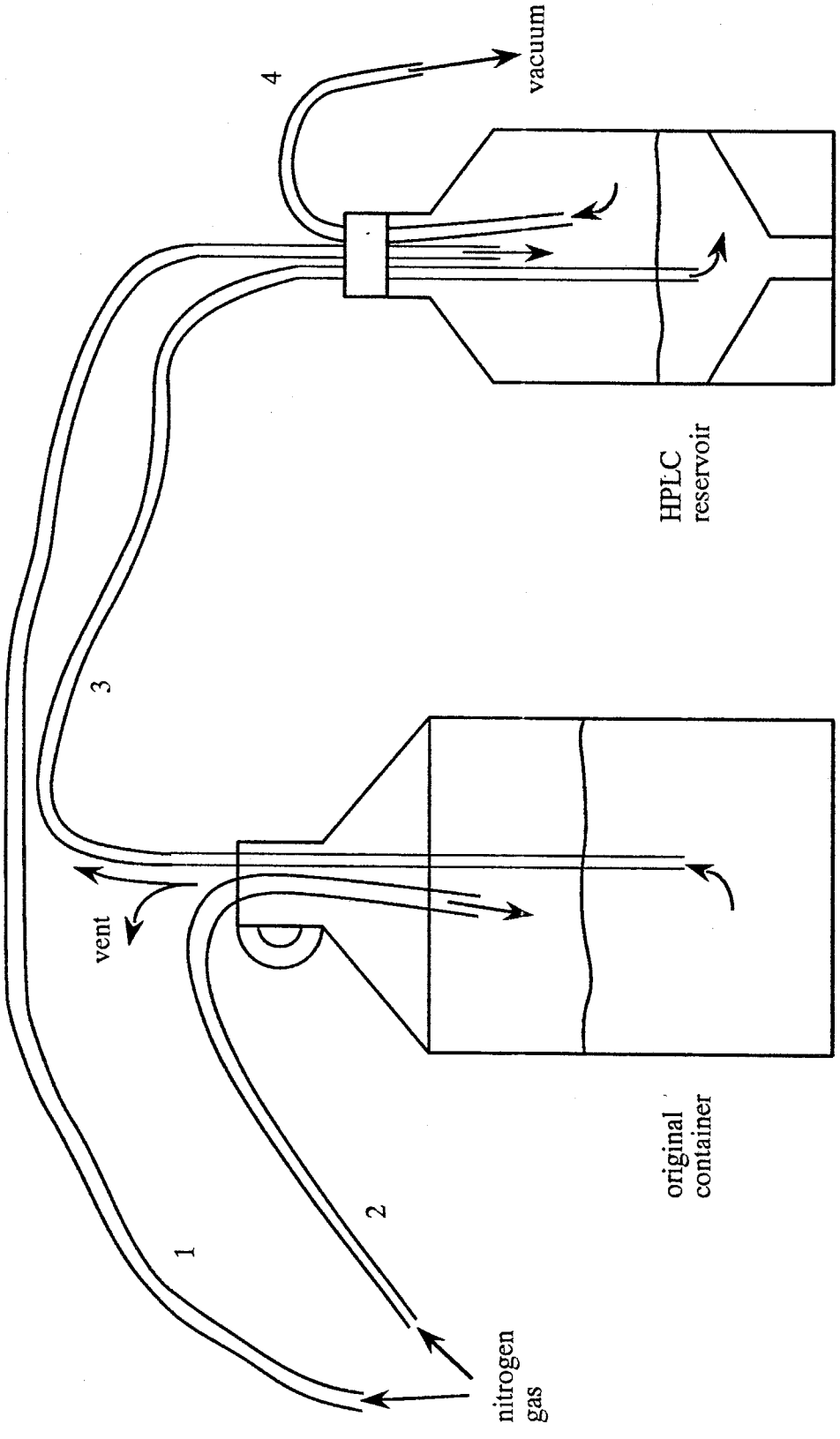

Fig. 13 Liquid transfer from original container to HPLC reservoir

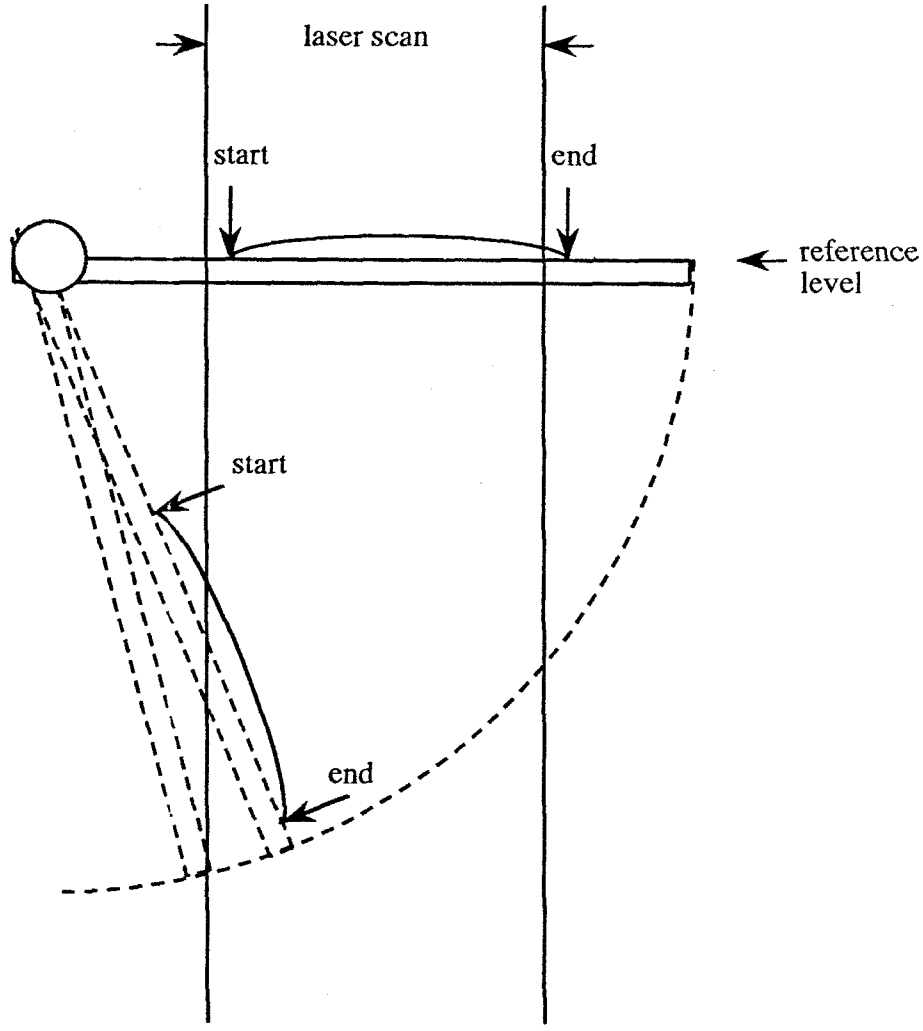

Figure 14 Measurement region on plate

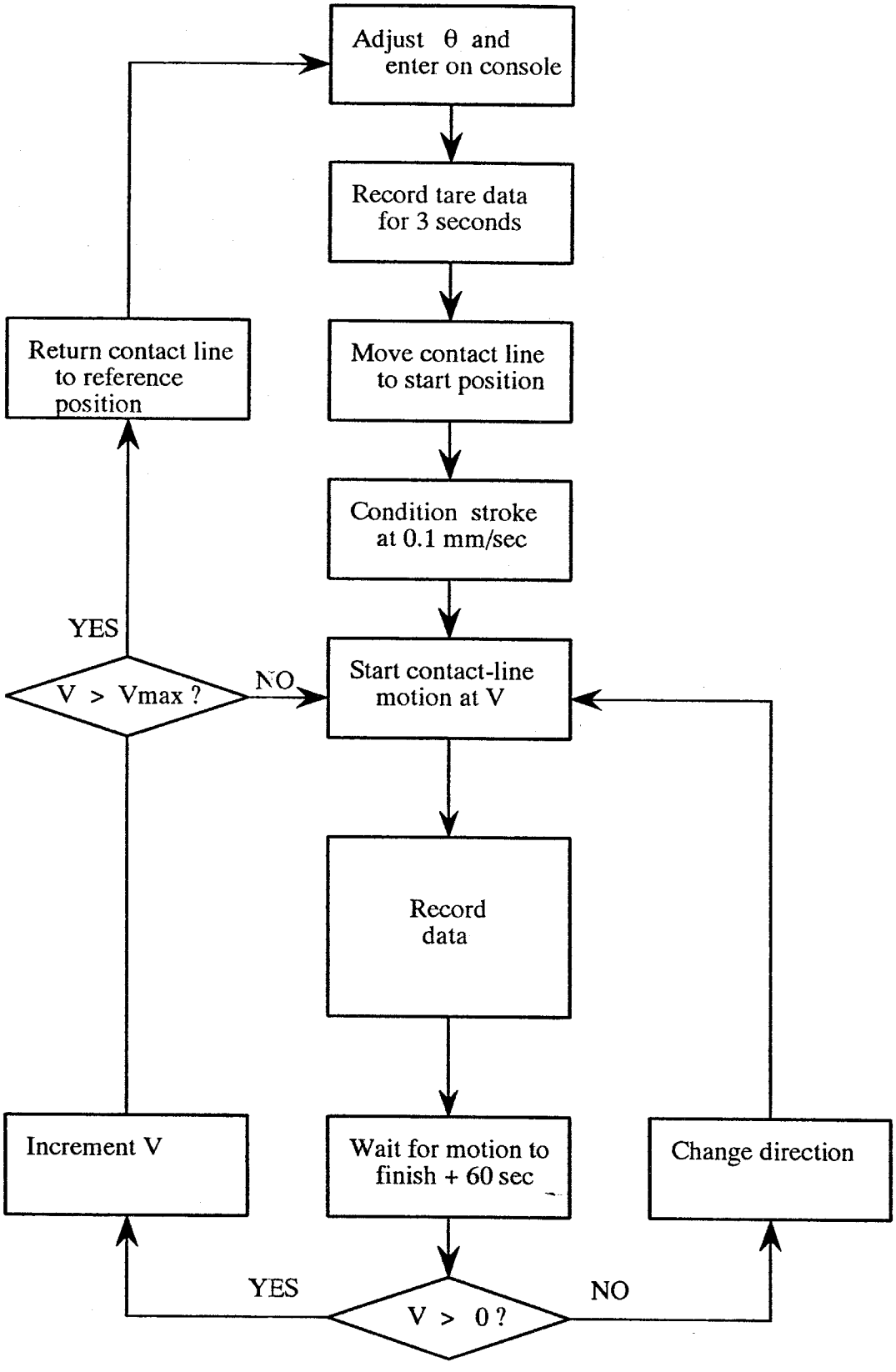

Fig. 15 Data acquisition flow chart

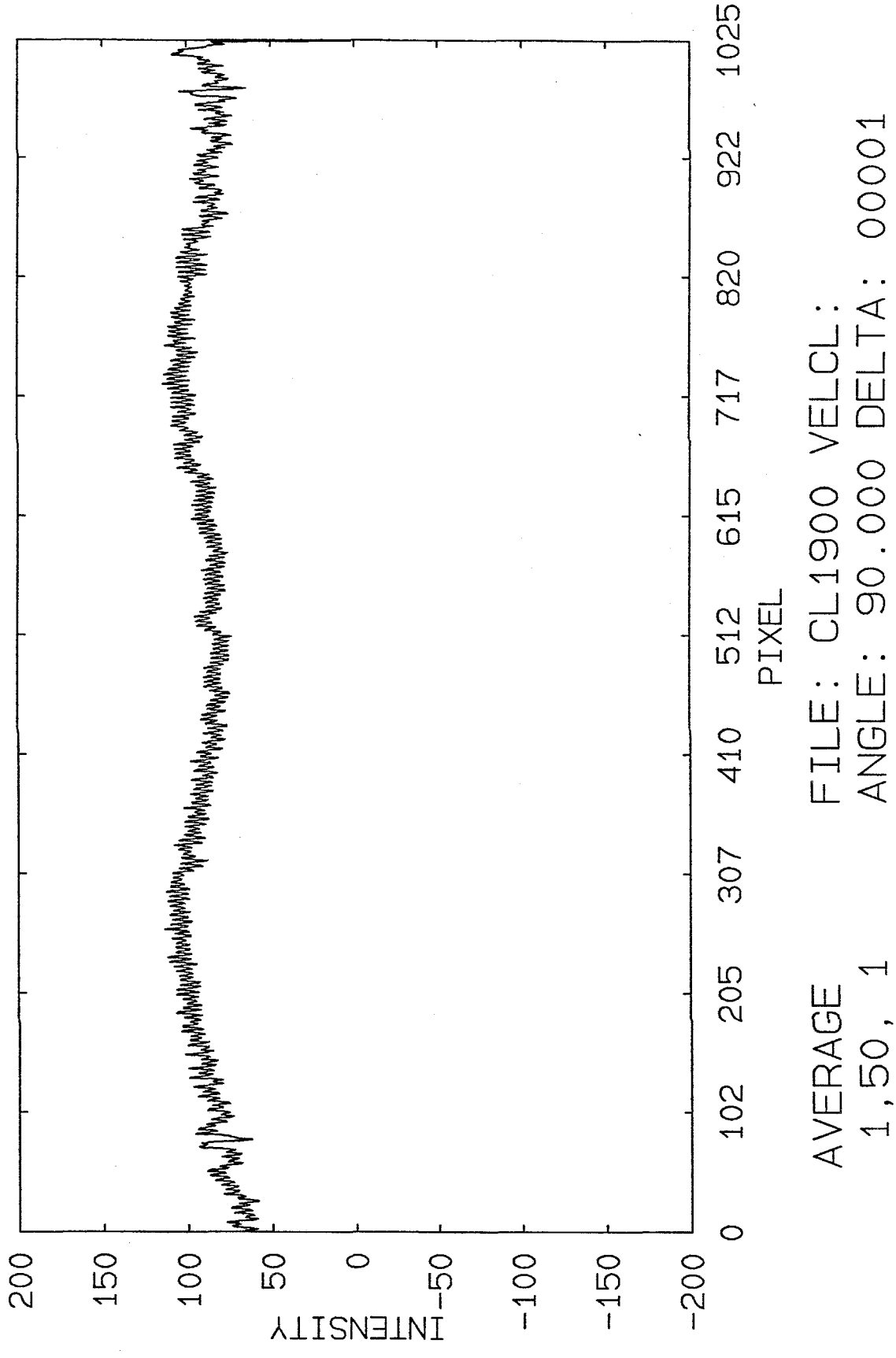
AVERAGE
1,50, 1
FILE: CL1900 VELCL:
ANGLE: 90.000 DELTA: 00001
INTENSITY
PIXEL
200
150
100
50
0
-50
-100
-150
-200
0
102
205
307
410
512
615
717
820
922
1025

Figure 16

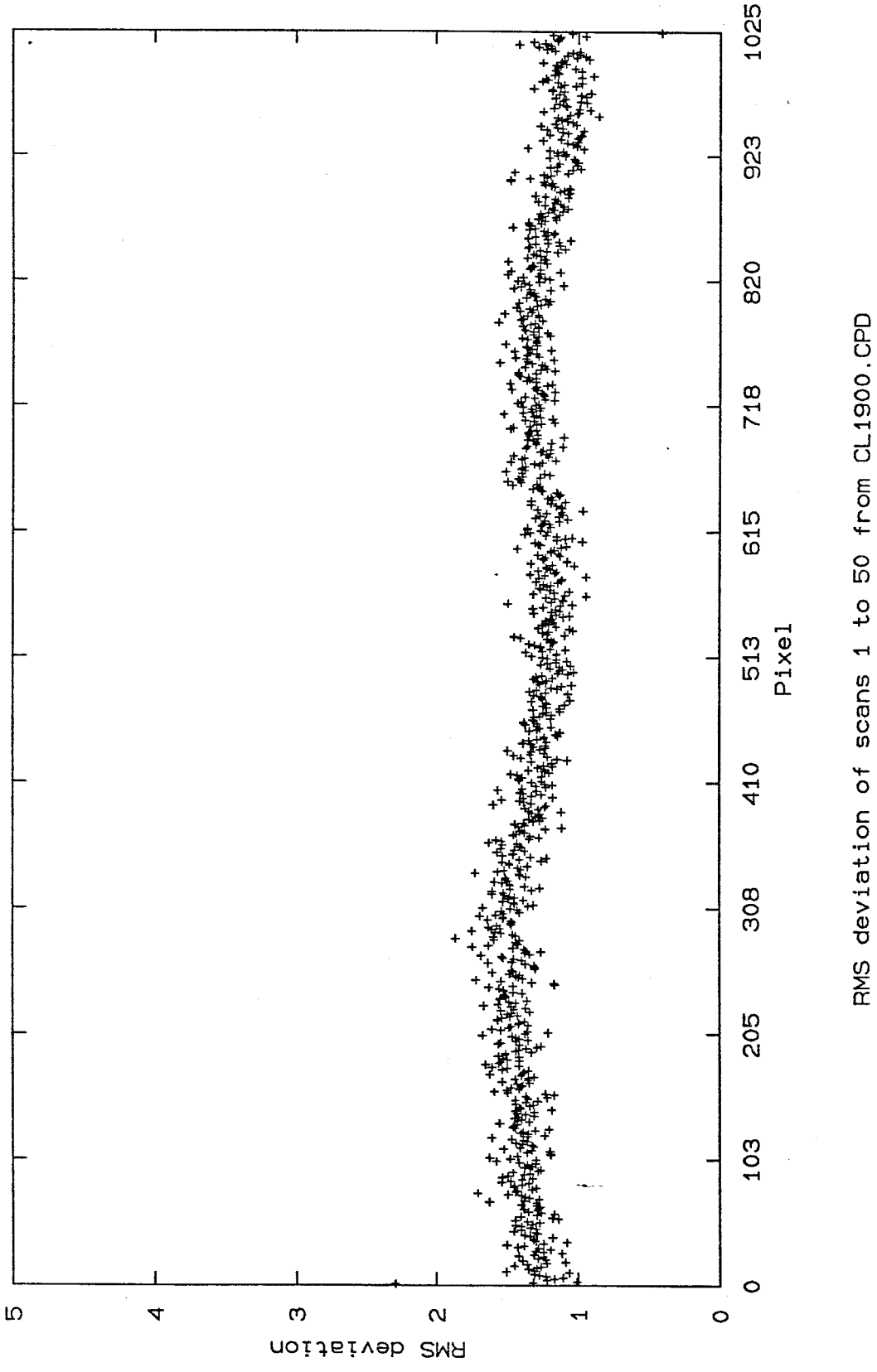
RMS deviation of scans 1 to 50 from CL1900.CPD
RMS deviation
Pixel
0
1
2
3
4
5
0
103
205
308
410
513
615
718
820
923
1025

Figure 17

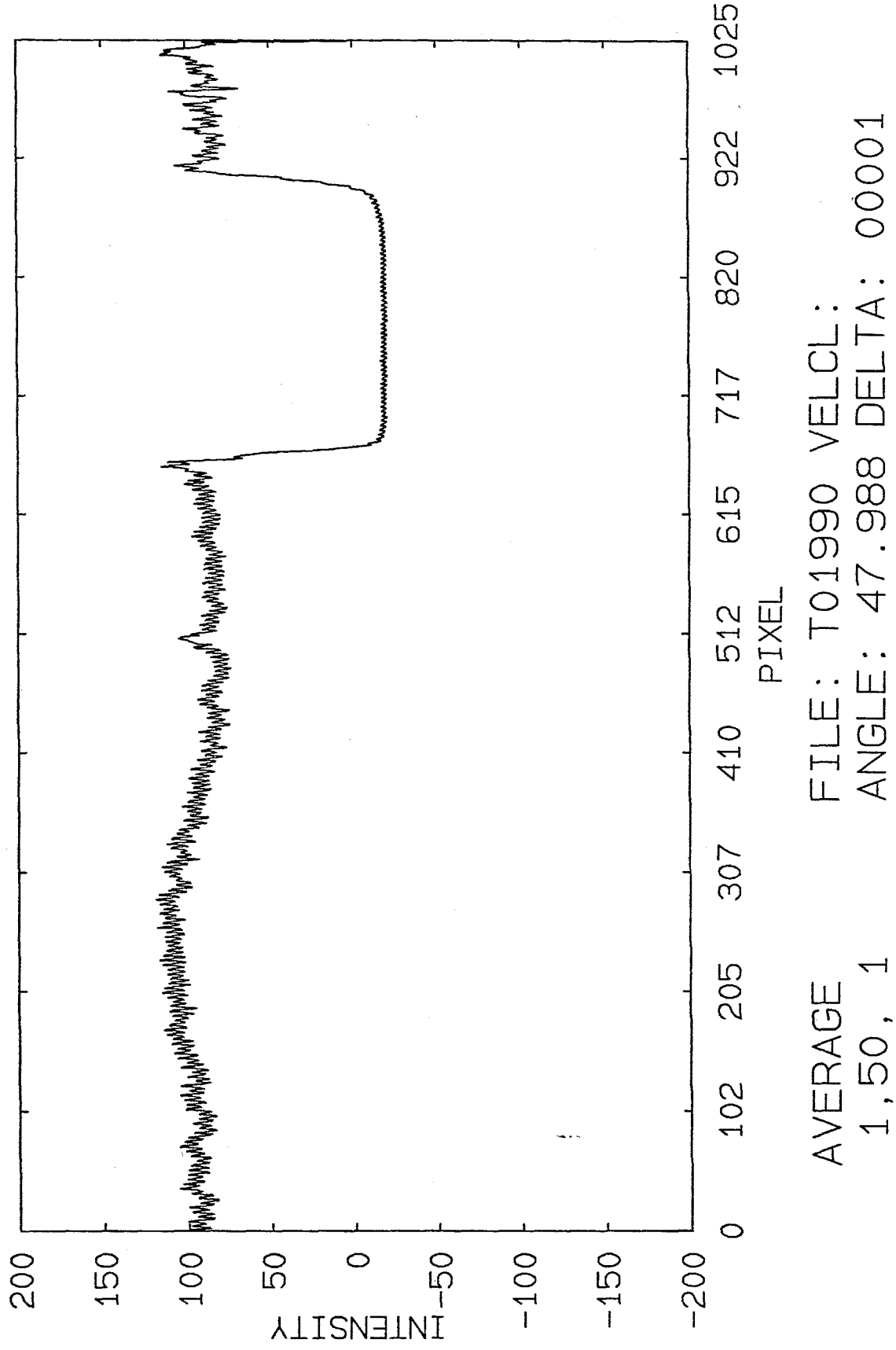
200
150
100
50
0
-50
-100
-150
-200
INTENSITY
0
102
205
307
410
512
615
717
820
922
1025
PIXEL
AVERAGE
1,50, 1
FILE: T01990 VELCL:
ANGLE: 47.988 DELTA: 00001

Figure 18

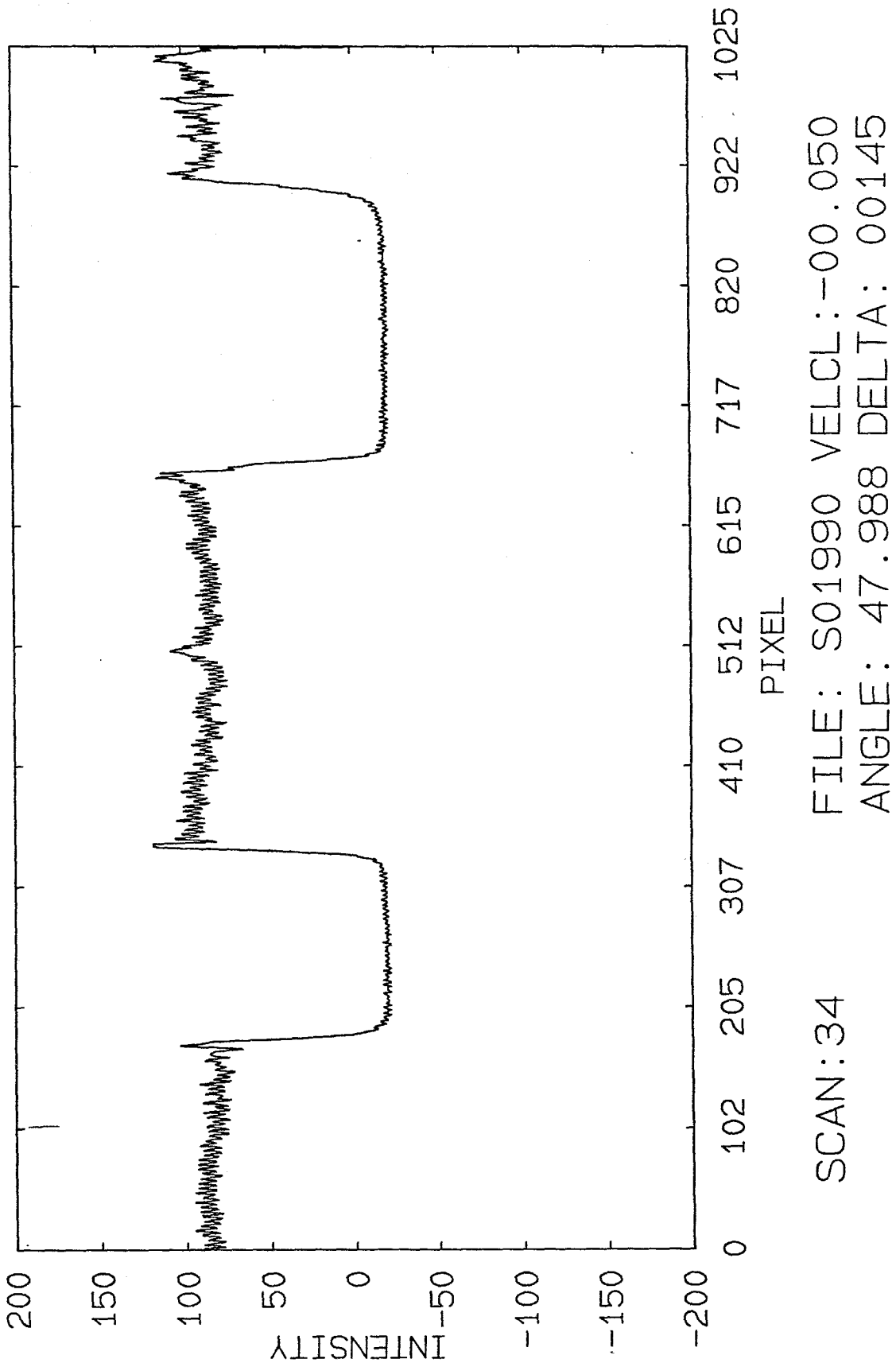
200
150
100
50
0
-50
-100
-150
-200
INTENSITY
0
102
205
307
410
512
615
717
820
922
1025
PIXEL
SCAN:34
FILE: S01990 VELCL:-00.050
ANGLE: 47.988 DELTA: 00145

Figure 19

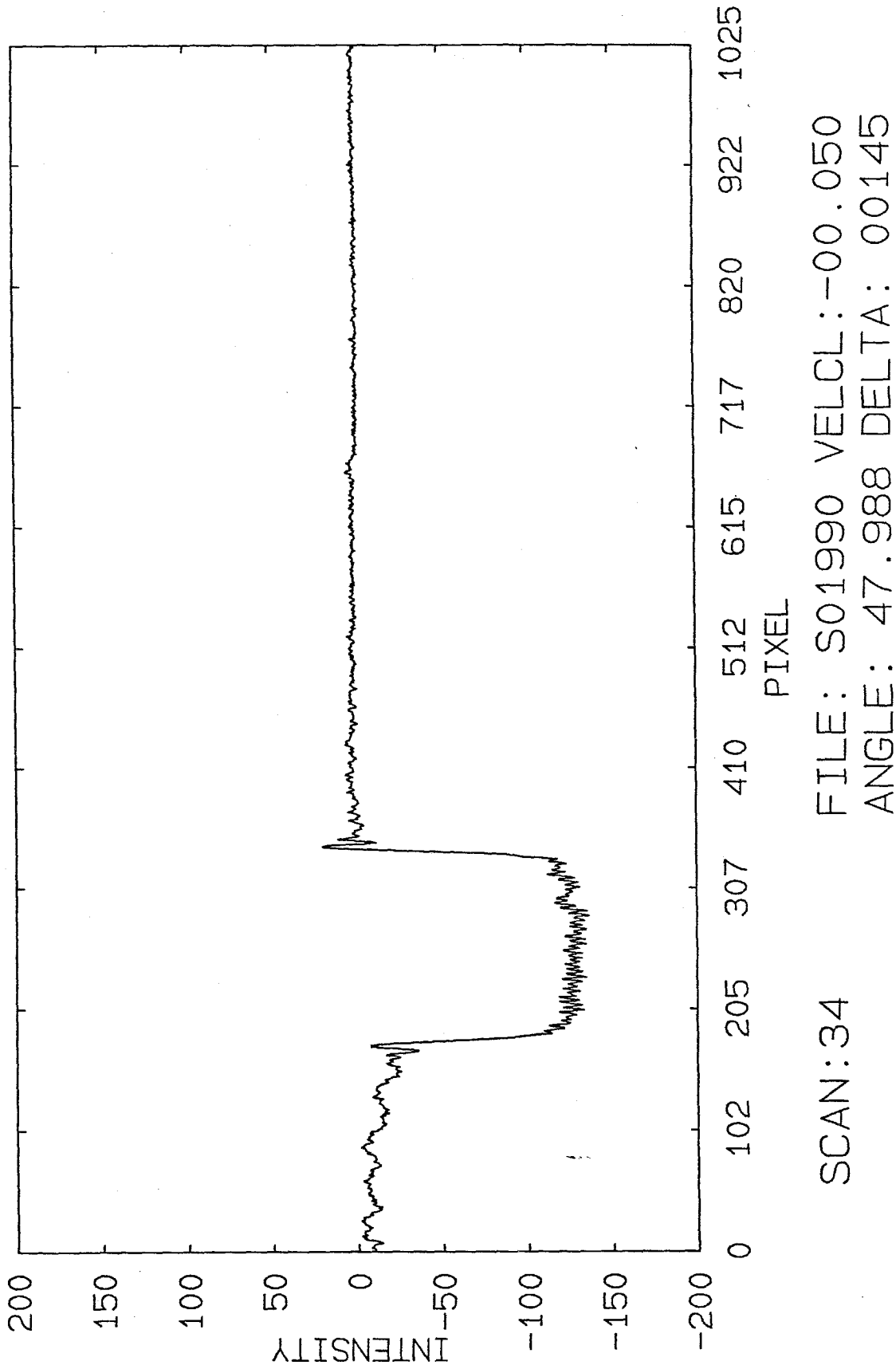
INTENSITY
200
150
100
50
0
-50
-100
-150
-200
0
102
205
307
410
512
615
717
820
922
1025
PIXEL
SCAN:34
FILE: S01990 VELCL:-00.050
ANGLE: 47.988 DELTA: 00145

Figure 20

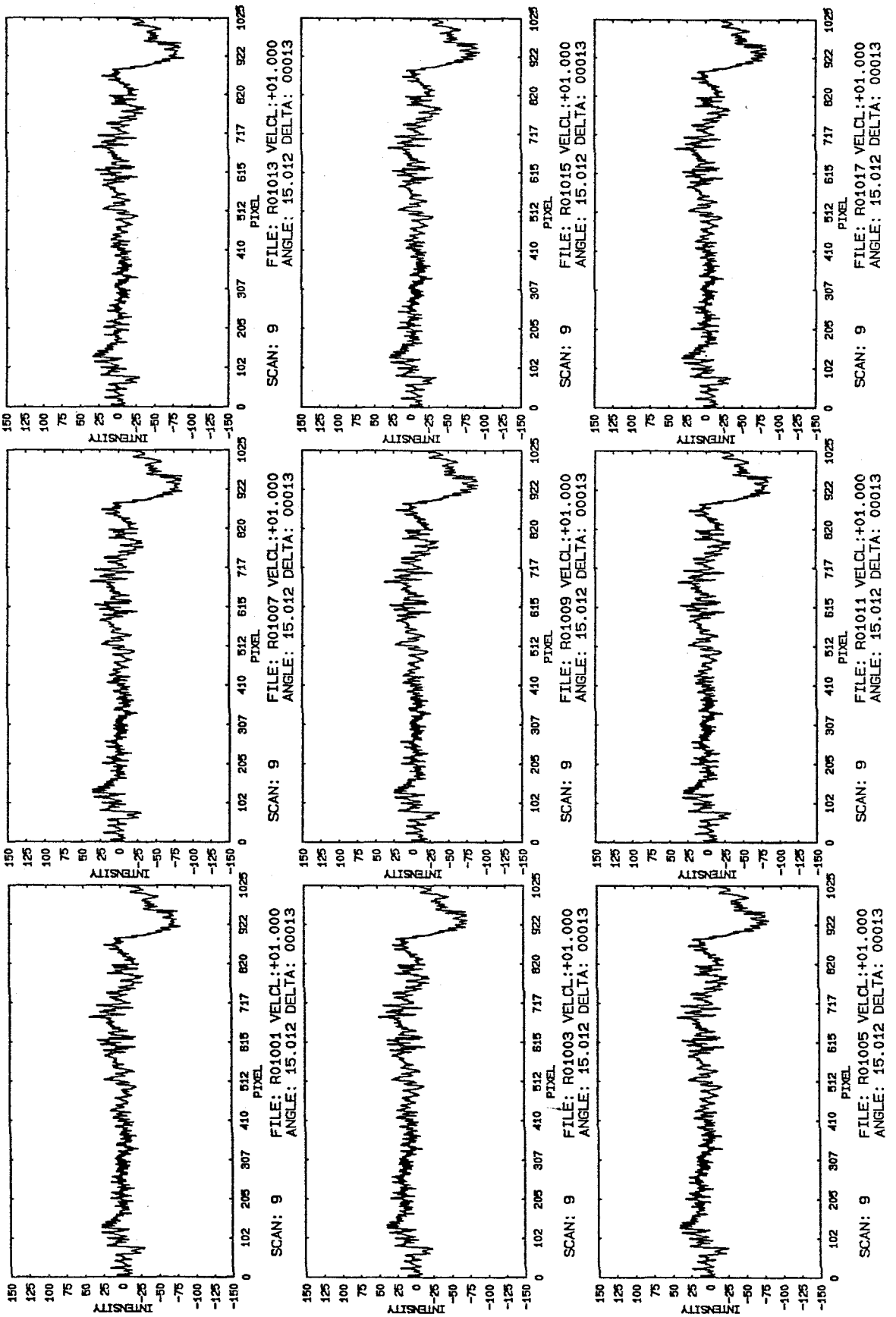
INTENSITY
PIXEL
SCAN: 9
FILE: R01001 VELCL:+01.000
ANGLE: 15.012 DELTA: 00013
FILE: R01003 VELCL:+01.000
ANGLE: 15.012 DELTA: 00013
FILE: R01005 VELCL:+01.000
ANGLE: 15.012 DELTA: 00013
FILE: R01007 VELCL:+01.000
ANGLE: 15.012 DELTA: 00013
FILE: R01009 VELCL:+01.000
ANGLE: 15.012 DELTA: 00013
FILE: R01011 VELCL:+01.000
ANGLE: 15.012 DELTA: 00013
FILE: R01013 VELCL:+01.000
ANGLE: 15.012 DELTA: 00013
FILE: R01015 VELCL:+01.000
ANGLE: 15.012 DELTA: 00013
FILE: R01017 VELCL:+01.000
ANGLE: 15.012 DELTA: 00013

Figure 21

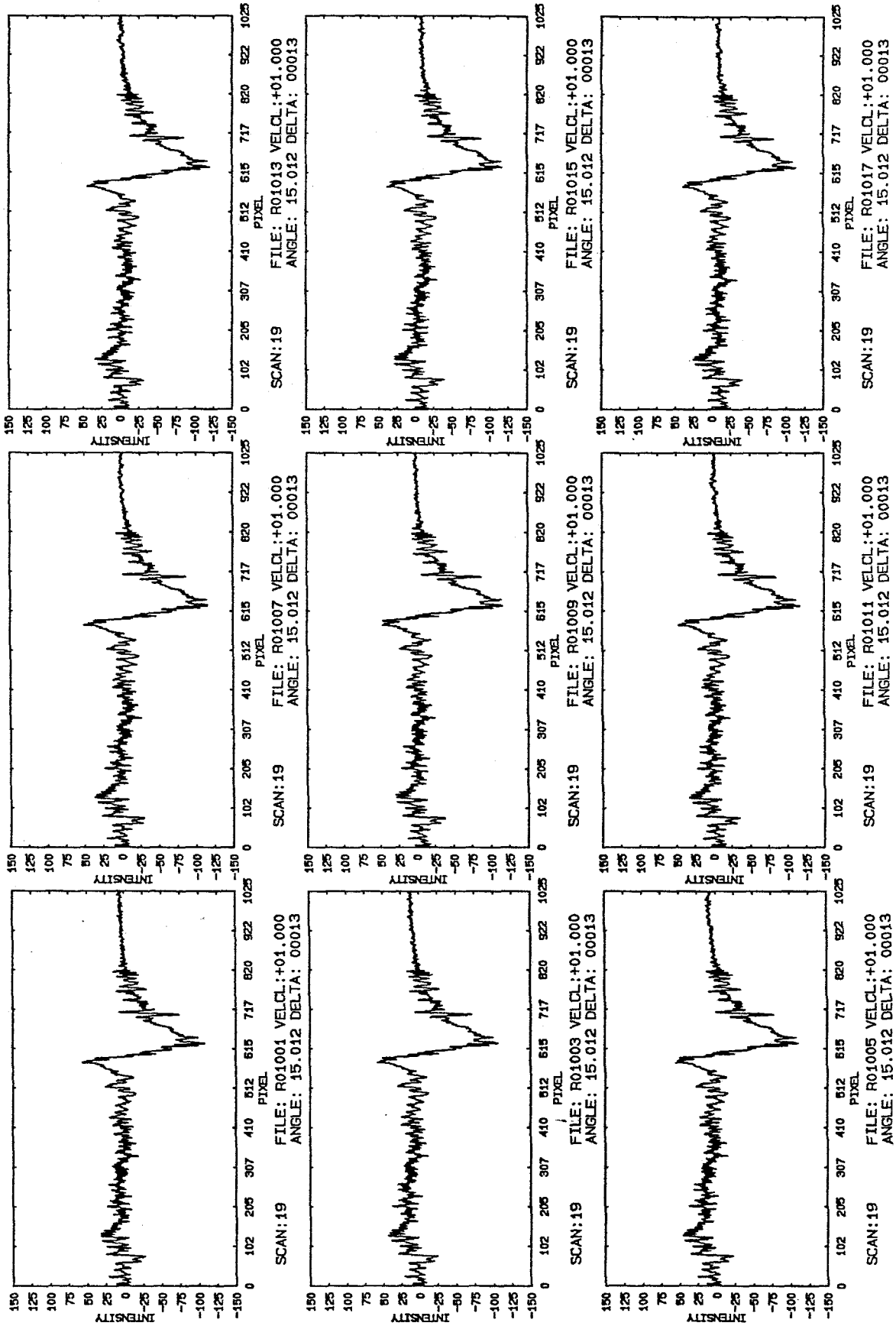
INTENSITY
PIXEL
SCAN:19
FILE: R01001 VELCL:+01.000
ANGLE: 15.012 DELTA: 00013
FILE: R01003 VELCL:+01.000
ANGLE: 15.012 DELTA: 00013
FILE: R01005 VELCL:+01.000
ANGLE: 15.012 DELTA: 00013
FILE: R01007 VELCL:+01.000
ANGLE: 15.012 DELTA: 00013
FILE: R01009 VELCL:+01.000
ANGLE: 15.012 DELTA: 00013
FILE: R01011 VELCL:+01.000
ANGLE: 15.012 DELTA: 00013
FILE: R01013 VELCL:+01.000
ANGLE: 15.012 DELTA: 00013
FILE: R01015 VELCL:+01.000
ANGLE: 15.012 DELTA: 00013
FILE: R01017 VELCL:+01.000
ANGLE: 15.012 DELTA: 00013

Figure 22

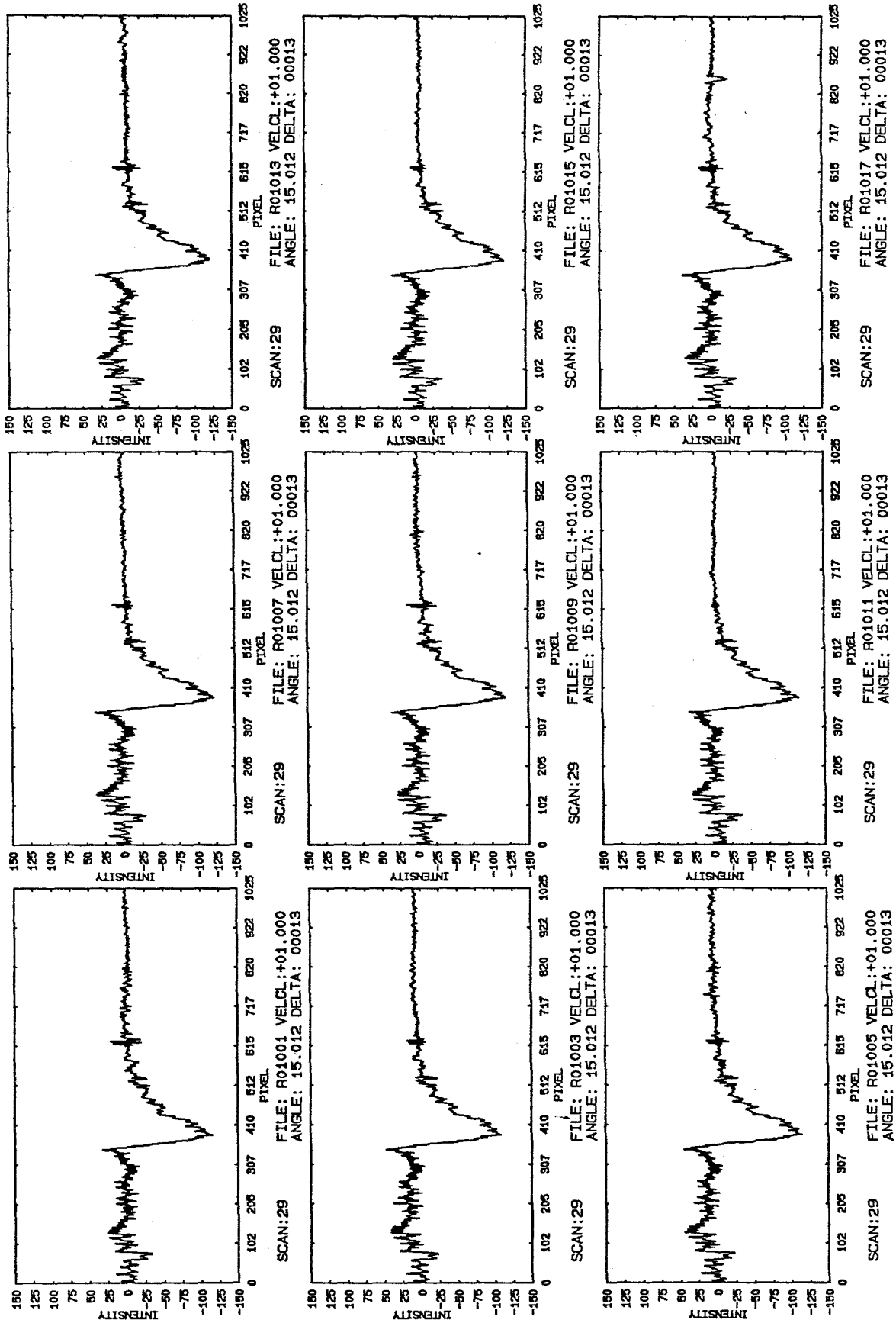
INTENSITY
PIXEL
SCAN:29
FILE: R01001 VELCL:+01.000
ANGLE: 15.012 DELTA: 00013
FILE: R01003 VELCL:+01.000
ANGLE: 15.012 DELTA: 00013
FILE: R01005 VELCL:+01.000
ANGLE: 15.012 DELTA: 00013
FILE: R01007 VELCL:+01.000
ANGLE: 15.012 DELTA: 00013
FILE: R01009 VELCL:+01.000
ANGLE: 15.012 DELTA: 00013
FILE: R01011 VELCL:+01.000
ANGLE: 15.012 DELTA: 00013
FILE: R01013 VELCL:+01.000
ANGLE: 15.012 DELTA: 00013
FILE: R01015 VELCL:+01.000
ANGLE: 15.012 DELTA: 00013
FILE: R01017 VELCL:+01.000
ANGLE: 15.012 DELTA: 00013

Figure 23

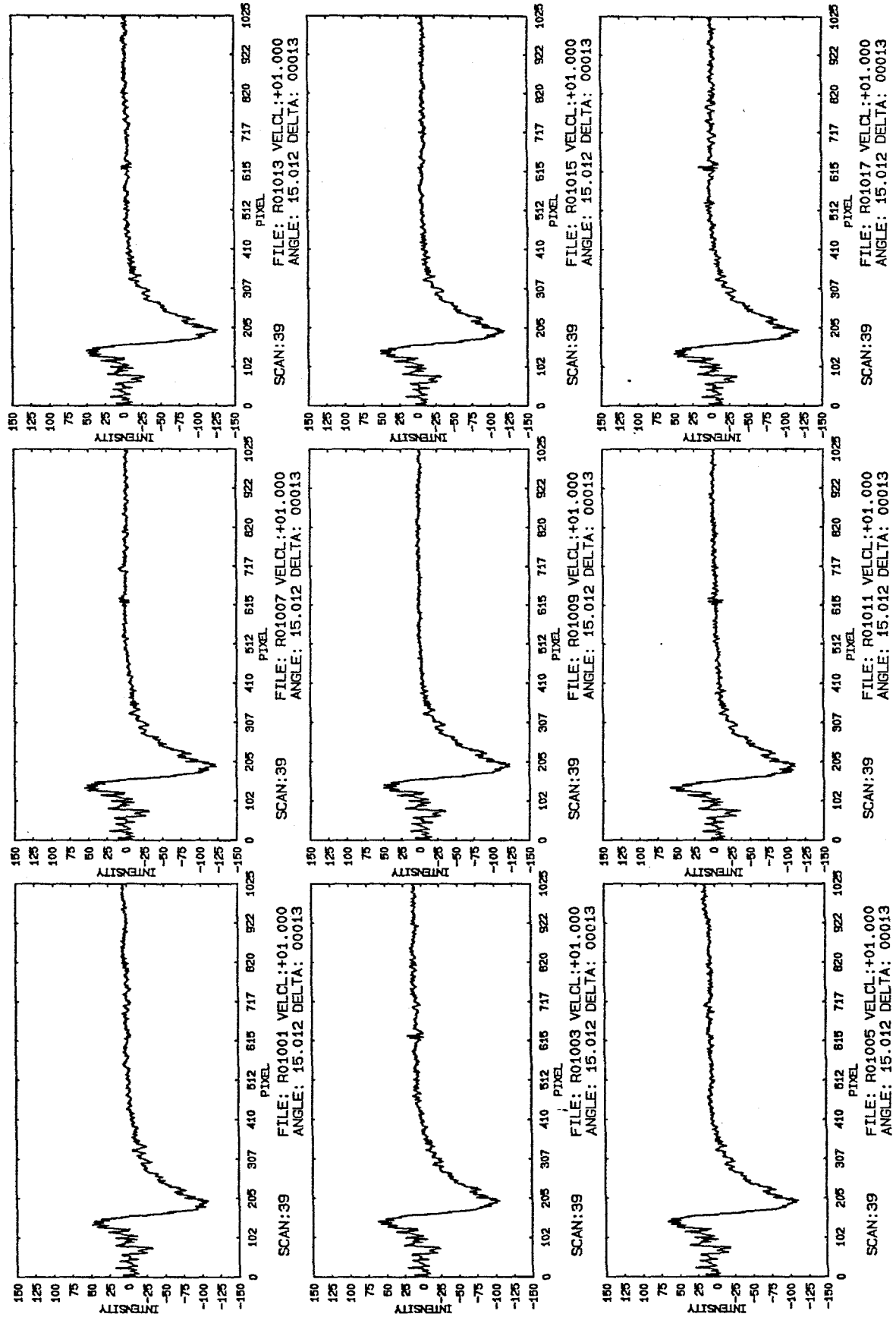
INTENSITY
PIXEL
SCAN:39
FILE: R01001 VELCL:+01.000
ANGLE: 15.012 DELTA: 00013
FILE: R01003 VELCL:+01.000
FILE: R01005 VELCL:+01.000
FILE: R01007 VELCL:+01.000
FILE: R01009 VELCL:+01.000
FILE: R01011 VELCL:+01.000
FILE: R01013 VELCL:+01.000
FILE: R01015 VELCL:+01.000
FILE: R01017 VELCL:+01.000

Figure 24

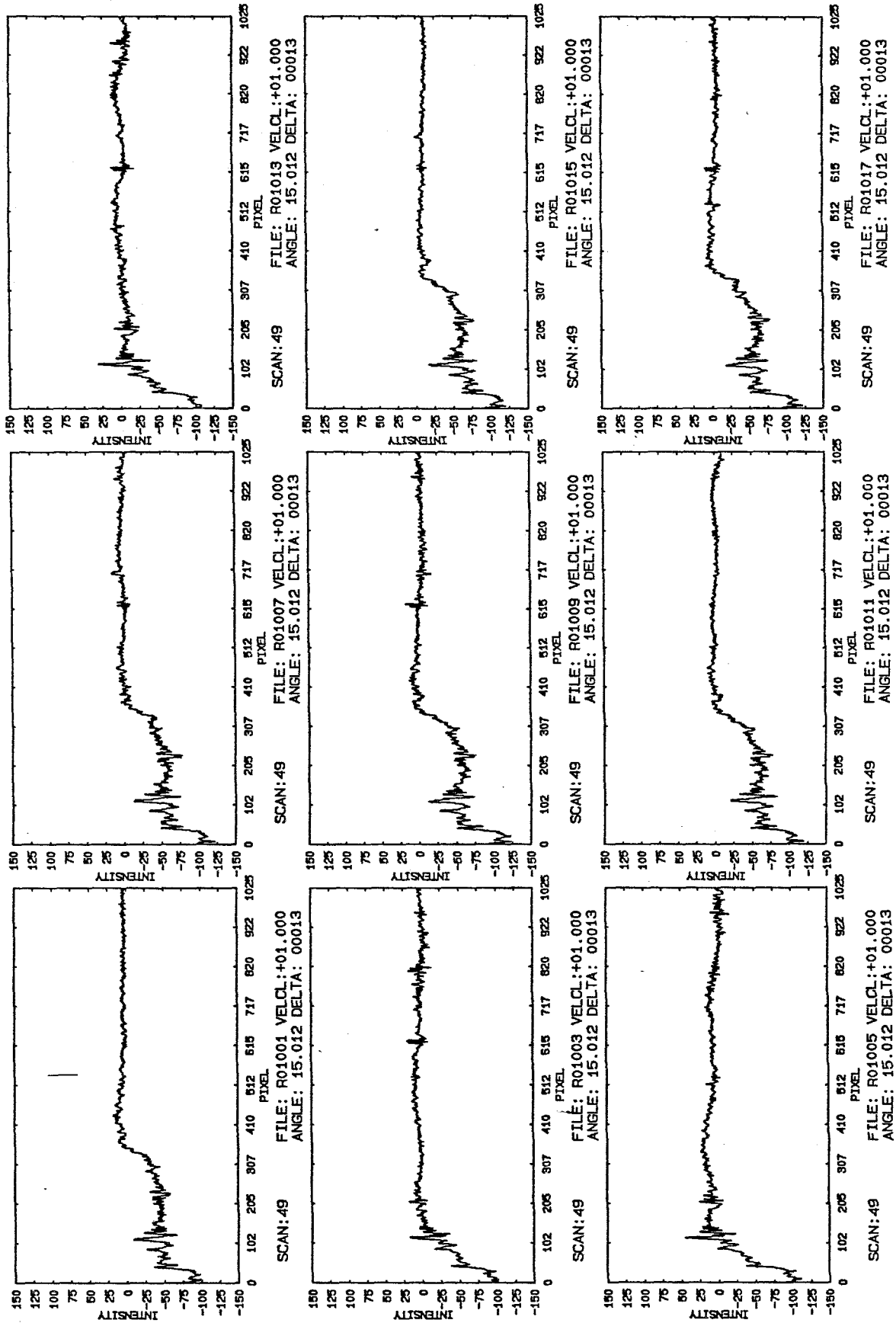
INTENSITY
PIXEL
SCAN:49
FILE: R01001 VELCL:+01.000
ANGLE: 15.012 DELTA: 00013
FILE: R01003 VELCL:+01.000
ANGLE: 15.012 DELTA: 00013
FILE: R01005 VELCL:+01.000
ANGLE: 15.012 DELTA: 00013
FILE: R01007 VELCL:+01.000
ANGLE: 15.012 DELTA: 00013
FILE: R01009 VELCL:+01.000
ANGLE: 15.012 DELTA: 00013
FILE: R01011 VELCL:+01.000
ANGLE: 15.012 DELTA: 00013
FILE: R01013 VELCL:+01.000
ANGLE: 15.012 DELTA: 00013
FILE: R01015 VELCL:+01.000
ANGLE: 15.012 DELTA: 00013
FILE: R01017 VELCL:+01.000
ANGLE: 15.012 DELTA: 00013

Figure 25

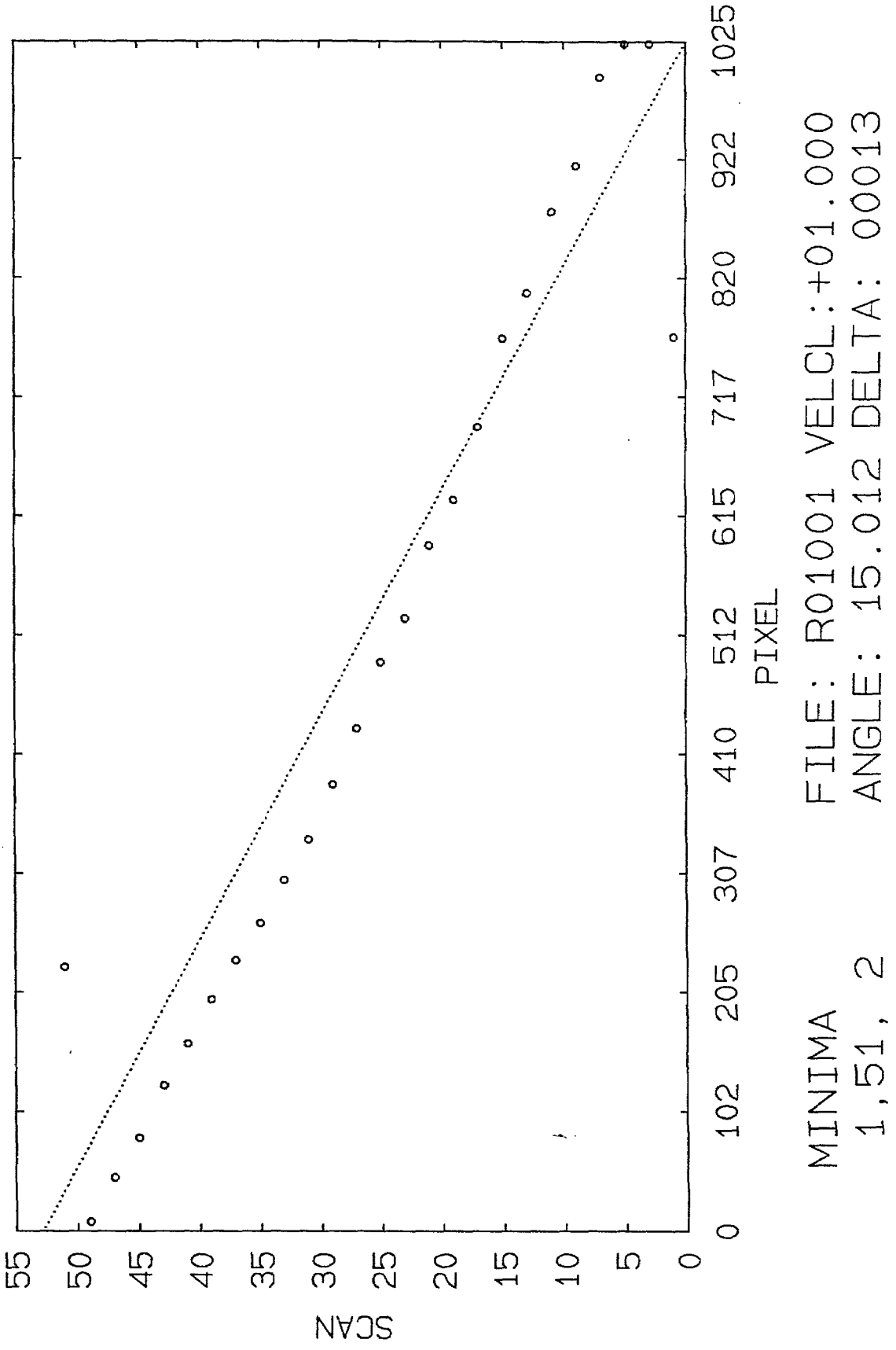
FILE: R01001 VELCL:+01.000
ANGLE: 15.012 DELTA: 00013
MINIMA
1,51, 2
SCAN
55
50
45
40
35
30
25
20
15
10
5
0
0
102
205
307
410
512
615
717
820
922
1025
PIXEL

Figure 26

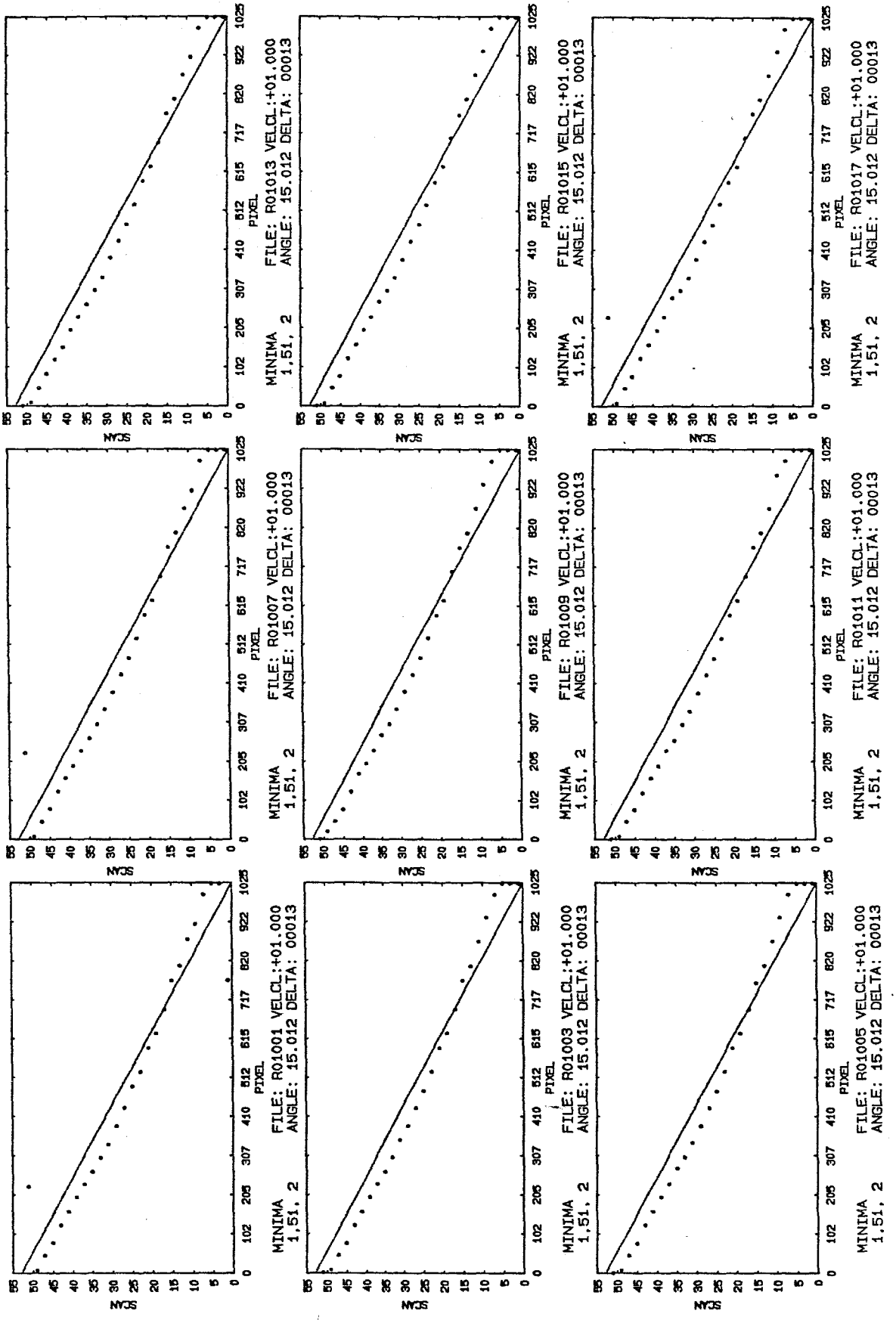
SCAN
PIXEL
MINIMA
1,51, 2
FILE: R01001 VELCL:+01.000
ANGLE: 15.012 DELTA: 00013
FILE: R01003 VELCL:+01.000
ANGLE: 15.012 DELTA: 00013
FILE: R01005 VELCL:+01.000
ANGLE: 15.012 DELTA: 00013
FILE: R01007 VELCL:+01.000
ANGLE: 15.012 DELTA: 00013
FILE: R01009 VELCL:+01.000
ANGLE: 15.012 DELTA: 00013
FILE: R01011 VELCL:+01.000
ANGLE: 15.012 DELTA: 00013
FILE: R01013 VELCL:+01.000
ANGLE: 15.012 DELTA: 00013
FILE: R01015 VELCL:+01.000
ANGLE: 15.012 DELTA: 00013
FILE: R01017 VELCL:+01.000
ANGLE: 15.012 DELTA: 00013

Figure 27

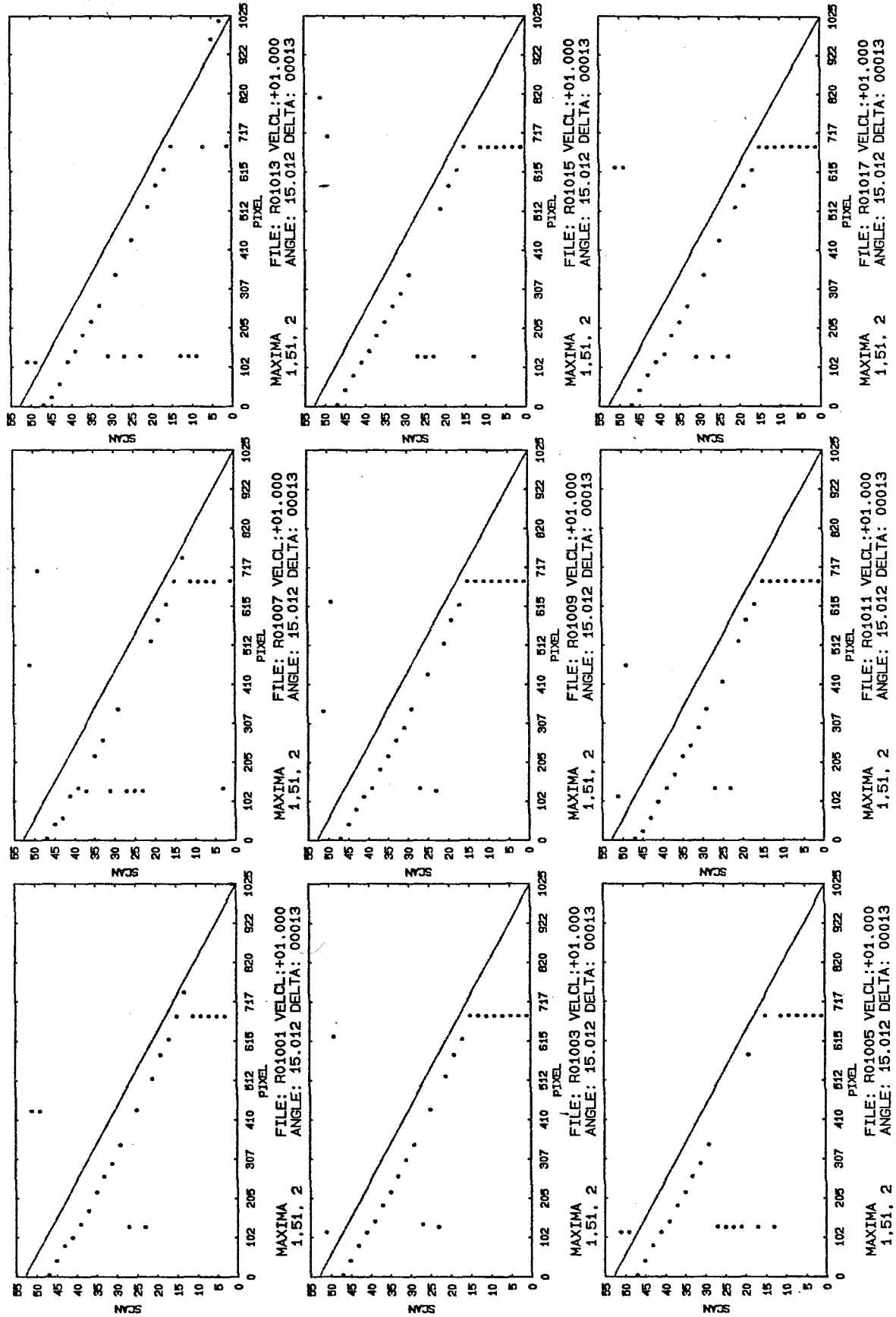
FILE: R01001 VELCL:+01.000
ANGLE: 15.012 DELTA: 00013
MAXIMA
1,51, 2
FILE: R01003 VELCL:+01.000
ANGLE: 15.012 DELTA: 00013
MAXIMA
1,51, 2
FILE: R01005 VELCL:+01.000
ANGLE: 15.012 DELTA: 00013
MAXIMA
1,51, 2
FILE: R01007 VELCL:+01.000
ANGLE: 15.012 DELTA: 00013
MAXIMA
1,51, 2
FILE: R01009 VELCL:+01.000
ANGLE: 15.012 DELTA: 00013
MAXIMA
1,51, 2
FILE: R01011 VELCL:+01.000
ANGLE: 15.012 DELTA: 00013
MAXIMA
1,51, 2
FILE: R01013 VELCL:+01.000
ANGLE: 15.012 DELTA: 00013
MAXIMA
1,51, 2
FILE: R01015 VELCL:+01.000
ANGLE: 15.012 DELTA: 00013
MAXIMA
1,51, 2
FILE: R01017 VELCL:+01.000
ANGLE: 15.012 DELTA: 00013
SCAN
PIXEL

Figure 28

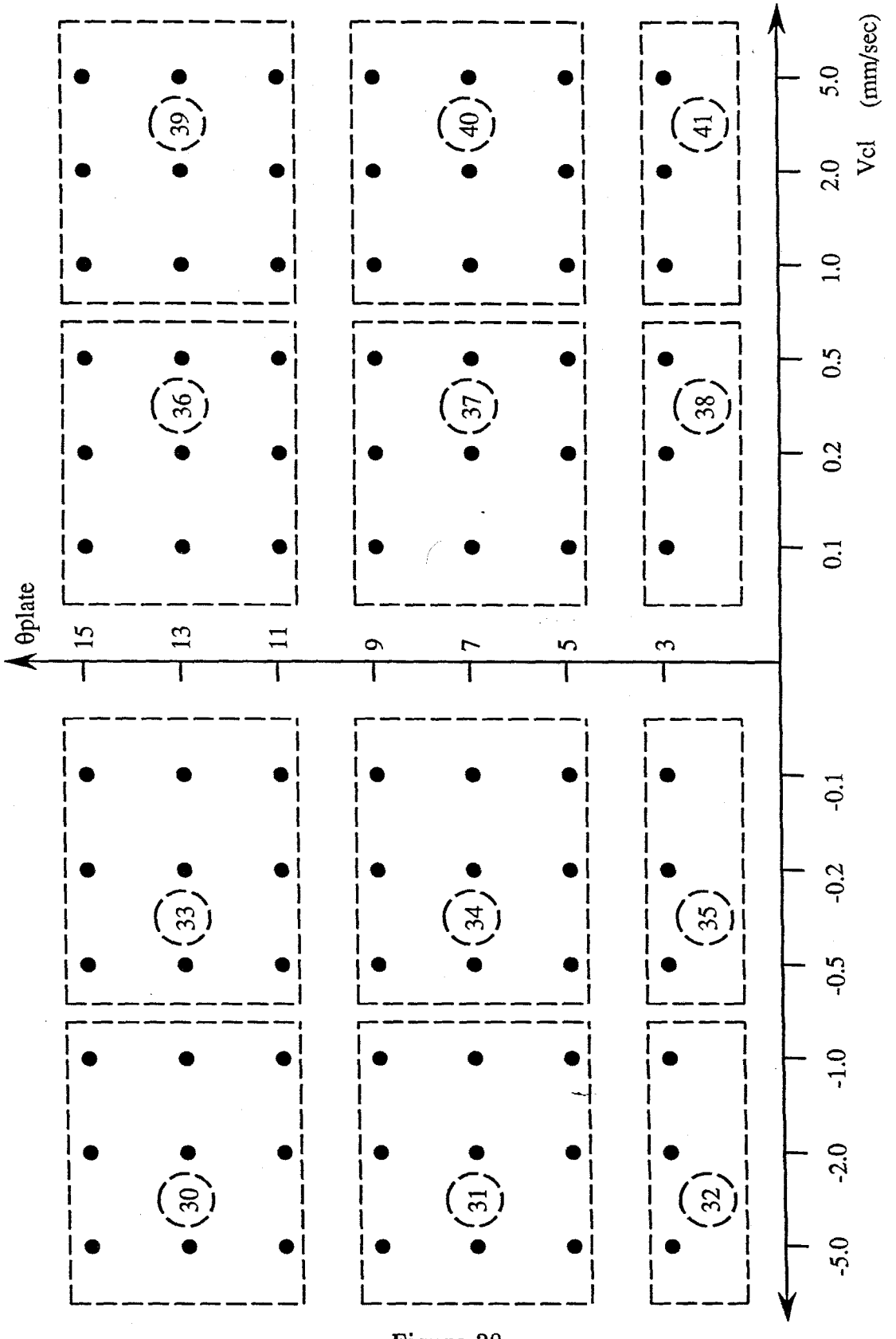

(Plate-angle, Velocity) space for "slippery"-plate experiments

Figure 29

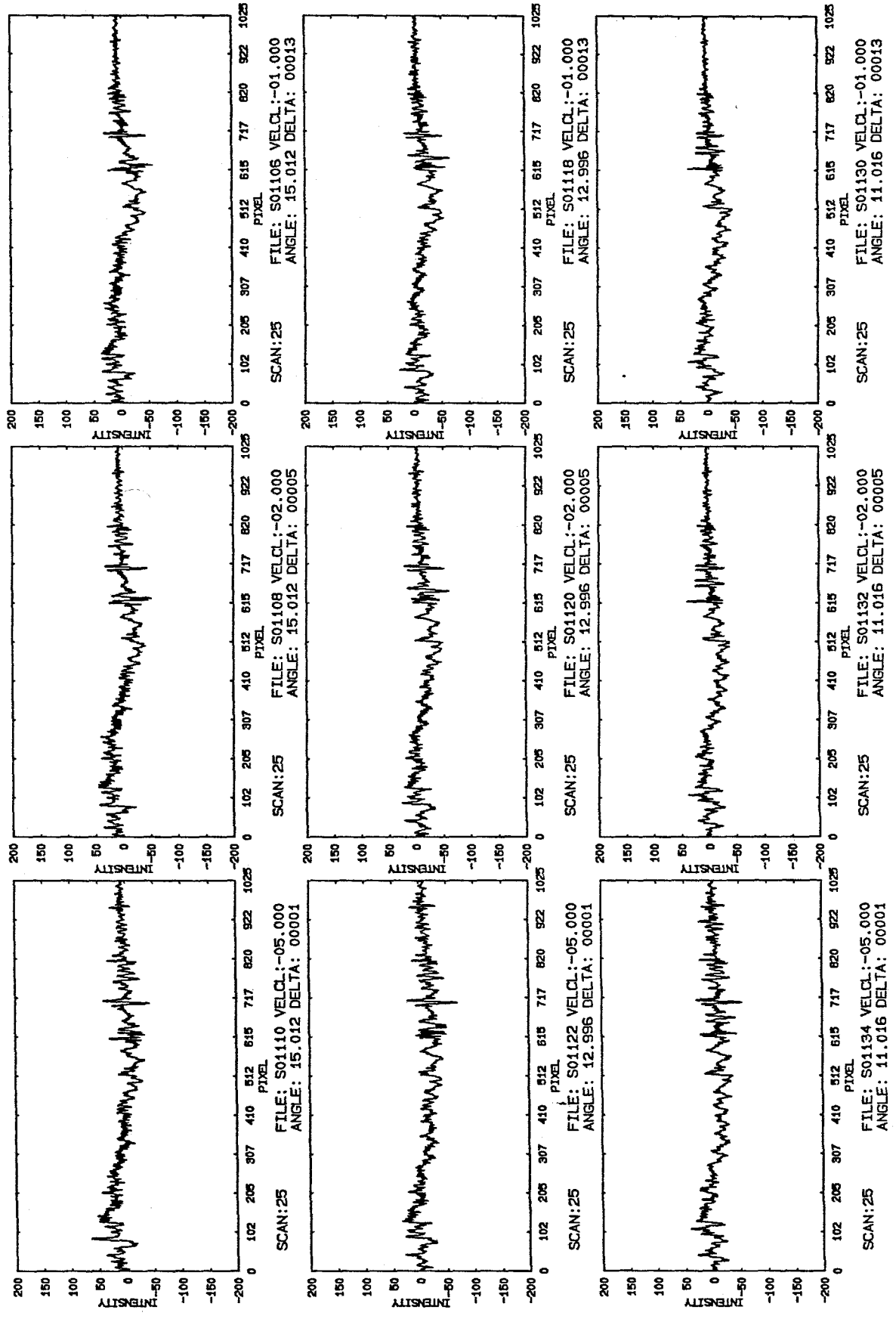
INTENSITY
PIXEL
SCAN:25
FILE: S01105 VELCL:-01.000
ANGLE: 15.012 DELTA: 00013
FILE: S01108 VELCL:-02.000
ANGLE: 15.012 DELTA: 00005
FILE: S01110 VELCL:-05.000
ANGLE: 15.012 DELTA: 00001
FILE: S01118 VELCL:-01.000
ANGLE: 12.996 DELTA: 00013
FILE: S01120 VELCL:-02.000
ANGLE: 12.996 DELTA: 00005
FILE: S01122 VELCL:-05.000
ANGLE: 12.996 DELTA: 00001
FILE: S01130 VELCL:-01.000
ANGLE: 11.016 DELTA: 00013
FILE: S01132 VELCL:-02.000
ANGLE: 11.016 DELTA: 00005
FILE: S01134 VELCL:-05.000
ANGLE: 11.016 DELTA: 00001

Figure 30

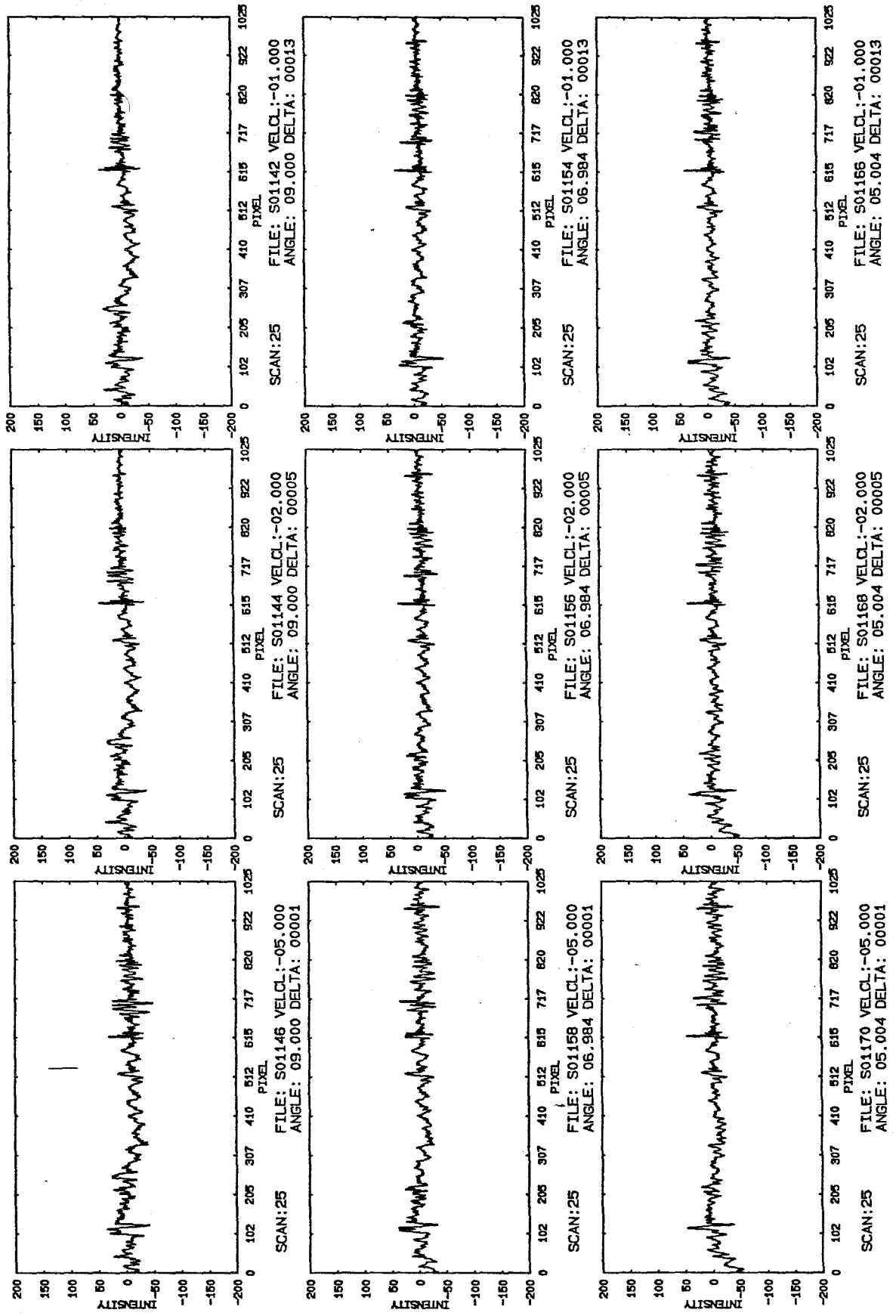
INTENSITY
PIXEL
SCAN:25
FILE: S01142 VELCL:-01.000
ANGLE: 09.000 DELTA: 00013
FILE: S01144 VELCL:-02.000
ANGLE: 09.000 DELTA: 00005
FILE: S01146 VELCL:-05.000
ANGLE: 09.000 DELTA: 00001
FILE: S01154 VELCL:-01.000
ANGLE: 06.984 DELTA: 00013
FILE: S01156 VELCL:-02.000
ANGLE: 06.984 DELTA: 00005
FILE: S01158 VELCL:-05.000
ANGLE: 06.984 DELTA: 00001
FILE: S01166 VELCL:-01.000
ANGLE: 05.004 DELTA: 00013
FILE: S01168 VELCL:-02.000
ANGLE: 05.004 DELTA: 00005
FILE: S01170 VELCL:-05.000
ANGLE: 05.004 DELTA: 00001

Figure 31

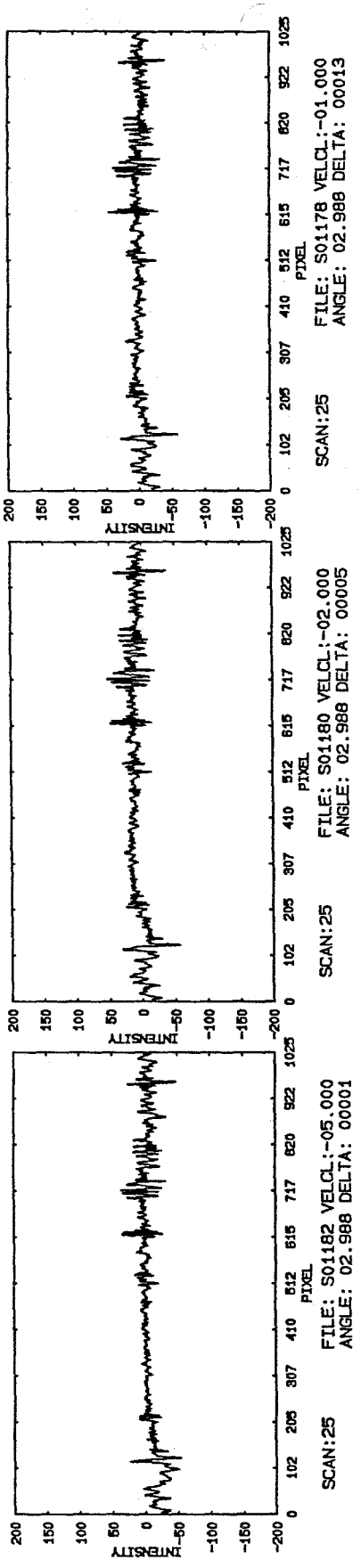
INTENSITY
PIXEL
SCAN:25
FILE: S01182 VELCL:-05.000
ANGLE: 02.988 DELTA: 00001
SCAN:25
FILE: S01180 VELCL:-02.000
ANGLE: 02.988 DELTA: 00005
SCAN:25
FILE: S01178 VELCL:-01.000
ANGLE: 02.988 DELTA: 00013

Figure 32

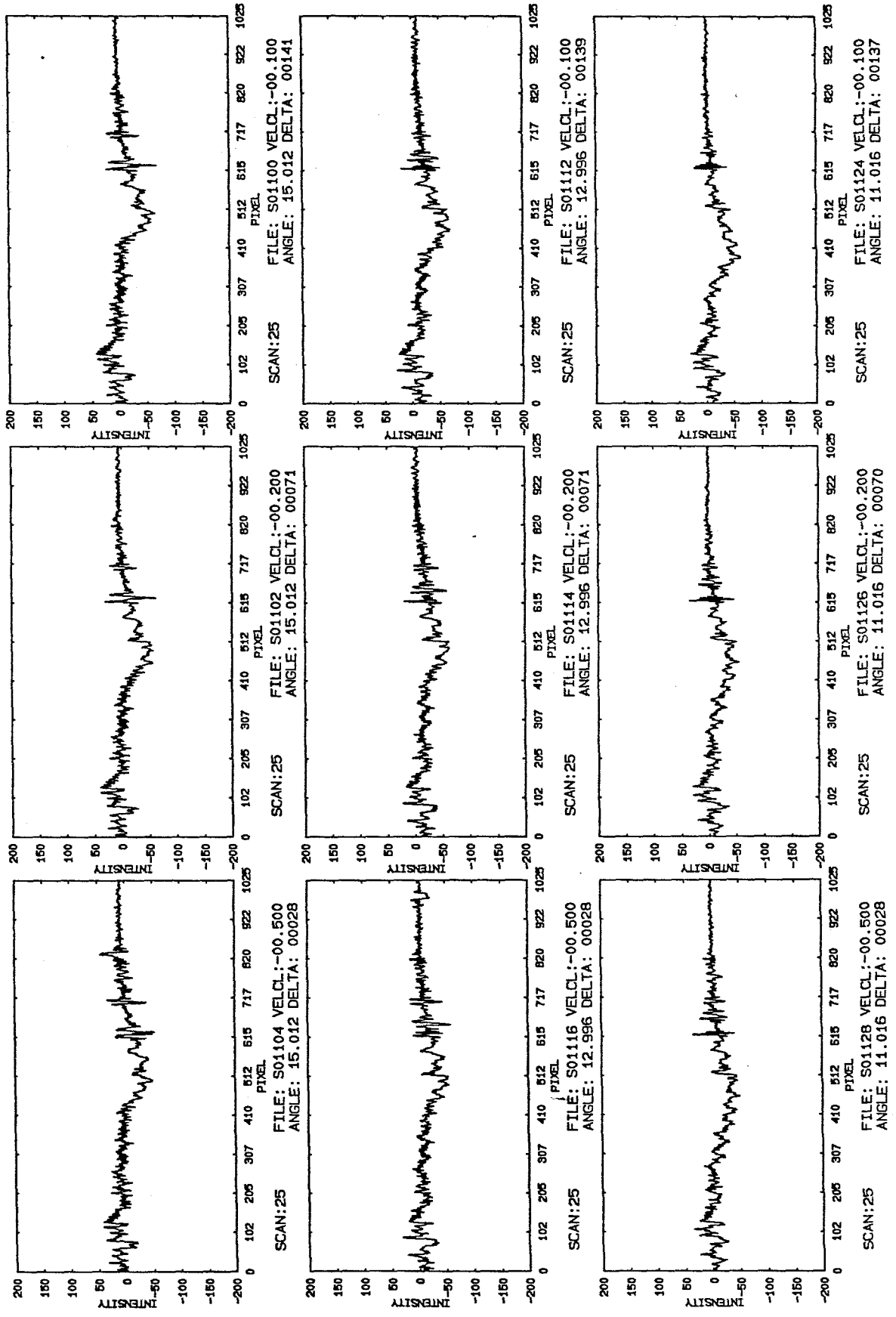
INTENSITY
PIXEL
SCAN:25
FILE: S01100 VELCL:-00.100
ANGLE: 15.012 DELTA: 00141
FILE: S01102 VELCL:-00.200
ANGLE: 15.012 DELTA: 00071
FILE: S01104 VELCL:-00.500
ANGLE: 15.012 DELTA: 00028
FILE: S01112 VELCL:-00.100
ANGLE: 12.996 DELTA: 00139
FILE: S01114 VELCL:-00.200
ANGLE: 12.996 DELTA: 00071
FILE: S01116 VELCL:-00.500
ANGLE: 12.996 DELTA: 00028
FILE: S01124 VELCL:-00.100
ANGLE: 11.016 DELTA: 00137
FILE: S01126 VELCL:-00.200
ANGLE: 11.016 DELTA: 00070
FILE: S01128 VELCL:-00.500
ANGLE: 11.016 DELTA: 00028

Figure 33

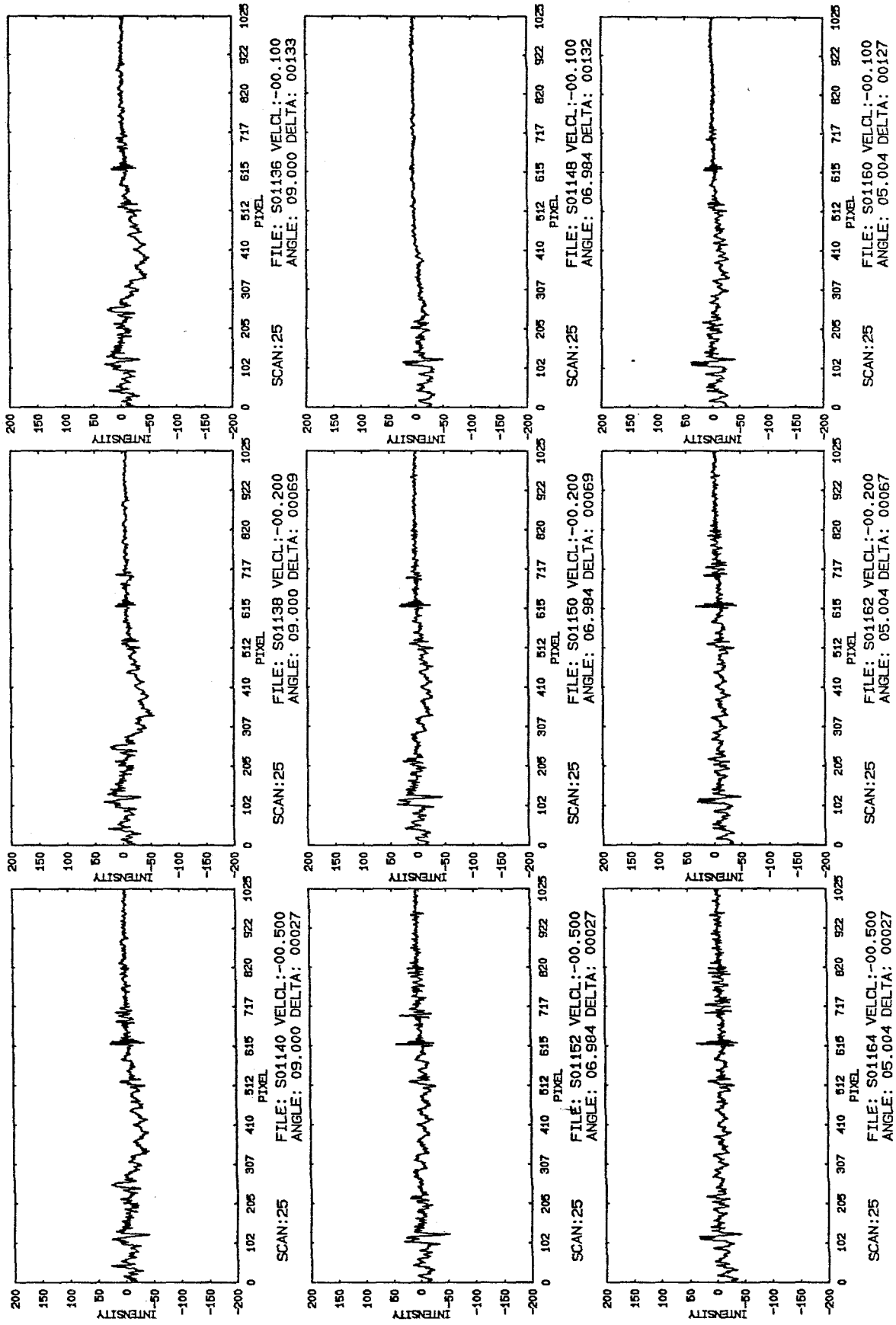
INTENSITY
PIXEL
SCAN:25
FILE: S01136 VELCL:-00.100
ANGLE: 09.000 DELTA: 00133
FILE: S01138 VELCL:-00.200
ANGLE: 09.000 DELTA: 00069
FILE: S01140 VELCL:-00.500
ANGLE: 09.000 DELTA: 00027
FILE: S01148 VELCL:-00.100
ANGLE: 06.984 DELTA: 00132
FILE: S01150 VELCL:-00.200
ANGLE: 06.984 DELTA: 00069
FILE: S01152 VELCL:-00.500
ANGLE: 06.984 DELTA: 00027
FILE: S01160 VELCL:-00.100
ANGLE: 05.004 DELTA: 00127
FILE: S01162 VELCL:-00.200
ANGLE: 05.004 DELTA: 00067
FILE: S01164 VELCL:-00.500
ANGLE: 05.004 DELTA: 00027

Figure 34

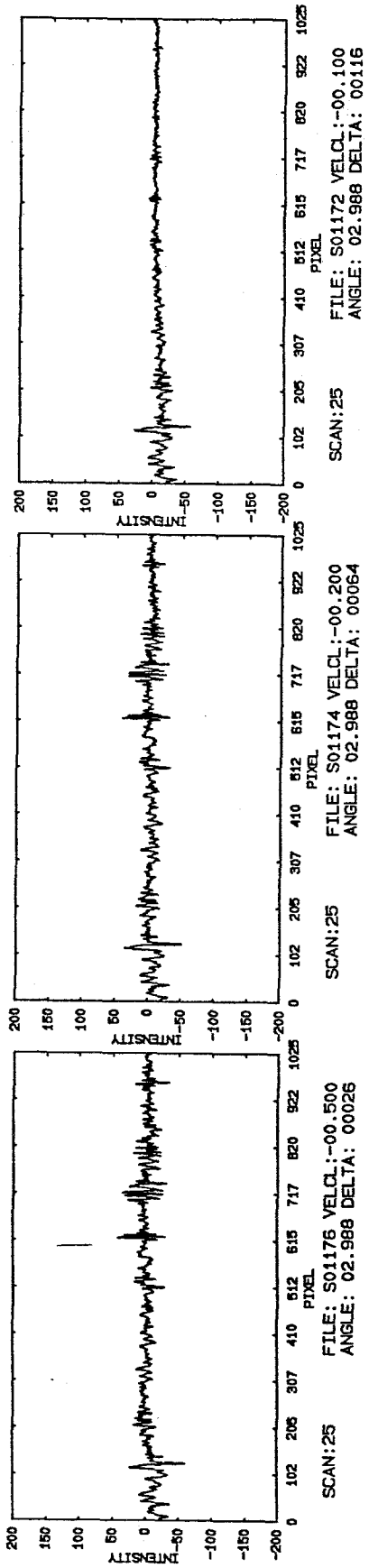
INTENSITY
PIXEL
SCAN:25
FILE: S01176 VELCL:-00.500
ANGLE: 02.988 DELTA: 00026
SCAN:25
FILE: S01174 VELCL:-00.200
ANGLE: 02.988 DELTA: 00064
SCAN:25
FILE: S01172 VELCL:-00.100
ANGLE: 02.988 DELTA: 00116

Figure 35

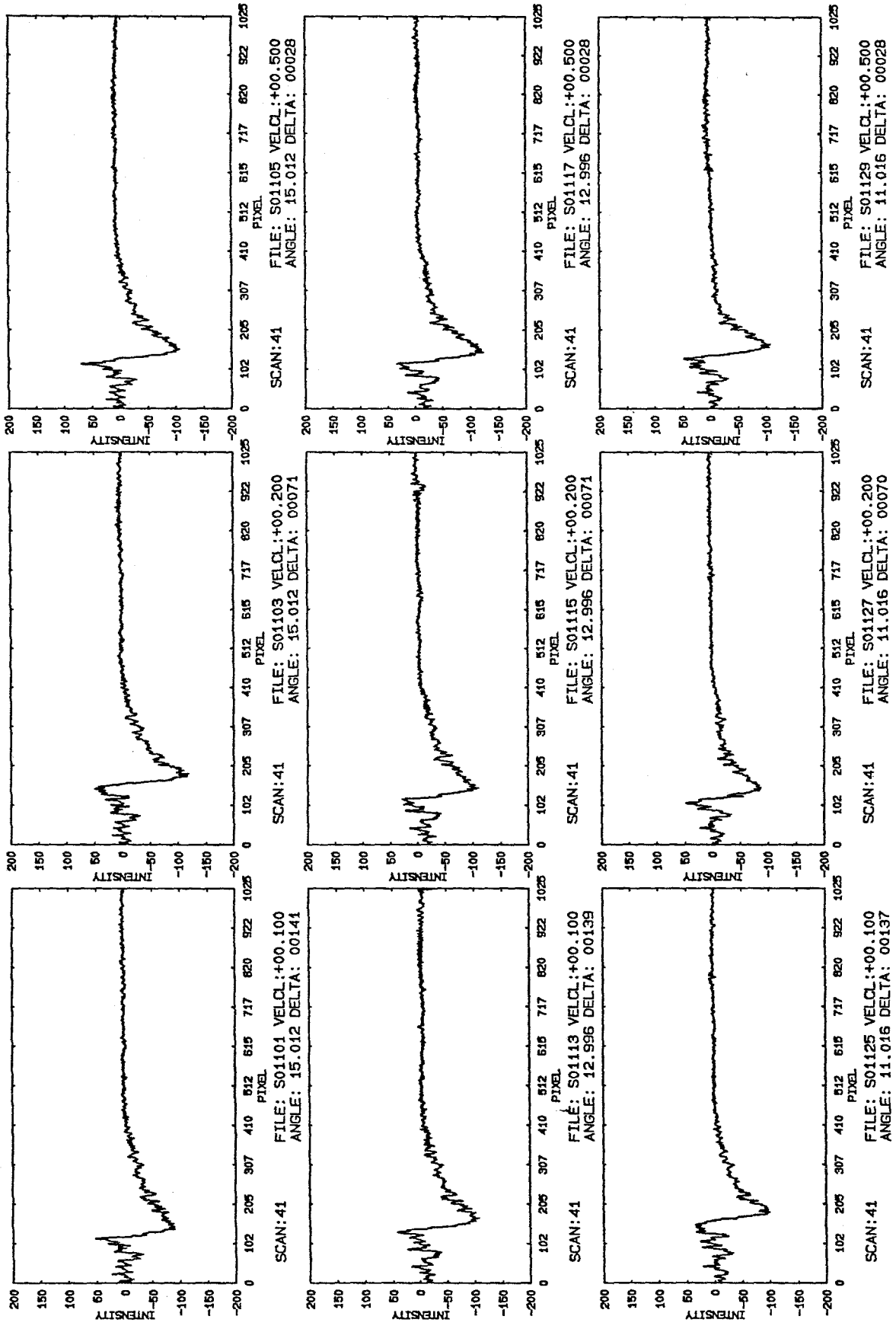
INTENSITY
PIXEL
SCAN:41
FILE: S01101 VELCL:+00.100
ANGLE: 15.012 DELTA: 00141
FILE: S01103 VELCL:+00.200
ANGLE: 15.012 DELTA: 00071
FILE: S01105 VELCL:+00.500
ANGLE: 15.012 DELTA: 00028
FILE: S01113 VELCL:+00.100
ANGLE: 12.996 DELTA: 00139
FILE: S01115 VELCL:+00.200
ANGLE: 12.996 DELTA: 00071
FILE: S01117 VELCL:+00.500
ANGLE: 12.996 DELTA: 00028
FILE: S01125 VELCL:+00.100
ANGLE: 11.016 DELTA: 00137
FILE: S01127 VELCL:+00.200
ANGLE: 11.016 DELTA: 00070
FILE: S01129 VELCL:+00.500
ANGLE: 11.016 DELTA: 00028

Figure 36

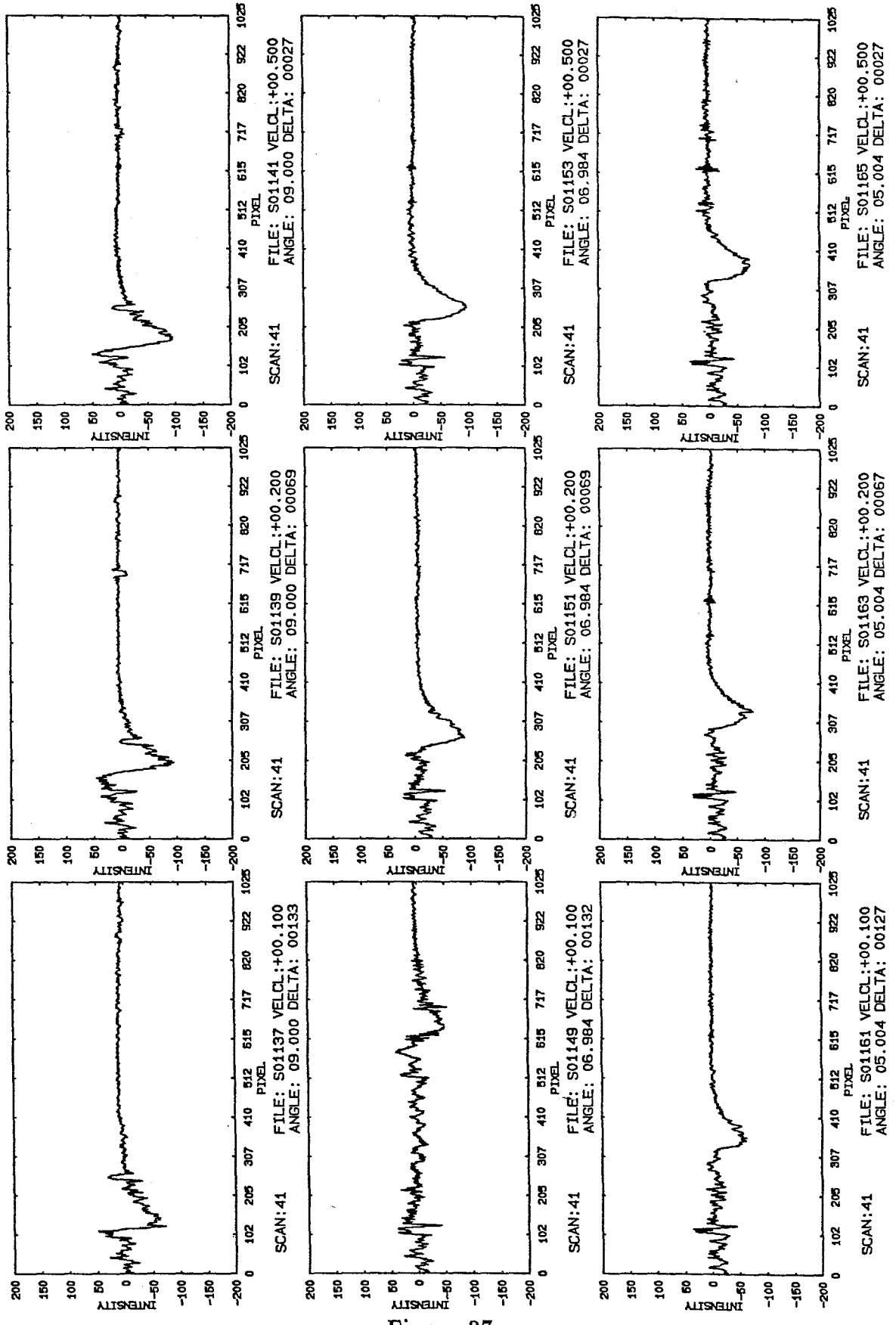
INTENSITY
PIXEL
SCAN:41
FILE: S01137 VELCL:+00.100
ANGLE: 09.000 DELTA: 00133
FILE: S01139 VELCL:+00.200
ANGLE: 09.000 DELTA: 00069
FILE: S01141 VELCL:+00.500
ANGLE: 09.000 DELTA: 00027
FILE: S01149 VELCL:+00.100
ANGLE: 06.984 DELTA: 00132
FILE: S01151 VELCL:+00.200
ANGLE: 06.984 DELTA: 00069
FILE: S01153 VELCL:+00.500
ANGLE: 06.984 DELTA: 00027
FILE: S01161 VELCL:+00.100
ANGLE: 05.004 DELTA: 00127
FILE: S01163 VELCL:+00.200
ANGLE: 05.004 DELTA: 00067
FILE: S01165 VELCL:+00.500
ANGLE: 05.004 DELTA: 00027

Figure 37

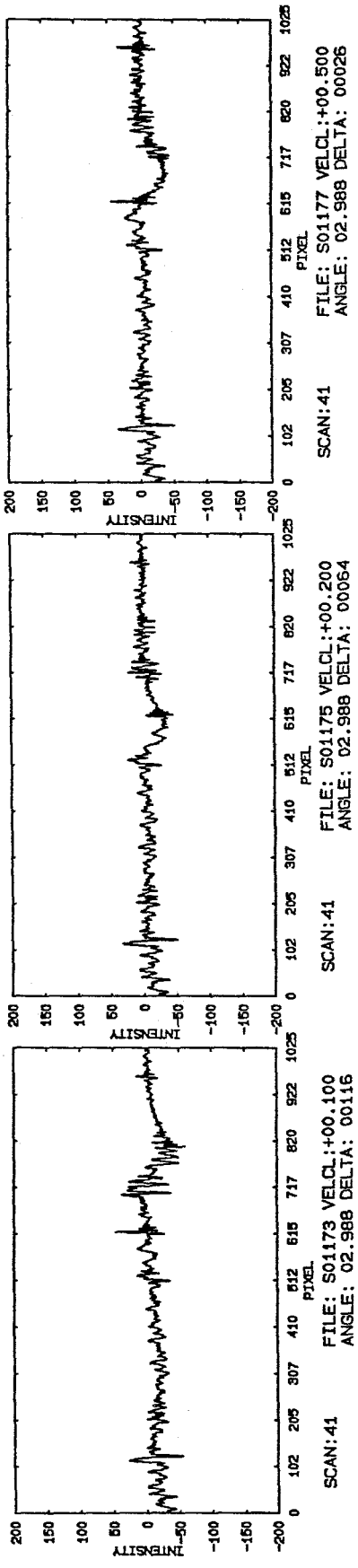
INTENSITY
PIXEL
SCAN:41
FILE: S01173 VELCL:+00.100
ANGLE: 02.988 DELTA: 00116
FILE: S01175 VELCL:+00.200
ANGLE: 02.988 DELTA: 00064
FILE: S01177 VELCL:+00.500
ANGLE: 02.988 DELTA: 00026

Figure 38

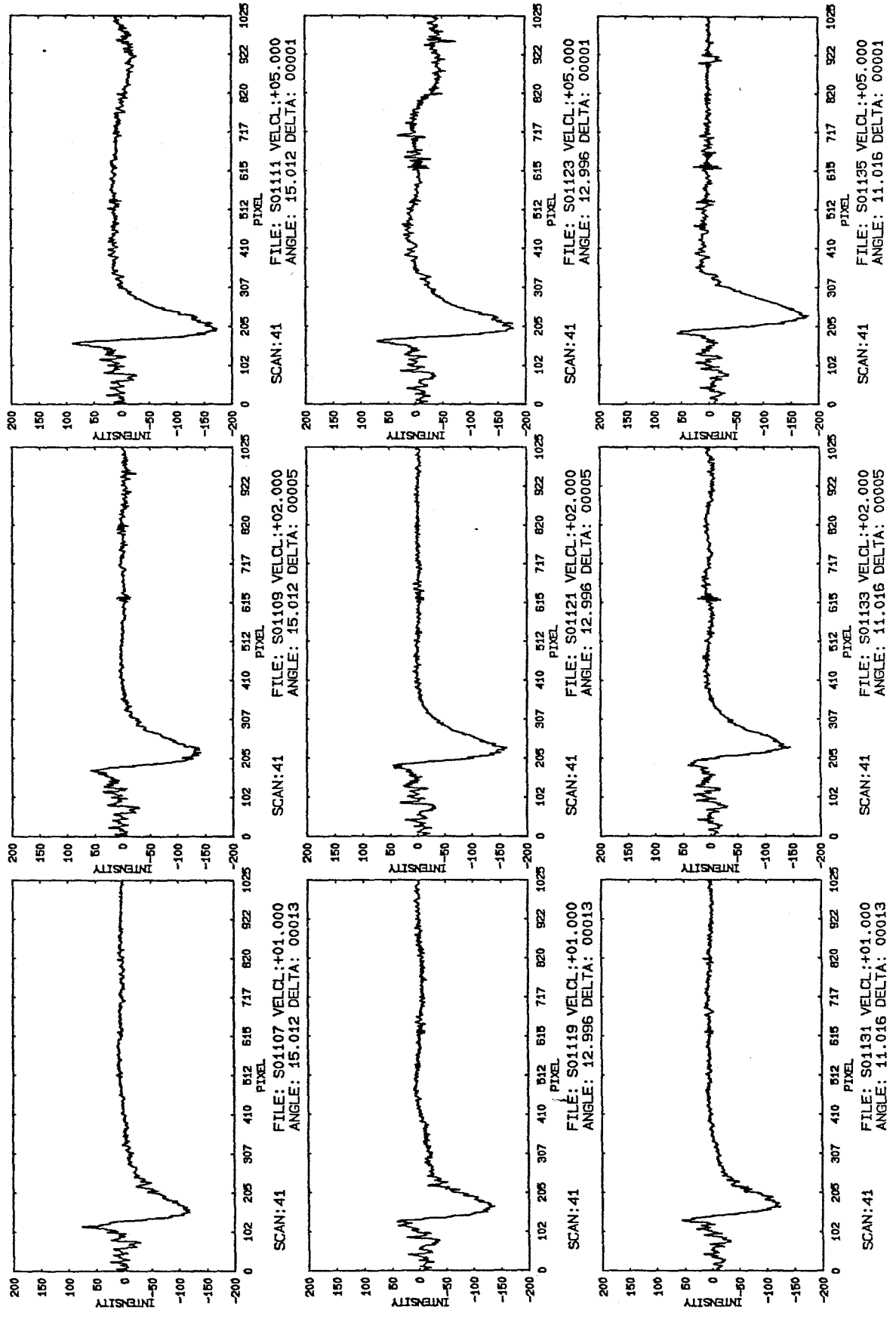
INTENSITY
PIXEL
SCAN:41
FILE: S01107 VELCL:+01.000
ANGLE: 15.012 DELTA: 00013
FILE: S01109 VELCL:+02.000
ANGLE: 15.012 DELTA: 00005
FILE: S01111 VELCL:+05.000
ANGLE: 15.012 DELTA: 00001
FILE: S01119 VELCL:+01.000
ANGLE: 12.996 DELTA: 00013
FILE: S01121 VELCL:+02.000
ANGLE: 12.996 DELTA: 00005
FILE: S01123 VELCL:+05.000
ANGLE: 12.996 DELTA: 00001
FILE: S01131 VELCL:+01.000
ANGLE: 11.016 DELTA: 00013
FILE: S01133 VELCL:+02.000
ANGLE: 11.016 DELTA: 00005
FILE: S01135 VELCL:+05.000
ANGLE: 11.016 DELTA: 00001

Figure 39

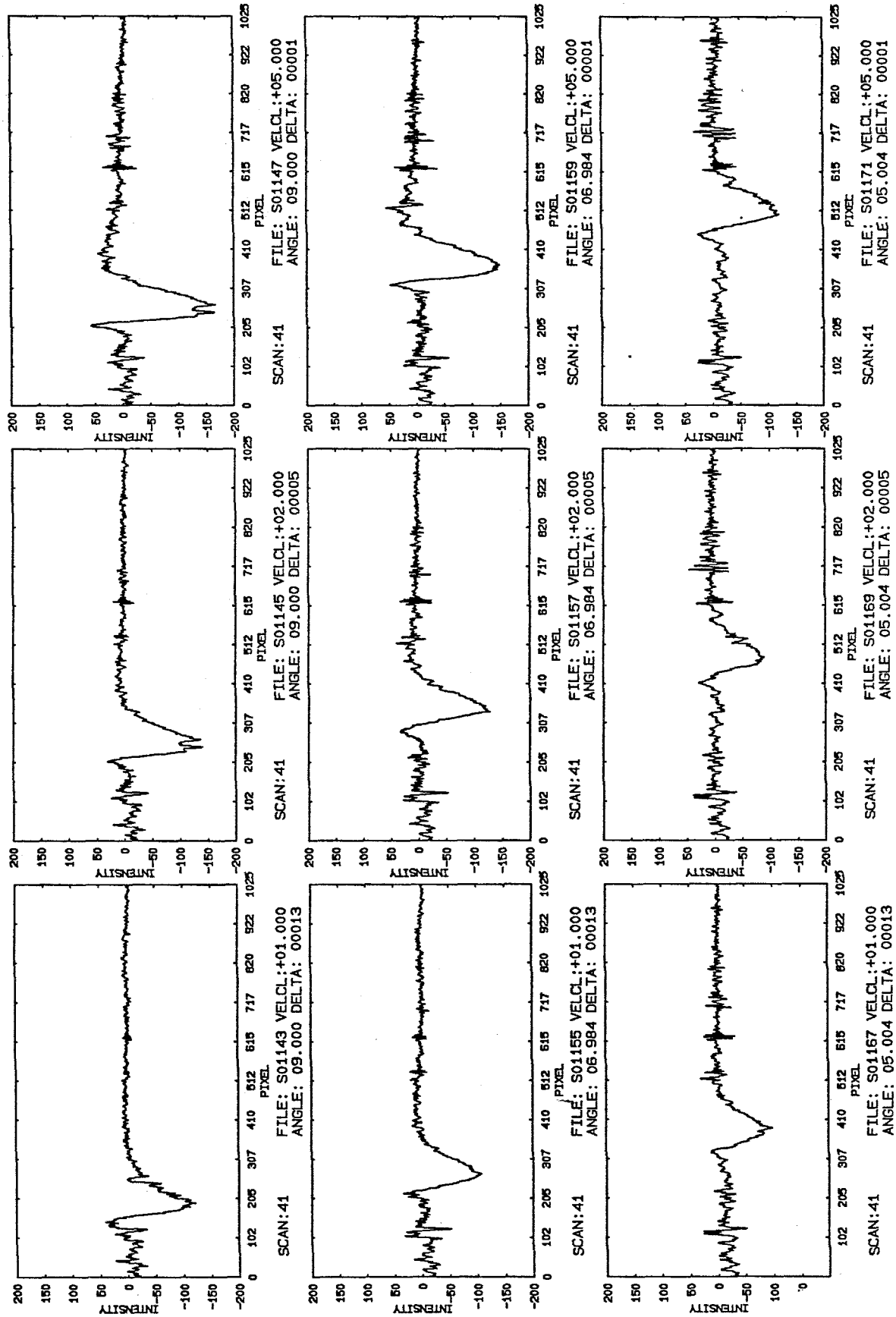
INTENSITY
PIXEL
SCAN:41
FILE: S01143 VELCL:+01.000
ANGLE: 09.000 DELTA: 00013
FILE: S01145 VELCL:+02.000
ANGLE: 09.000 DELTA: 00005
FILE: S01147 VELCL:+05.000
ANGLE: 09.000 DELTA: 00001
FILE: S01155 VELCL:+01.000
ANGLE: 06.984 DELTA: 00013
FILE: S01157 VELCL:+02.000
ANGLE: 06.984 DELTA: 00005
FILE: S01159 VELCL:+05.000
ANGLE: 06.984 DELTA: 00001
FILE: S01167 VELCL:+01.000
ANGLE: 05.004 DELTA: 00013
FILE: S01169 VELCL:+02.000
ANGLE: 05.004 DELTA: 00005
FILE: S01171 VELCL:+05.000
ANGLE: 05.004 DELTA: 00001

Figure 40

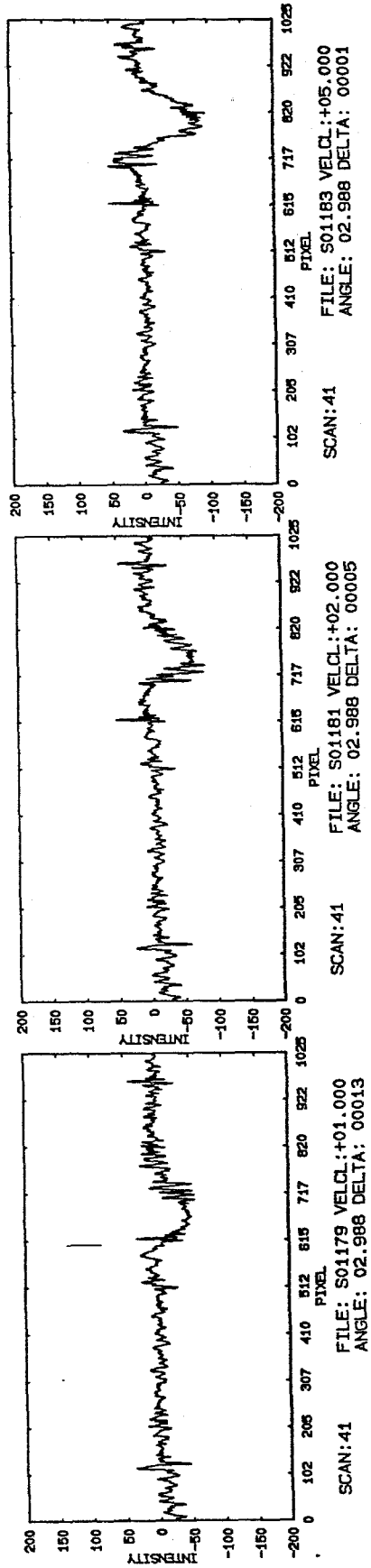
INTENSITY
PIXEL
SCAN:41
FILE: S01179 VELCL:+01.000
ANGLE: 02.988 DELTA: 00013
FILE: S01181 VELCL:+02.000
ANGLE: 02.988 DELTA: 00005
FILE: S01183 VELCL:+05.000
ANGLE: 02.988 DELTA: 00001

Figure 41

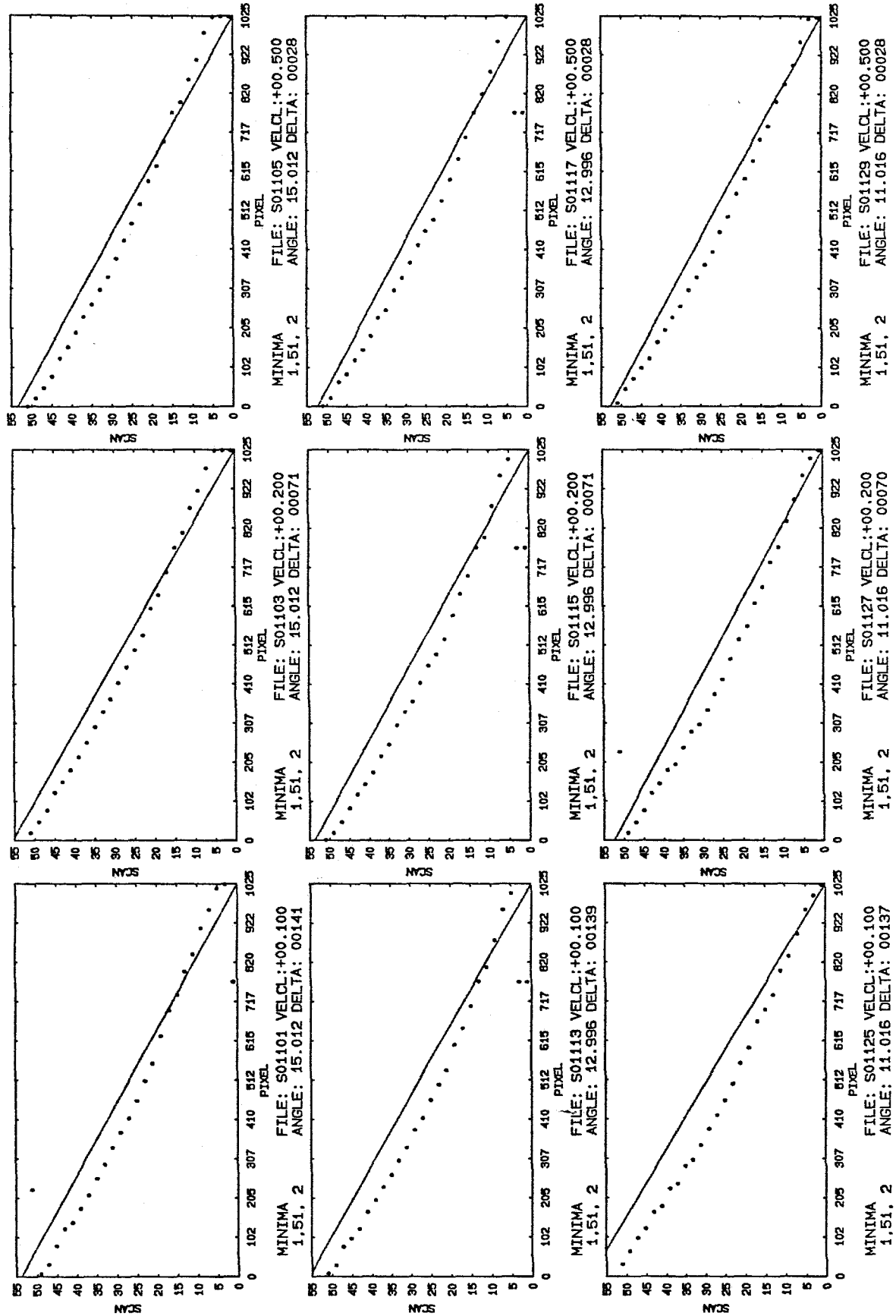
SCAN
PIXEL
MINIMA
1,51, 2
FILE: S01101 VELCL:+00.100
ANGLE: 15.012 DELTA: 00141
FILE: S01103 VELCL:+00.200
ANGLE: 15.012 DELTA: 00071
FILE: S01105 VELCL:+00.500
ANGLE: 15.012 DELTA: 00028
FILE: S01113 VELCL:+00.100
ANGLE: 12.996 DELTA: 00139
FILE: S01115 VELCL:+00.200
ANGLE: 12.996 DELTA: 00071
FILE: S01117 VELCL:+00.500
ANGLE: 12.996 DELTA: 00028
FILE: S01125 VELCL:+00.100
ANGLE: 11.016 DELTA: 00137
FILE: S01127 VELCL:+00.200
ANGLE: 11.016 DELTA: 00070
FILE: S01129 VELCL:+00.500
ANGLE: 11.016 DELTA: 00028

Figure 42

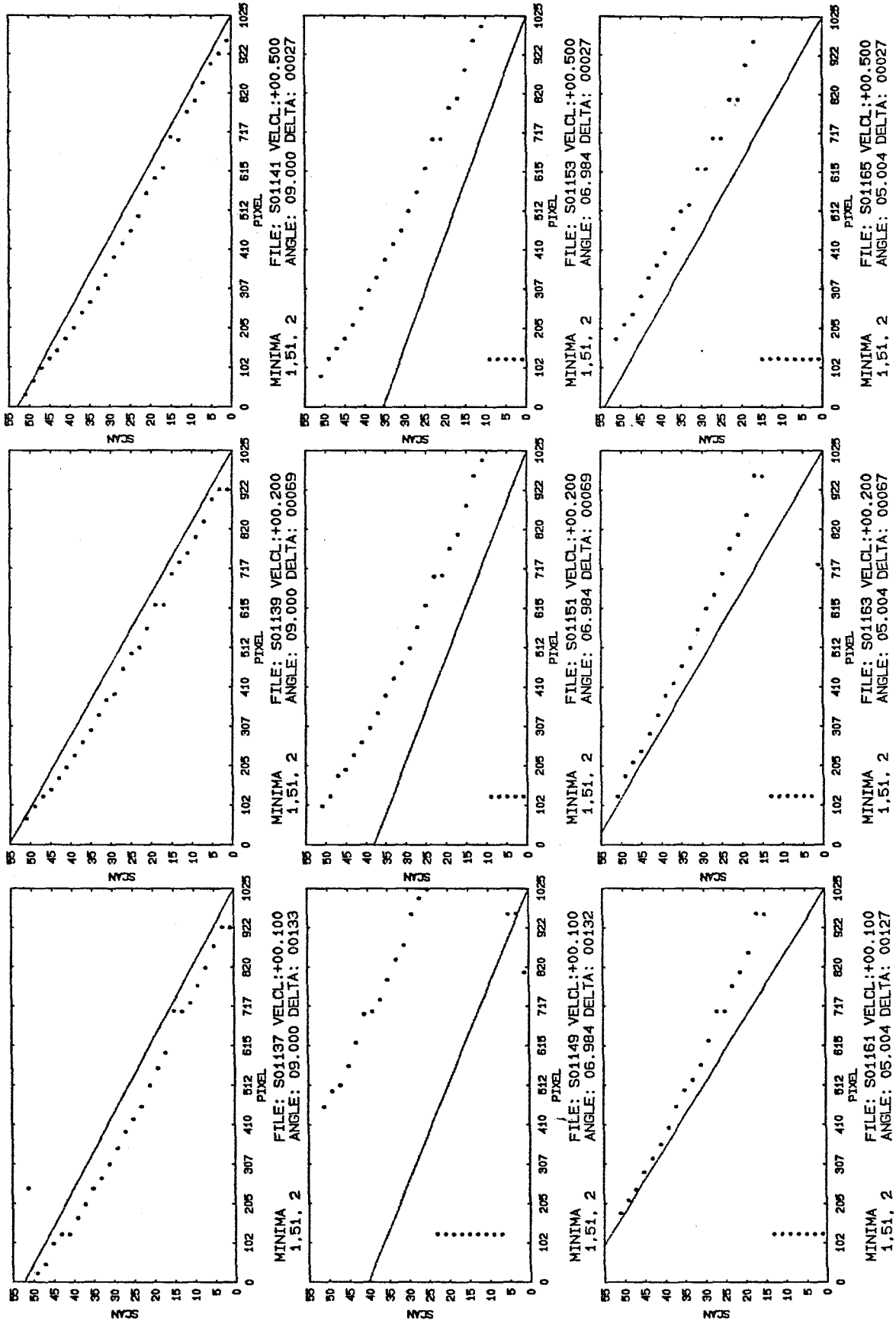
FILE: S01137 VELCL:+00.100
ANGLE: 09.000 DELTA: 00133
MINIMA
1,51, 2
FILE: S01139 VELCL:+00.200
ANGLE: 09.000 DELTA: 00069
MINIMA
1,51, 2
FILE: S01141 VELCL:+00.500
ANGLE: 09.000 DELTA: 00027
MINIMA
1,51, 2
FILE: S01149 VELCL:+00.100
ANGLE: 06.984 DELTA: 00132
MINIMA
1,51, 2
FILE: S01151 VELCL:+00.200
ANGLE: 06.984 DELTA: 00069
MINIMA
1,51, 2
FILE: S01153 VELCL:+00.500
ANGLE: 06.984 DELTA: 00027
MINIMA
1,51, 2
FILE: S01161 VELCL:+00.100
ANGLE: 05.004 DELTA: 00127
MINIMA
1,51, 2
FILE: S01163 VELCL:+00.200
ANGLE: 05.004 DELTA: 00067
MINIMA
1,51, 2
FILE: S01165 VELCL:+00.500
ANGLE: 05.004 DELTA: 00027
MINIMA
1,51, 2
SCAN
PIXEL

Figure 43

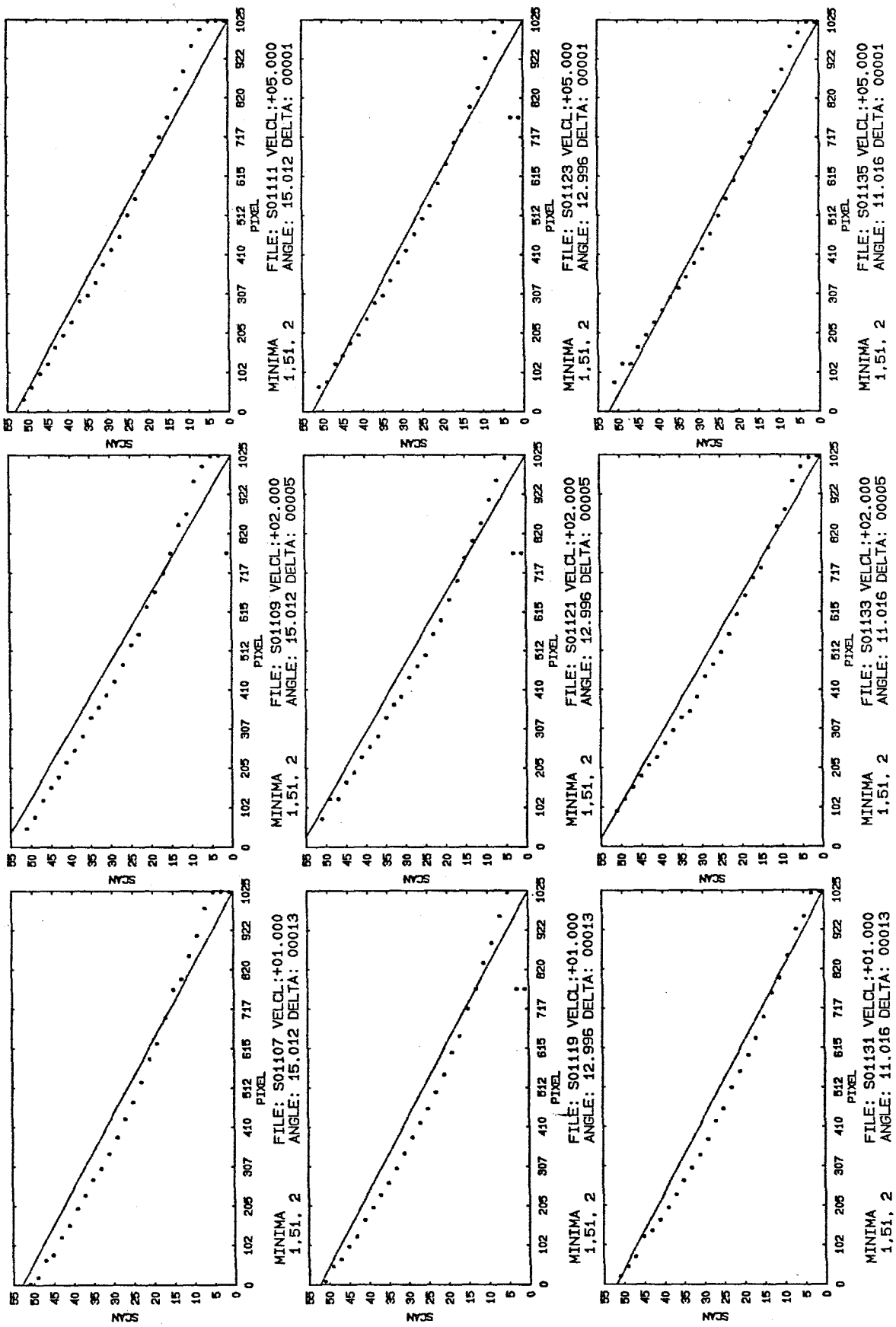
SCAN
PIXEL
MINIMA
1,51, 2
FILE: S01107 VELCL:+01.000
ANGLE: 15.012 DELTA: 00013
FILE: S01109 VELCL:+02.000
ANGLE: 15.012 DELTA: 00005
FILE: S01111 VELCL:+05.000
ANGLE: 15.012 DELTA: 00001
FILE: S01119 VELCL:+01.000
ANGLE: 12.996 DELTA: 00013
FILE: S01121 VELCL:+02.000
ANGLE: 12.996 DELTA: 00005
FILE: S01123 VELCL:+05.000
ANGLE: 12.996 DELTA: 00001
FILE: S01131 VELCL:+01.000
ANGLE: 11.016 DELTA: 00013
FILE: S01133 VELCL:+02.000
ANGLE: 11.016 DELTA: 00005
FILE: S01135 VELCL:+05.000
ANGLE: 11.016 DELTA: 00001

Figure 44

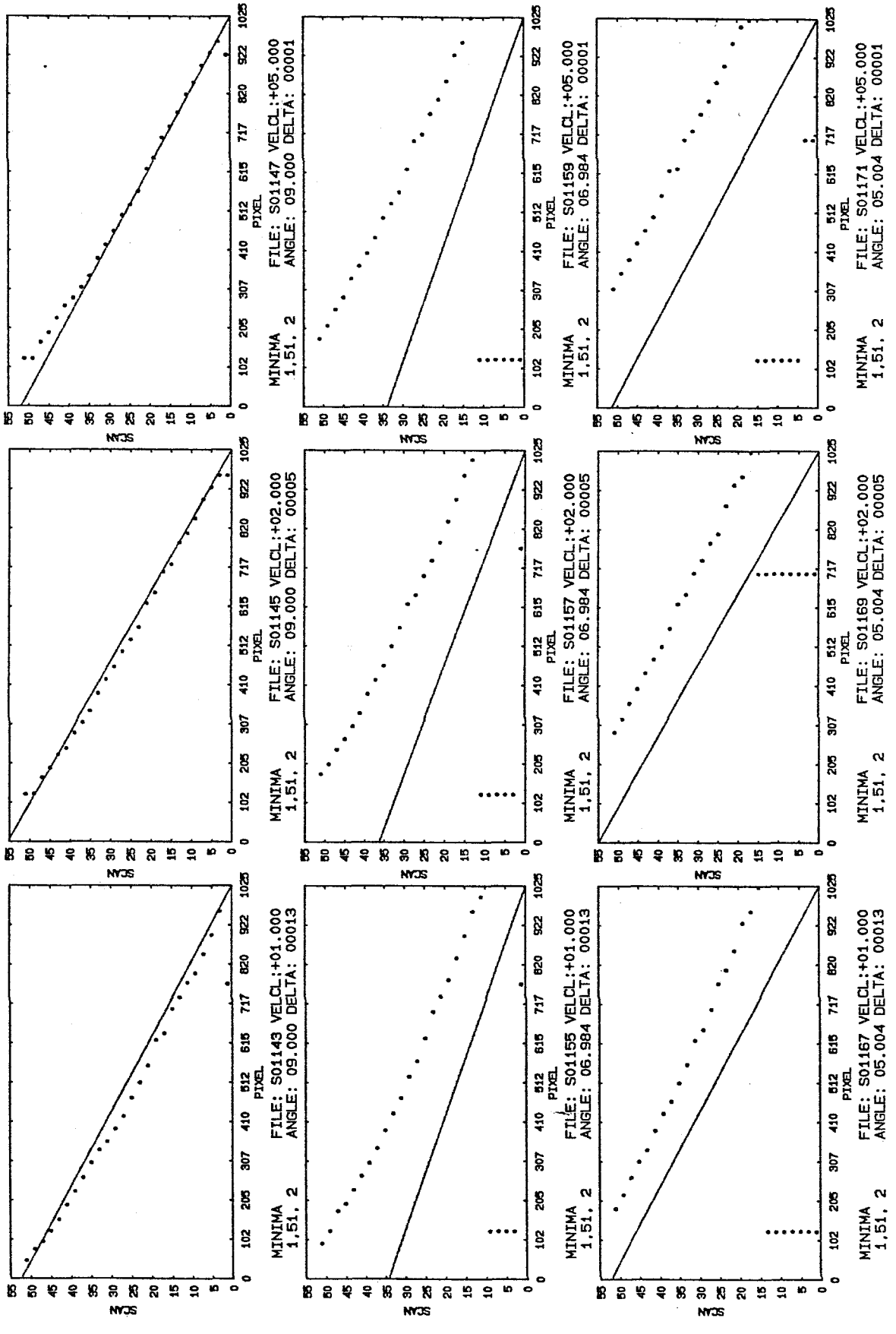
SCAN
PIXEL
MINIMA
1,51, 2
FILE: S01143 VELCL:+01.000
ANGLE: 09.000 DELTA: 00013
FILE: S01145 VELCL:+02.000
ANGLE: 09.000 DELTA: 00005
FILE: S01147 VELCL:+05.000
ANGLE: 09.000 DELTA: 00001
FILE: S01155 VELCL:+01.000
ANGLE: 06.984 DELTA: 00013
FILE: S01157 VELCL:+02.000
ANGLE: 06.984 DELTA: 00005
FILE: S01159 VELCL:+05.000
ANGLE: 06.984 DELTA: 00001
FILE: S01167 VELCL:+01.000
ANGLE: 05.004 DELTA: 00013
FILE: S01169 VELCL:+02.000
ANGLE: 05.004 DELTA: 00005
FILE: S01171 VELCL:+05.000
ANGLE: 05.004 DELTA: 00001

Figure 45

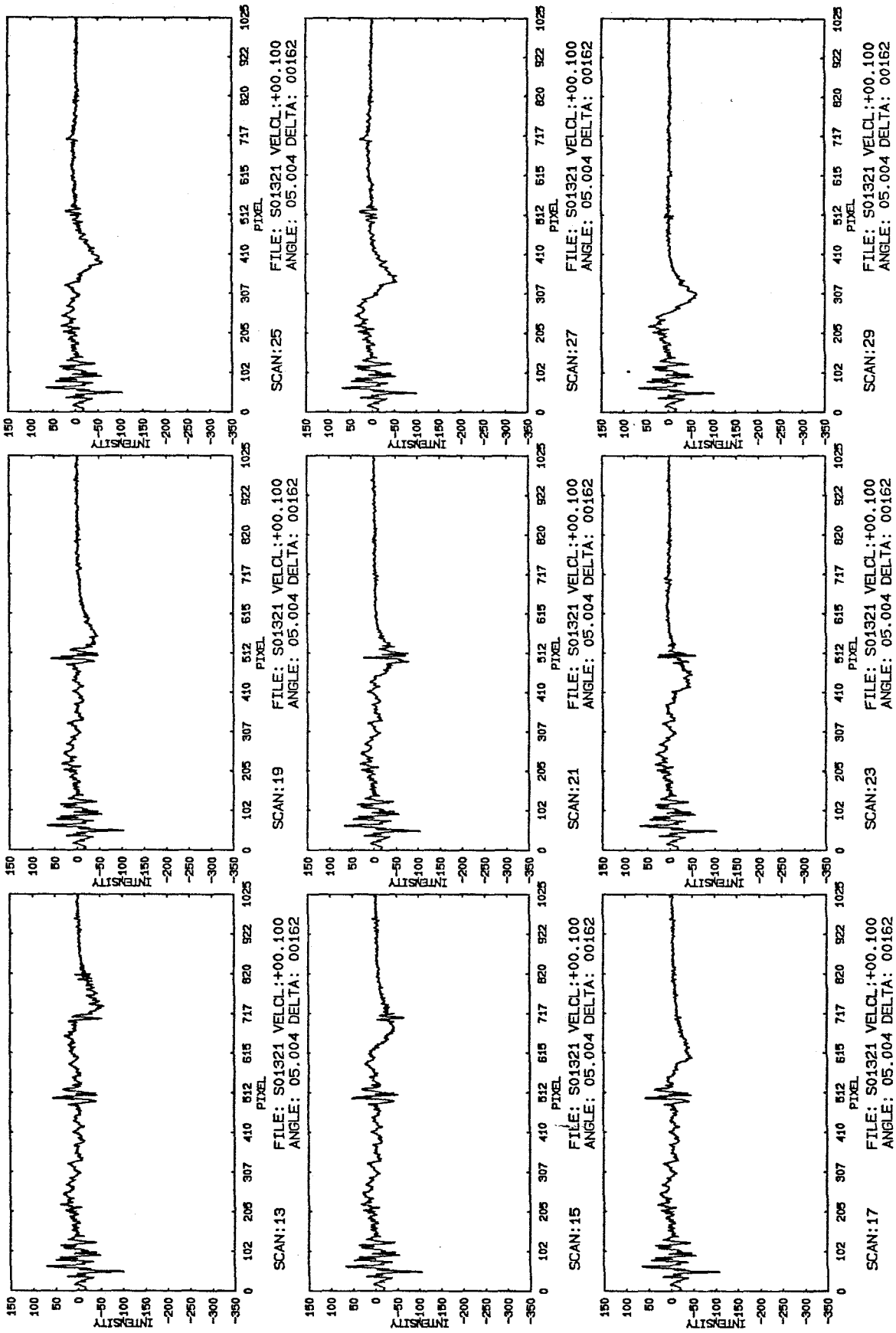
SCAN:13
FILE: S01321 VELCL:+00.100
ANGLE: 05.004 DELTA: 00162
SCAN:15
FILE: S01321 VELCL:+00.100
ANGLE: 05.004 DELTA: 00162
SCAN:17
FILE: S01321 VELCL:+00.100
ANGLE: 05.004 DELTA: 00162
SCAN:19
FILE: S01321 VELCL:+00.100
ANGLE: 05.004 DELTA: 00162
SCAN:21
FILE: S01321 VELCL:+00.100
ANGLE: 05.004 DELTA: 00162
SCAN:23
FILE: S01321 VELCL:+00.100
ANGLE: 05.004 DELTA: 00162
SCAN:25
FILE: S01321 VELCL:+00.100
ANGLE: 05.004 DELTA: 00162
SCAN:27
FILE: S01321 VELCL:+00.100
ANGLE: 05.004 DELTA: 00162
SCAN:29
FILE: S01321 VELCL:+00.100
ANGLE: 05.004 DELTA: 00162
INTENSITY
PIXEL

Figure 46

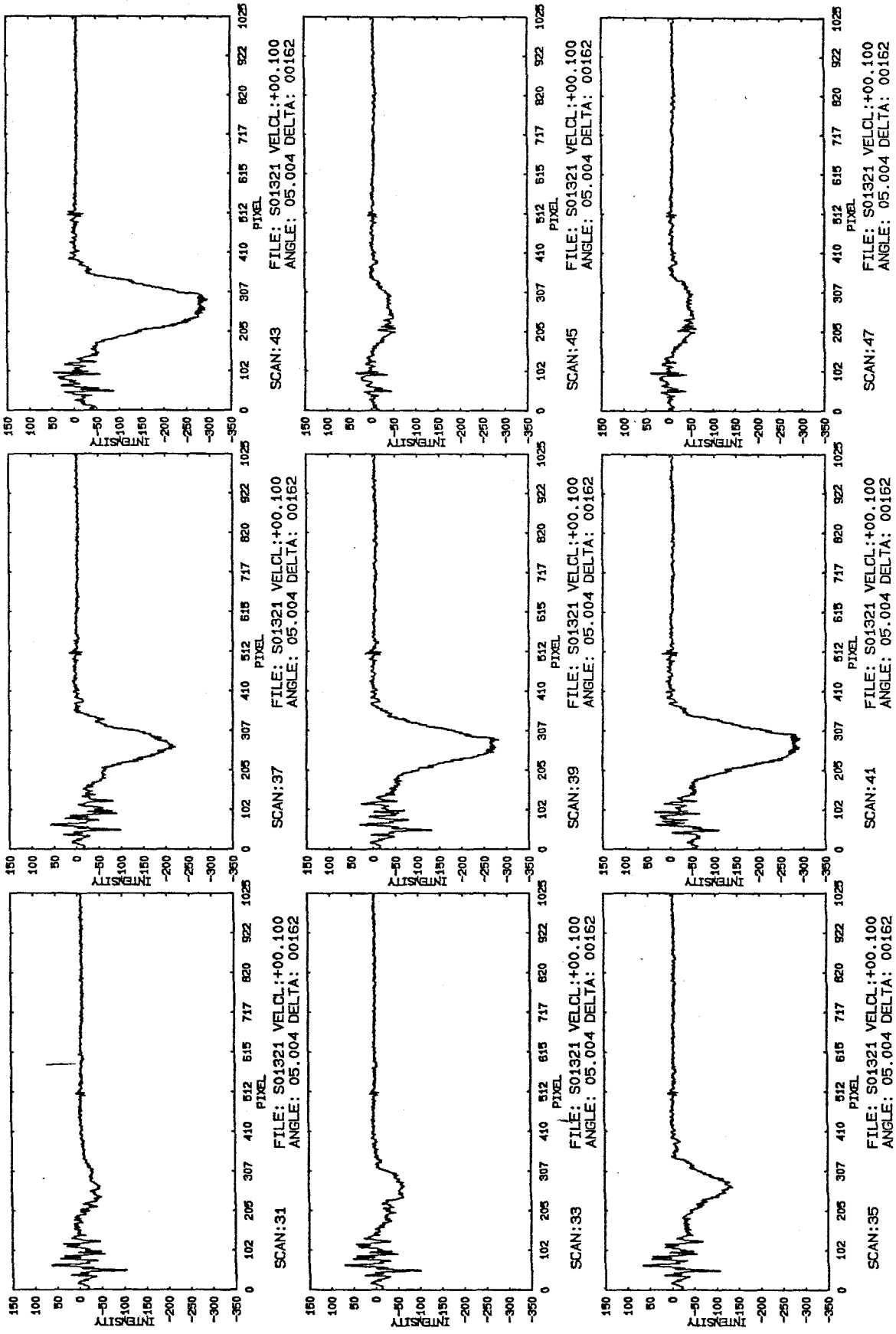
INTENSITY
PIXEL
SCAN:31
FILE: S01321 VELCL:+00.100
ANGLE: 05.004 DELTA: 00162
SCAN:33
FILE: S01321 VELCL:+00.100
ANGLE: 05.004 DELTA: 00162
SCAN:35
FILE: S01321 VELCL:+00.100
ANGLE: 05.004 DELTA: 00162
SCAN:37
FILE: S01321 VELCL:+00.100
ANGLE: 05.004 DELTA: 00162
SCAN:39
FILE: S01321 VELCL:+00.100
ANGLE: 05.004 DELTA: 00162
SCAN:41
FILE: S01321 VELCL:+00.100
ANGLE: 05.004 DELTA: 00162
SCAN:43
FILE: S01321 VELCL:+00.100
ANGLE: 05.004 DELTA: 00162
SCAN:45
FILE: S01321 VELCL:+00.100
ANGLE: 05.004 DELTA: 00162
SCAN:47
FILE: S01321 VELCL:+00.100
ANGLE: 05.004 DELTA: 00162

Figure 47

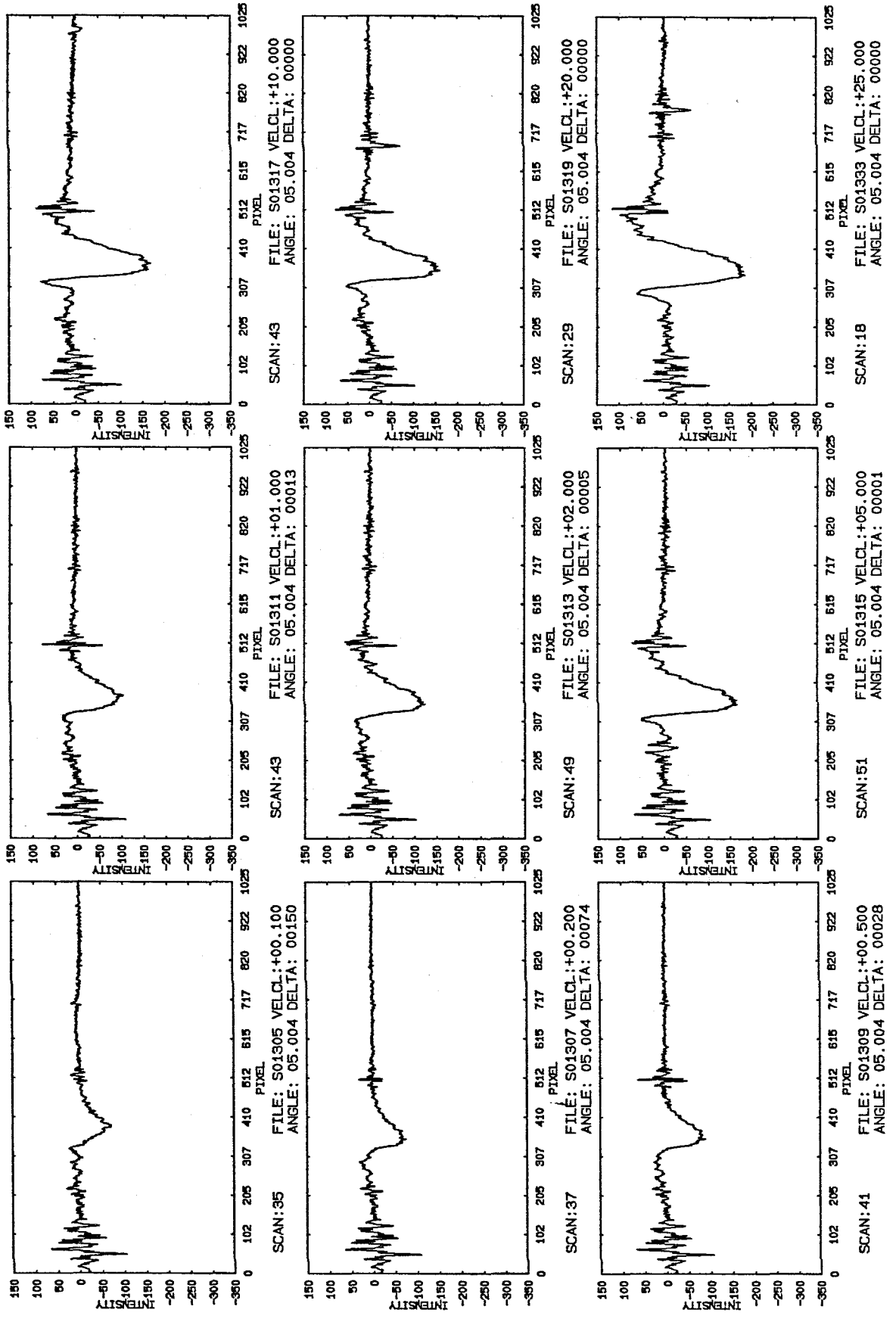
INTENSITY
PIXEL
SCAN:35
FILE: S01305 VELCL:+00.100
ANGLE: 05.004 DELTA: 00150
SCAN:37
FILE: S01307 VELCL:+00.200
ANGLE: 05.004 DELTA: 00074
SCAN:41
FILE: S01309 VELCL:+00.500
ANGLE: 05.004 DELTA: 00028
SCAN:43
FILE: S01311 VELCL:+01.000
ANGLE: 05.004 DELTA: 00013
SCAN:49
FILE: S01313 VELCL:+02.000
ANGLE: 05.004 DELTA: 00005
SCAN:51
FILE: S01315 VELCL:+05.000
ANGLE: 05.004 DELTA: 00001
SCAN:43
FILE: S01317 VELCL:+10.000
ANGLE: 05.004 DELTA: 00000
SCAN:29
FILE: S01319 VELCL:+20.000
ANGLE: 05.004 DELTA: 00000
SCAN:18
FILE: S01333 VELCL:+25.000
ANGLE: 05.004 DELTA: 00000

Figure 48

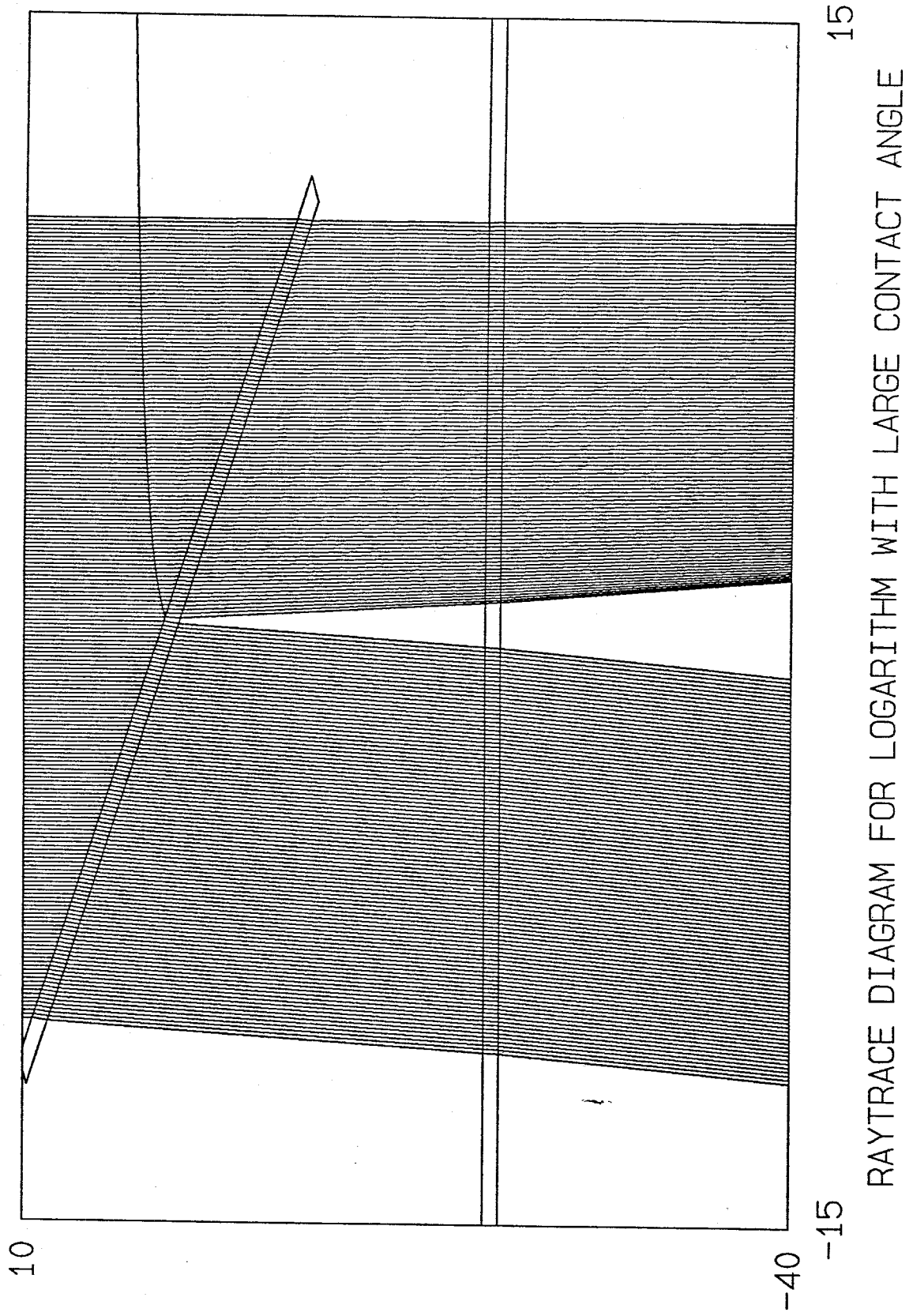
RAYTRACE DIAGRAM FOR LOGARITHM WITH LARGE CONTACT ANGLE
15
-15
10
-40

Figure 49

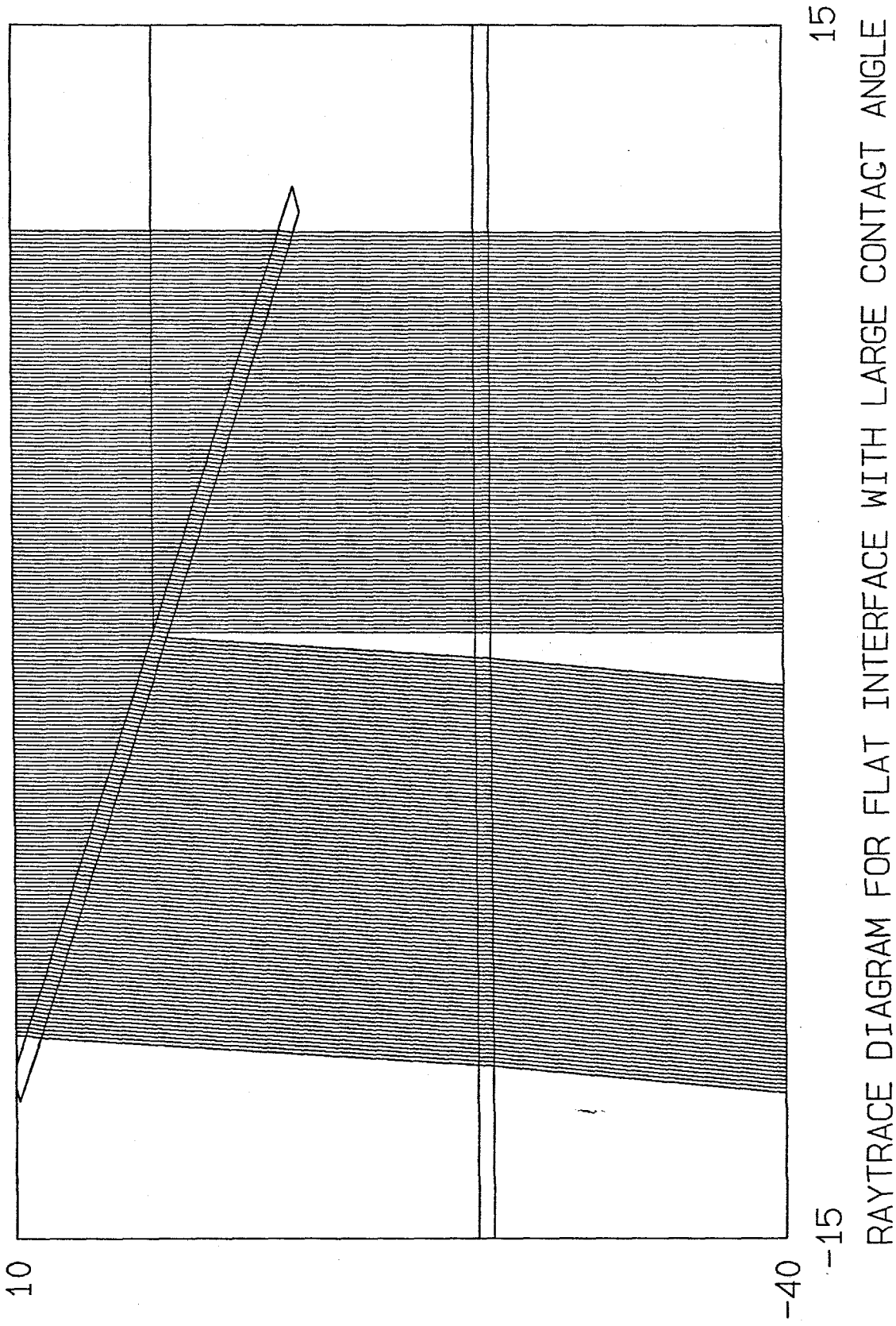
RAYTRACE DIAGRAM FOR FLAT INTERFACE WITH LARGE CONTACT ANGLE
15
-15
10
-40

Figure 50

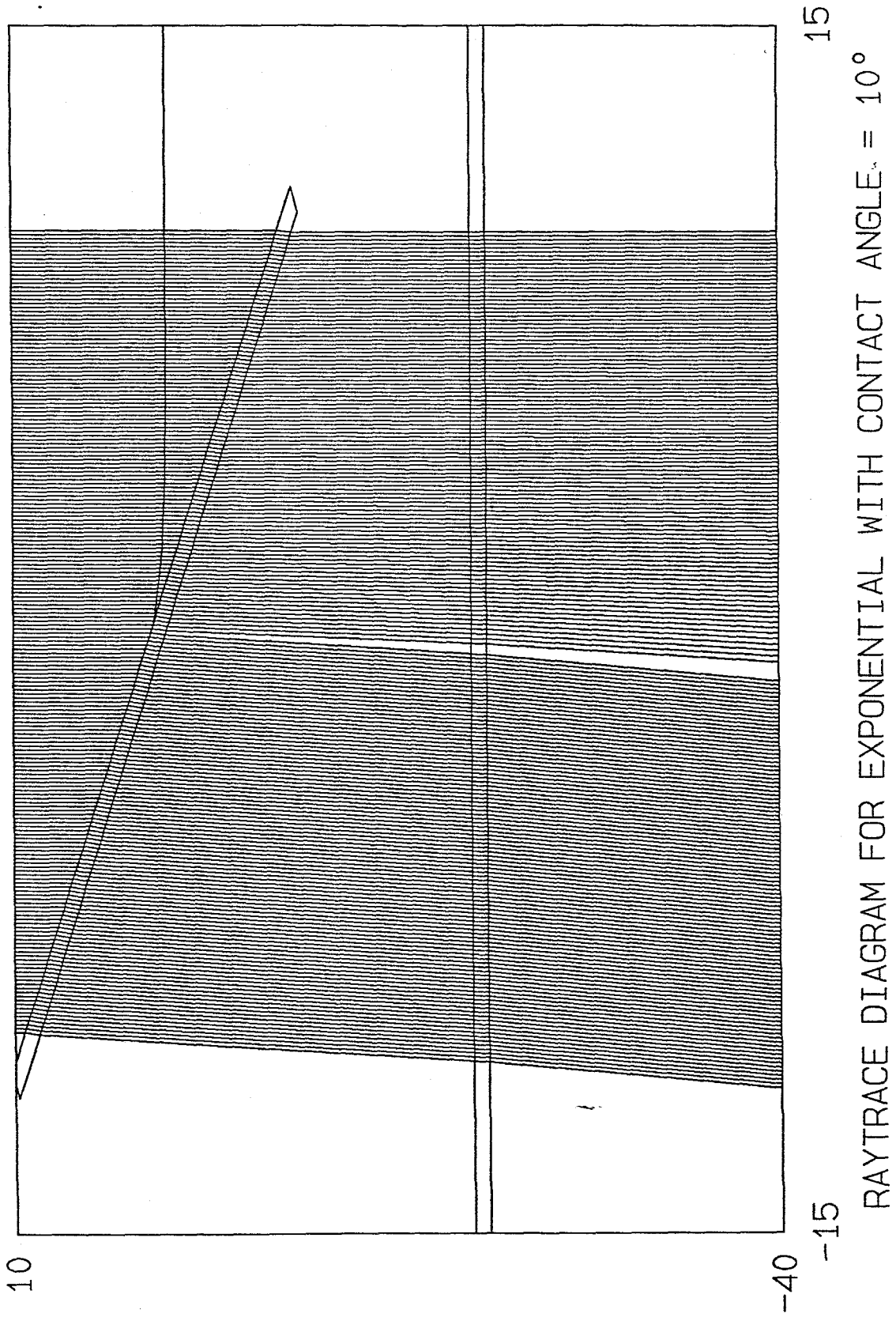
RAYTRACE DIAGRAM FOR EXPONENTIAL WITH CONTACT ANGLE = 10°
15
-15
10
-40

Figure 51

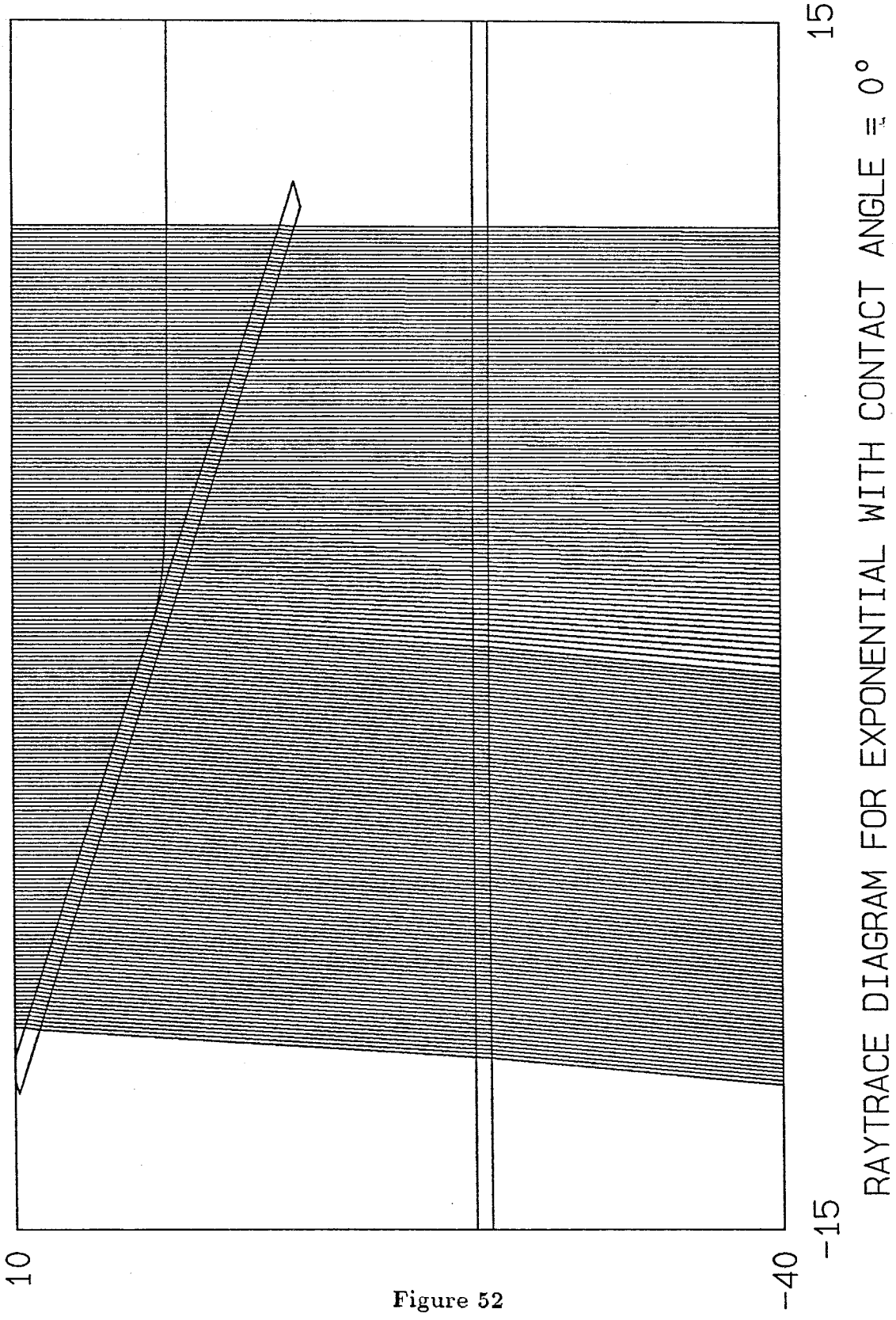
RAYTRACE DIAGRAM FOR EXPONENTIAL WITH CONTACT ANGLE = 0°
15
-15
10
-40

Figure 52

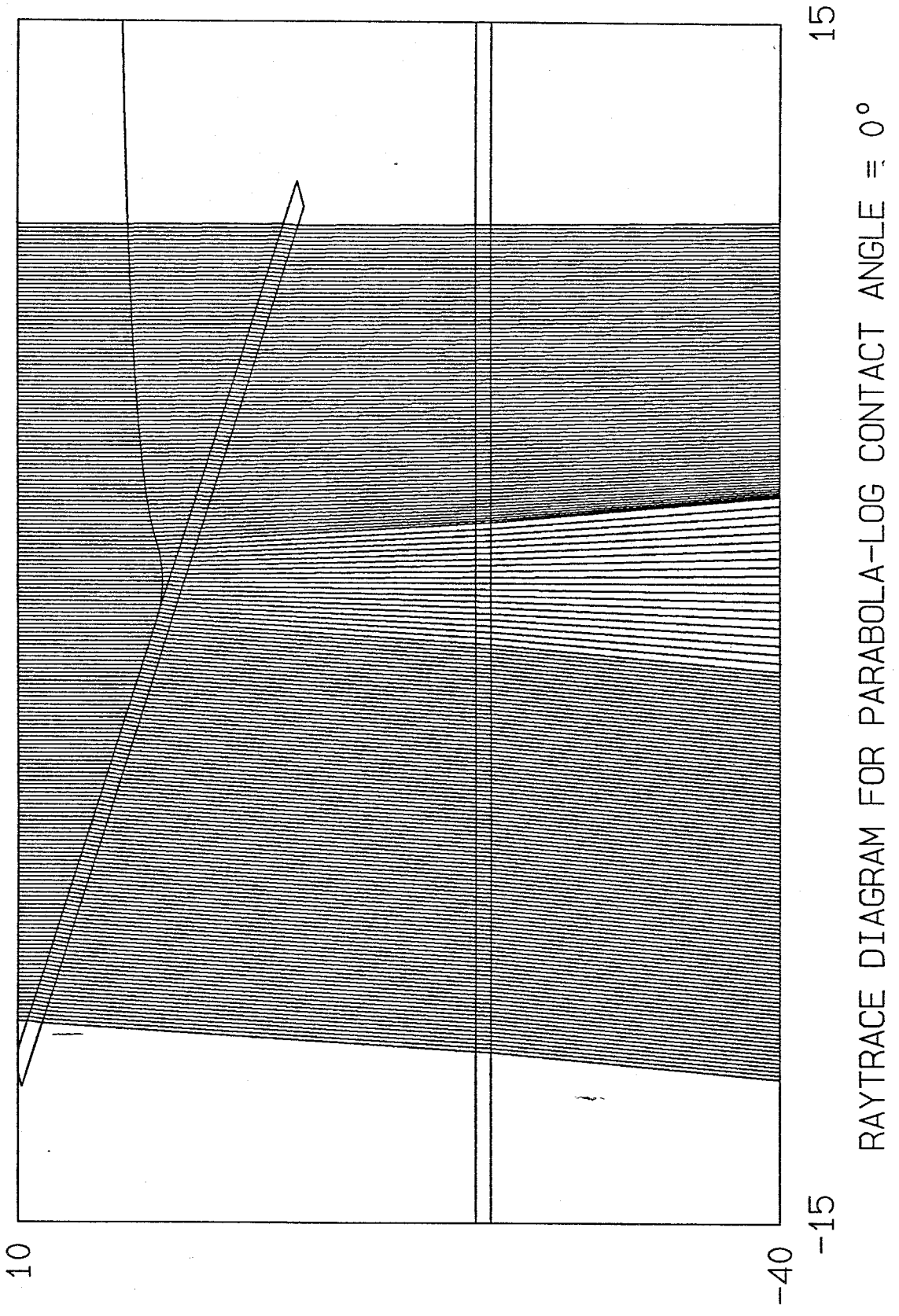
RAYTRACE DIAGRAM FOR PARABOLA-LOG CONTACT ANGLE = 0°
15
-15
10
-40

Figure 53

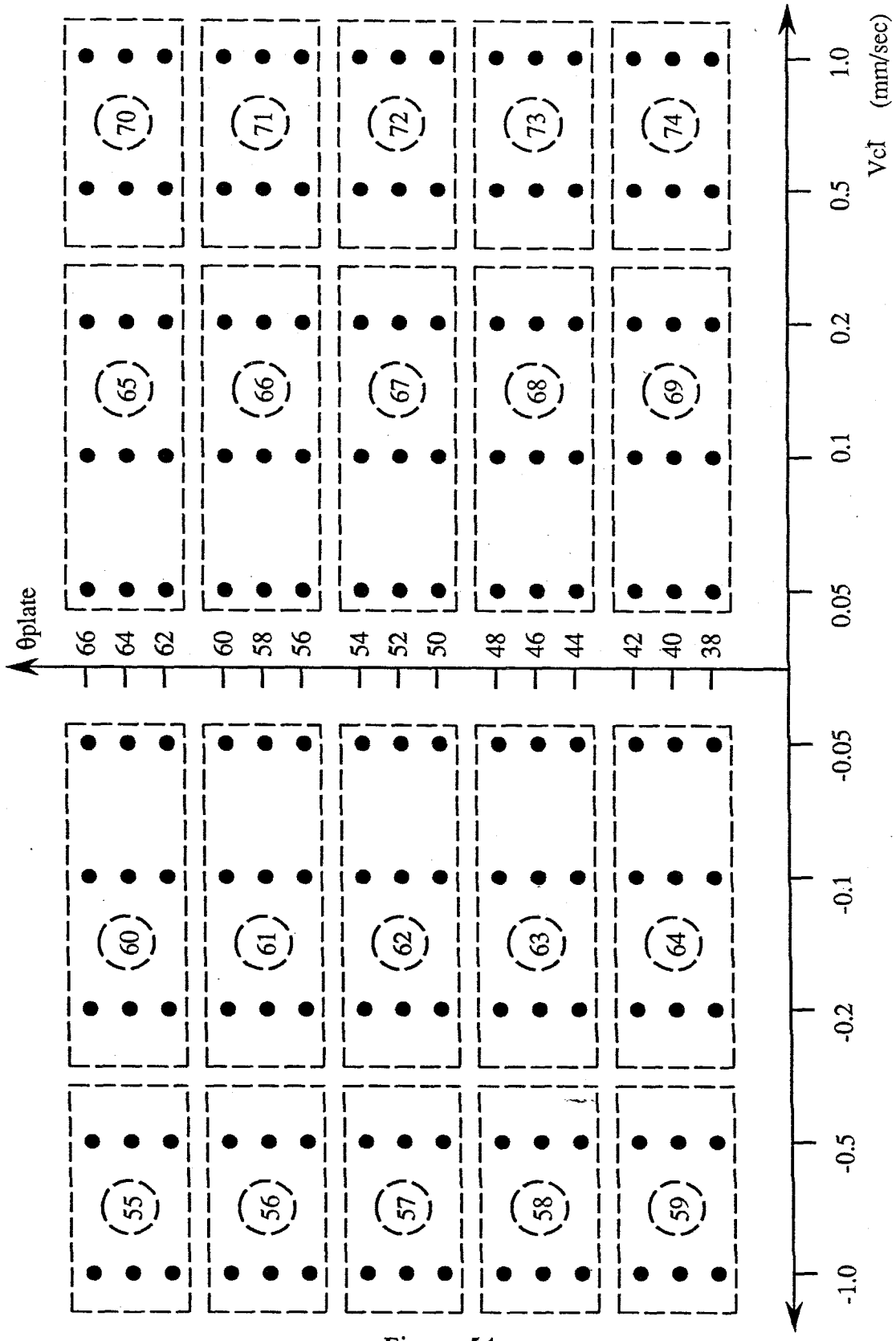

Figure 54

(Plate-angle, Velocity) space for "sticky"-plate experiments

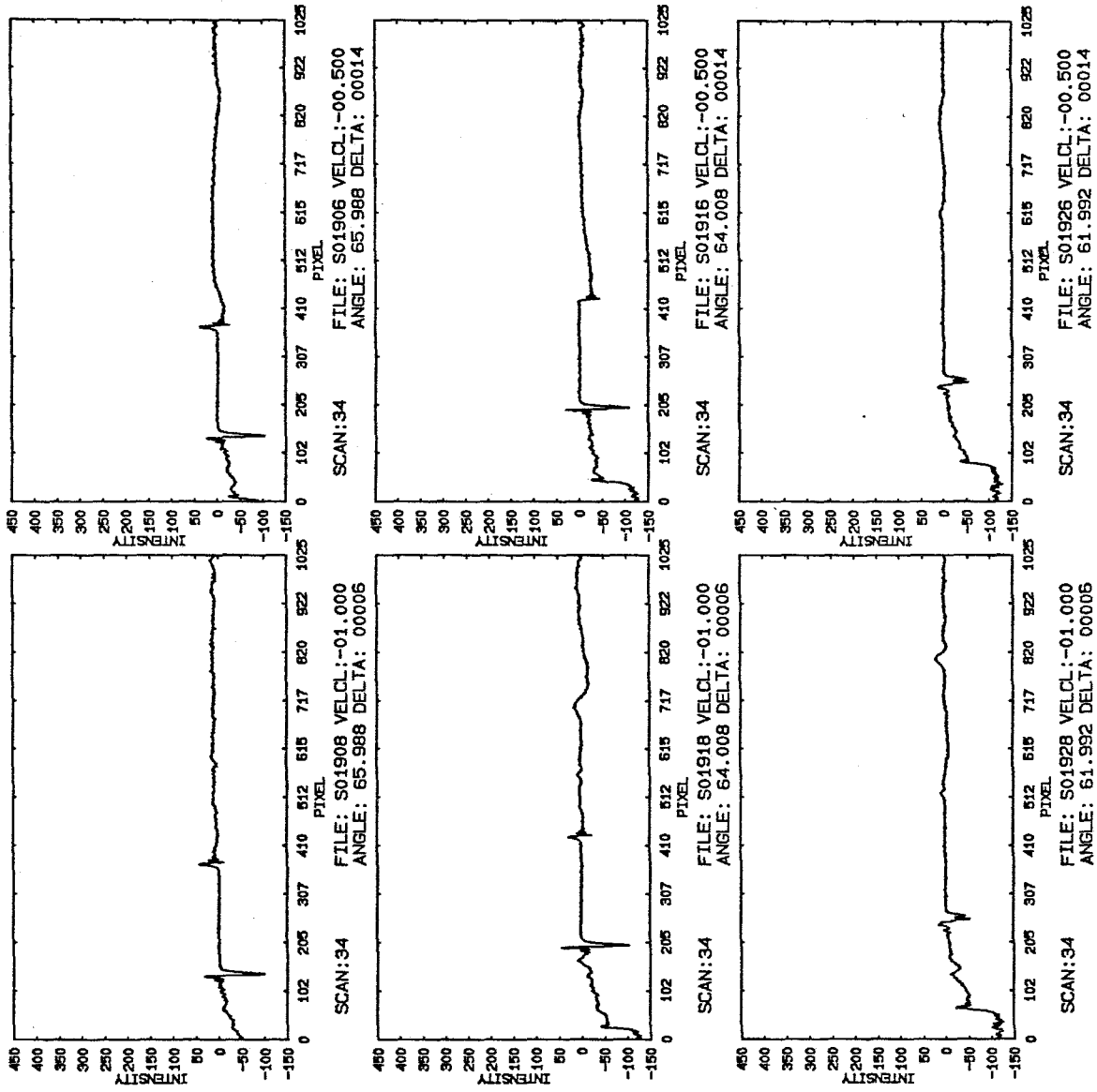
SCAN:34
FILE: S01906 VELCL:-00.500
ANGLE: 65.988 DELTA: 00014
SCAN:34
FILE: S01916 VELCL:-00.500
ANGLE: 64.008 DELTA: 00014
SCAN:34
FILE: S01926 VELCL:-00.500
ANGLE: 61.992 DELTA: 00014
SCAN:34
FILE: S01908 VELCL:-01.000
ANGLE: 65.988 DELTA: 00006
SCAN:34
FILE: S01918 VELCL:-01.000
ANGLE: 64.008 DELTA: 00006
SCAN:34
FILE: S01928 VELCL:-01.000
ANGLE: 61.992 DELTA: 00006
INTENSITY
PIXEL

Figure 55

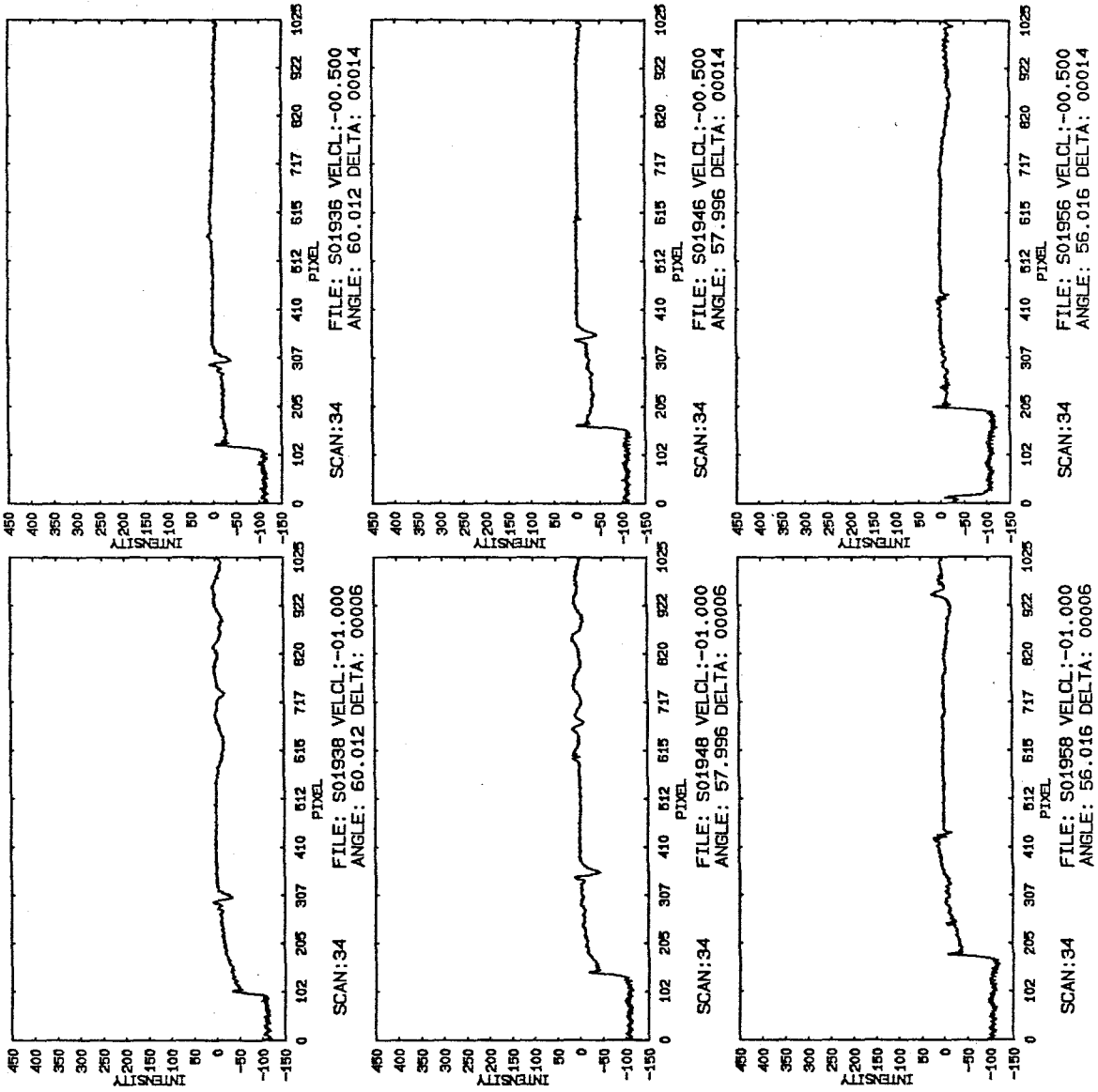
SCAN:34
FILE: S01936 VELCL:-00.500
ANGLE: 60.012 DELTA: 00014
SCAN:34
FILE: S01946 VELCL:-00.500
ANGLE: 57.996 DELTA: 00014
SCAN:34
FILE: S01956 VELCL:-00.500
ANGLE: 56.016 DELTA: 00014
SCAN:34
FILE: S01938 VELCL:-01.000
ANGLE: 60.012 DELTA: 00006
SCAN:34
FILE: S01948 VELCL:-01.000
ANGLE: 57.996 DELTA: 00006
SCAN:34
FILE: S01958 VELCL:-01.000
ANGLE: 56.016 DELTA: 00006
INTENSITY
PIXEL

Figure 56

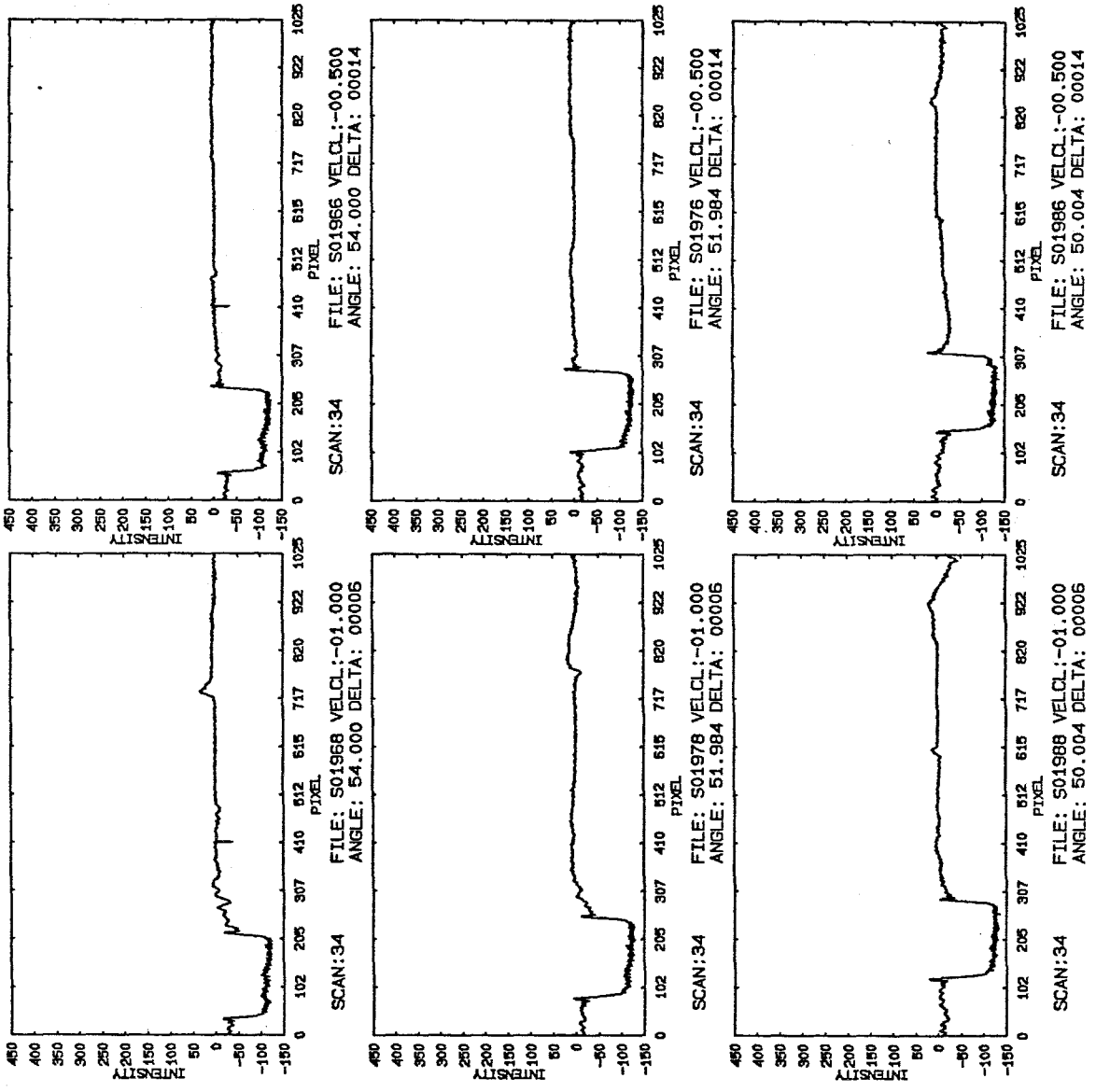
INTENSITY
PIXEL
SCAN:34
FILE: S01966 VELCL:-00.500
ANGLE: 54.000 DELTA: 00014
FILE: S01968 VELCL:-01.000
ANGLE: 54.000 DELTA: 00006
FILE: S01976 VELCL:-00.500
ANGLE: 51.984 DELTA: 00014
FILE: S01978 VELCL:-01.000
ANGLE: 51.984 DELTA: 00006
FILE: S01986 VELCL:-00.500
ANGLE: 50.004 DELTA: 00014
FILE: S01988 VELCL:-01.000
ANGLE: 50.004 DELTA: 00006

Figure 57

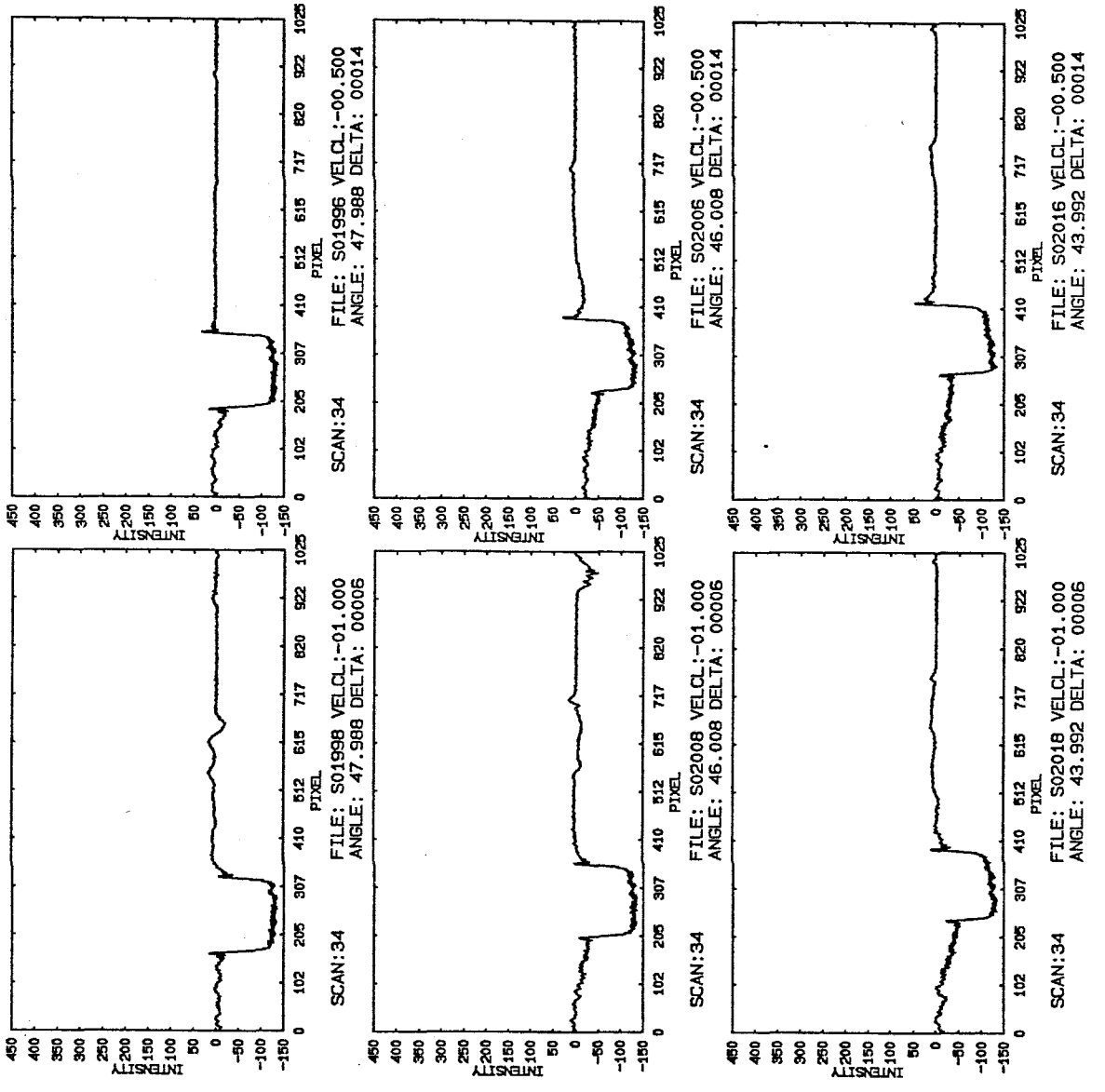
SCAN:34
FILE: S01998 VELCL:-01.000
ANGLE: 47.988 DELTA: 00006
SCAN:34
FILE: S01996 VELCL:-00.500
ANGLE: 47.988 DELTA: 00014
SCAN:34
FILE: S02008 VELCL:-01.000
ANGLE: 46.008 DELTA: 00006
SCAN:34
FILE: S02006 VELCL:-00.500
ANGLE: 46.008 DELTA: 00014
SCAN:34
FILE: S02018 VELCL:-01.000
ANGLE: 43.992 DELTA: 00006
SCAN:34
FILE: S02016 VELCL:-00.500
ANGLE: 43.992 DELTA: 00014
INTENSITY
PIXEL

Figure 58

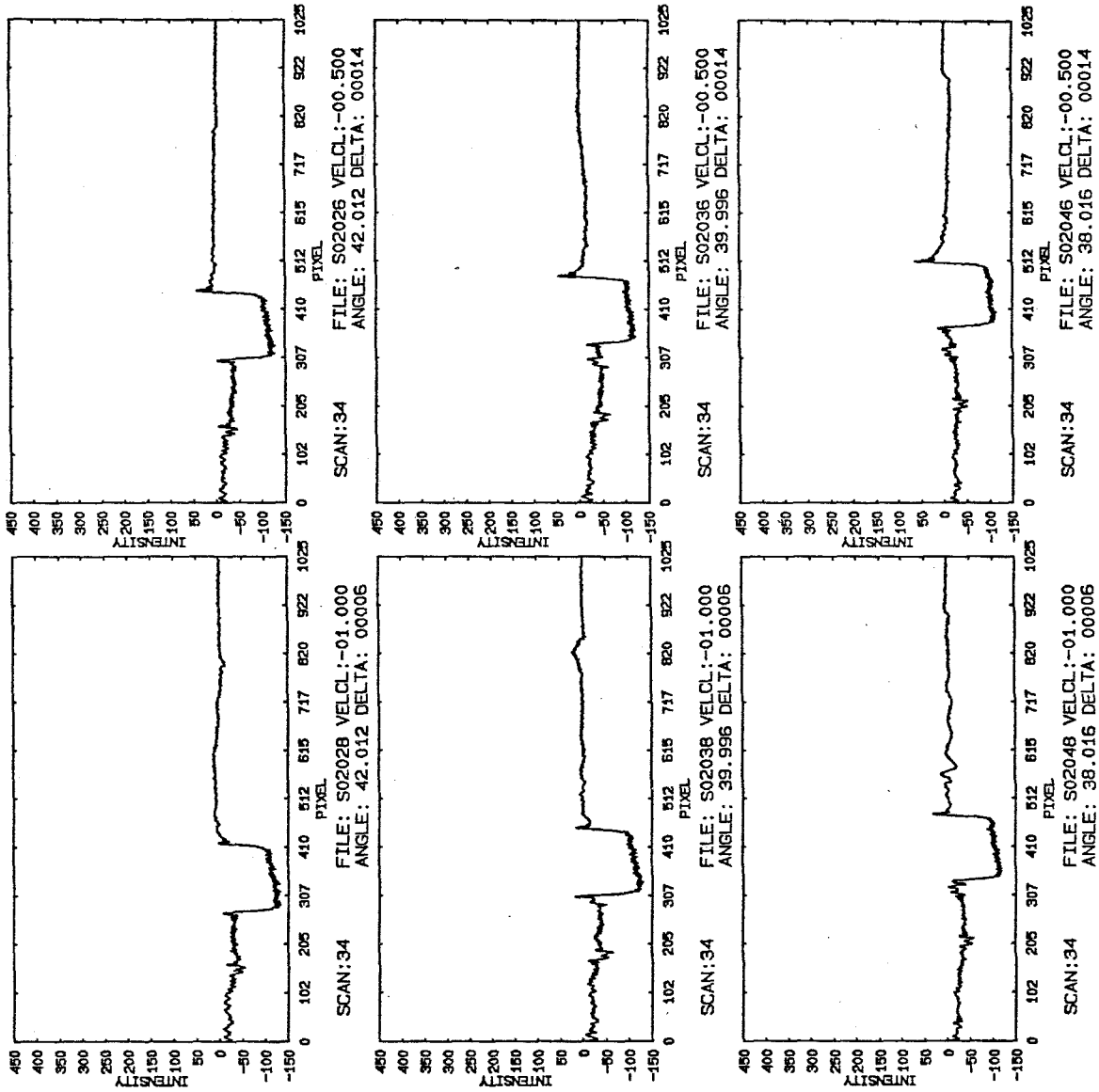
INTENSITY
PIXEL
SCAN:34
FILE: S02026 VELCL:-00.500
ANGLE: 42.012 DELTA: 00014
FILE: S02028 VELCL:-01.000
ANGLE: 42.012 DELTA: 00006
FILE: S02036 VELCL:-00.500
ANGLE: 39.996 DELTA: 00014
FILE: S02038 VELCL:-01.000
ANGLE: 39.996 DELTA: 00006
FILE: S02046 VELCL:-00.500
ANGLE: 38.016 DELTA: 00014
FILE: S02048 VELCL:-01.000
ANGLE: 38.016 DELTA: 00006

Figure 59

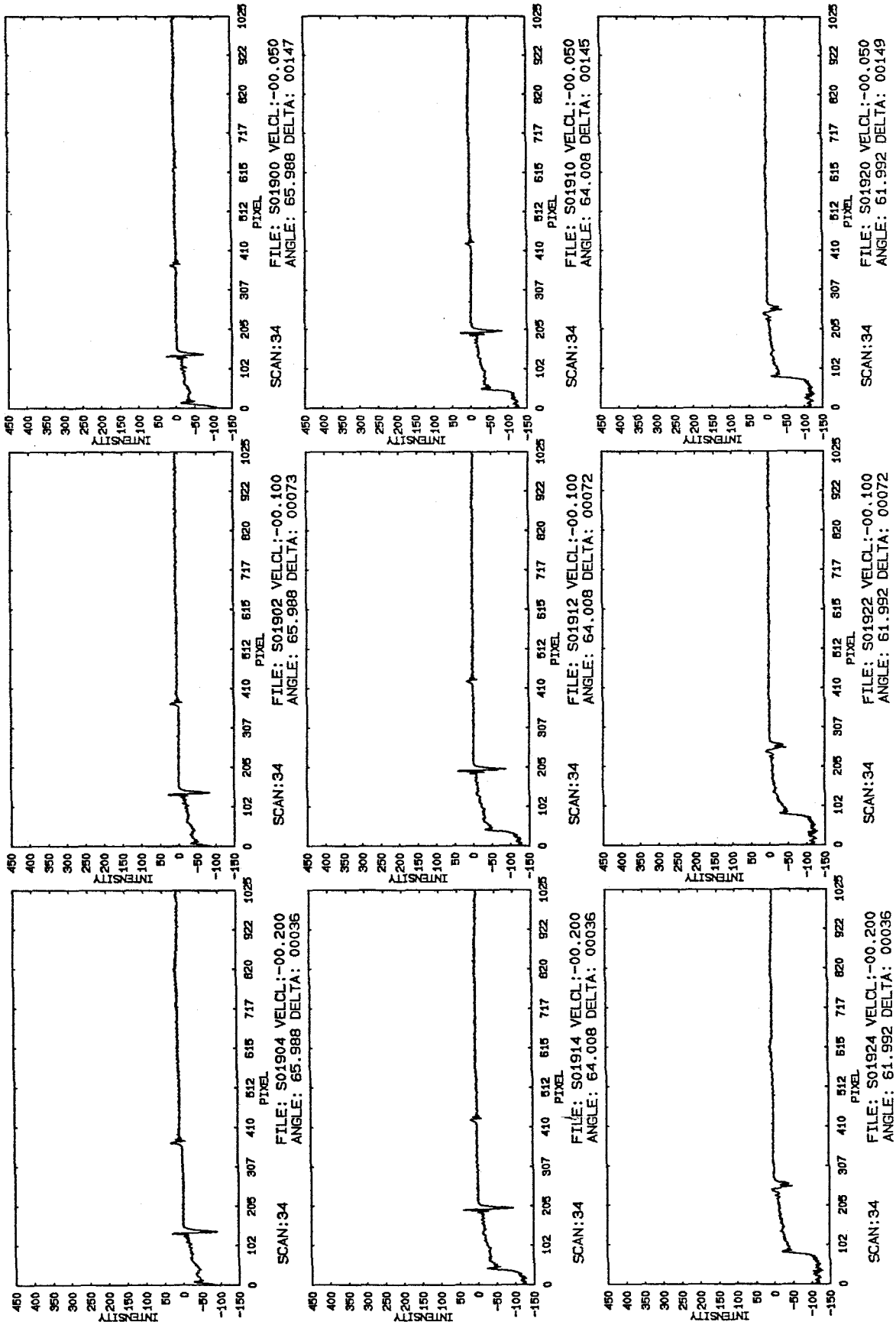
INTENSITY
PIXEL
SCAN:34
FILE: S01900 VELCL:-00.050
ANGLE: 65.988 DELTA: 00147
FILE: S01902 VELCL:-00.100
ANGLE: 65.988 DELTA: 00073
FILE: S01904 VELCL:-00.200
ANGLE: 65.988 DELTA: 00036
FILE: S01910 VELCL:-00.050
ANGLE: 64.008 DELTA: 00145
FILE: S01912 VELCL:-00.100
ANGLE: 64.008 DELTA: 00072
FILE: S01914 VELCL:-00.200
ANGLE: 64.008 DELTA: 00036
FILE: S01920 VELCL:-00.050
ANGLE: 61.992 DELTA: 00149
FILE: S01922 VELCL:-00.100
ANGLE: 61.992 DELTA: 00072
FILE: S01924 VELCL:-00.200
ANGLE: 61.992 DELTA: 00036

Figure 60

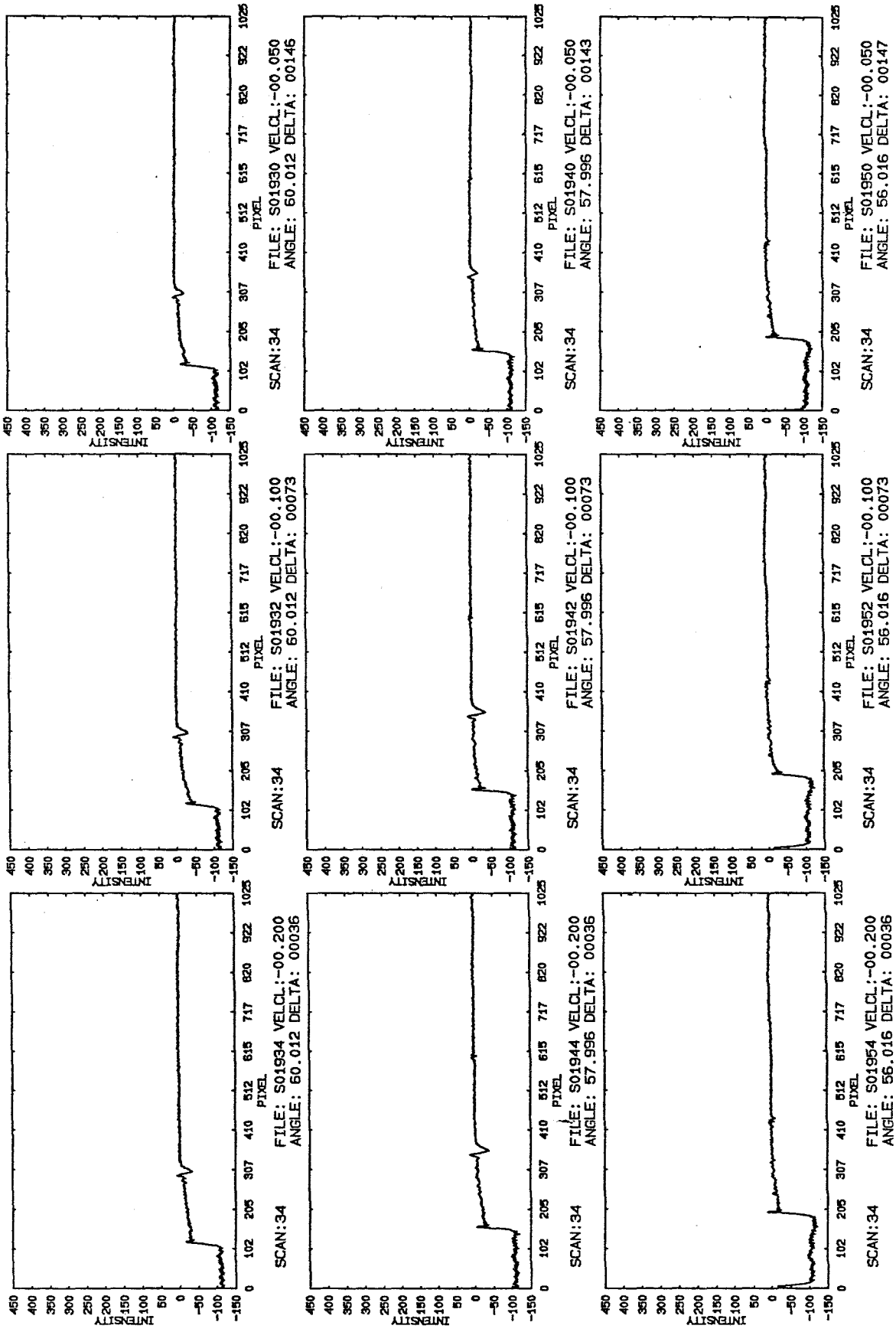
INTENSITY
PIXEL
SCAN:34
FILE: S01930 VELCL:-00.050
ANGLE: 60.012 DELTA: 00146
FILE: S01932 VELCL:-00.100
ANGLE: 60.012 DELTA: 00073
FILE: S01934 VELCL:-00.200
ANGLE: 60.012 DELTA: 00036
FILE: S01940 VELCL:-00.050
ANGLE: 57.996 DELTA: 00143
FILE: S01942 VELCL:-00.100
ANGLE: 57.996 DELTA: 00073
FILE: S01944 VELCL:-00.200
ANGLE: 57.996 DELTA: 00036
FILE: S01950 VELCL:-00.050
ANGLE: 56.016 DELTA: 00147
FILE: S01952 VELCL:-00.100
ANGLE: 56.016 DELTA: 00073
FILE: S01954 VELCL:-00.200
ANGLE: 56.016 DELTA: 00036

Figure 61

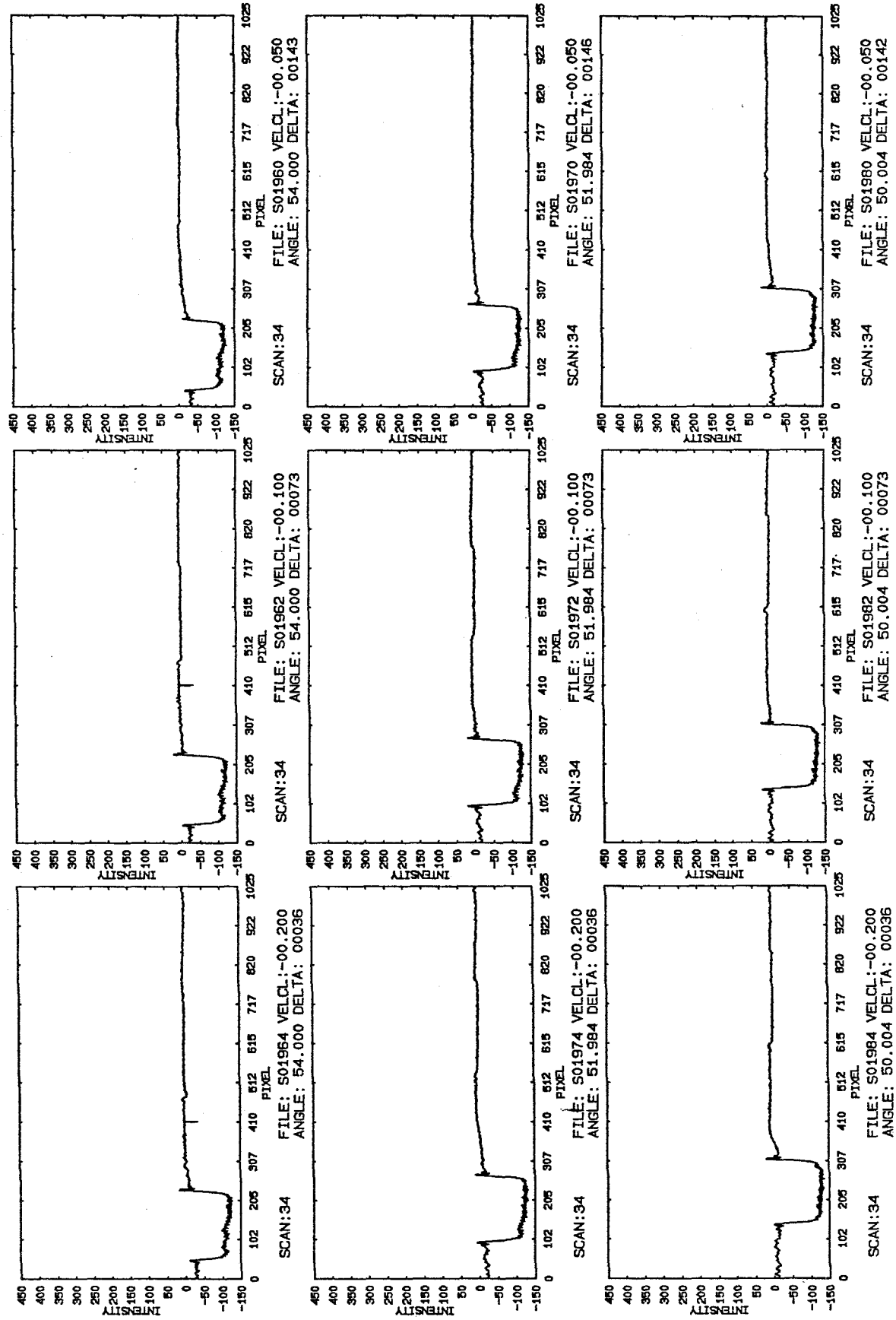
INTENSITY
PIXEL
SCAN:34
FILE: S01964 VELCL:-00.200
ANGLE: 54.000 DELTA: 00036
FILE: S01962 VELCL:-00.100
ANGLE: 54.000 DELTA: 00073
FILE: S01960 VELCL:-00.050
ANGLE: 54.000 DELTA: 00143
FILE: S01974 VELCL:-00.200
ANGLE: 51.984 DELTA: 00036
FILE: S01972 VELCL:-00.100
ANGLE: 51.984 DELTA: 00073
FILE: S01970 VELCL:-00.050
ANGLE: 51.984 DELTA: 00146
FILE: S01984 VELCL:-00.200
ANGLE: 50.004 DELTA: 00036
FILE: S01982 VELCL:-00.100
ANGLE: 50.004 DELTA: 00073
FILE: S01980 VELCL:-00.050
ANGLE: 50.004 DELTA: 00142

Figure 62

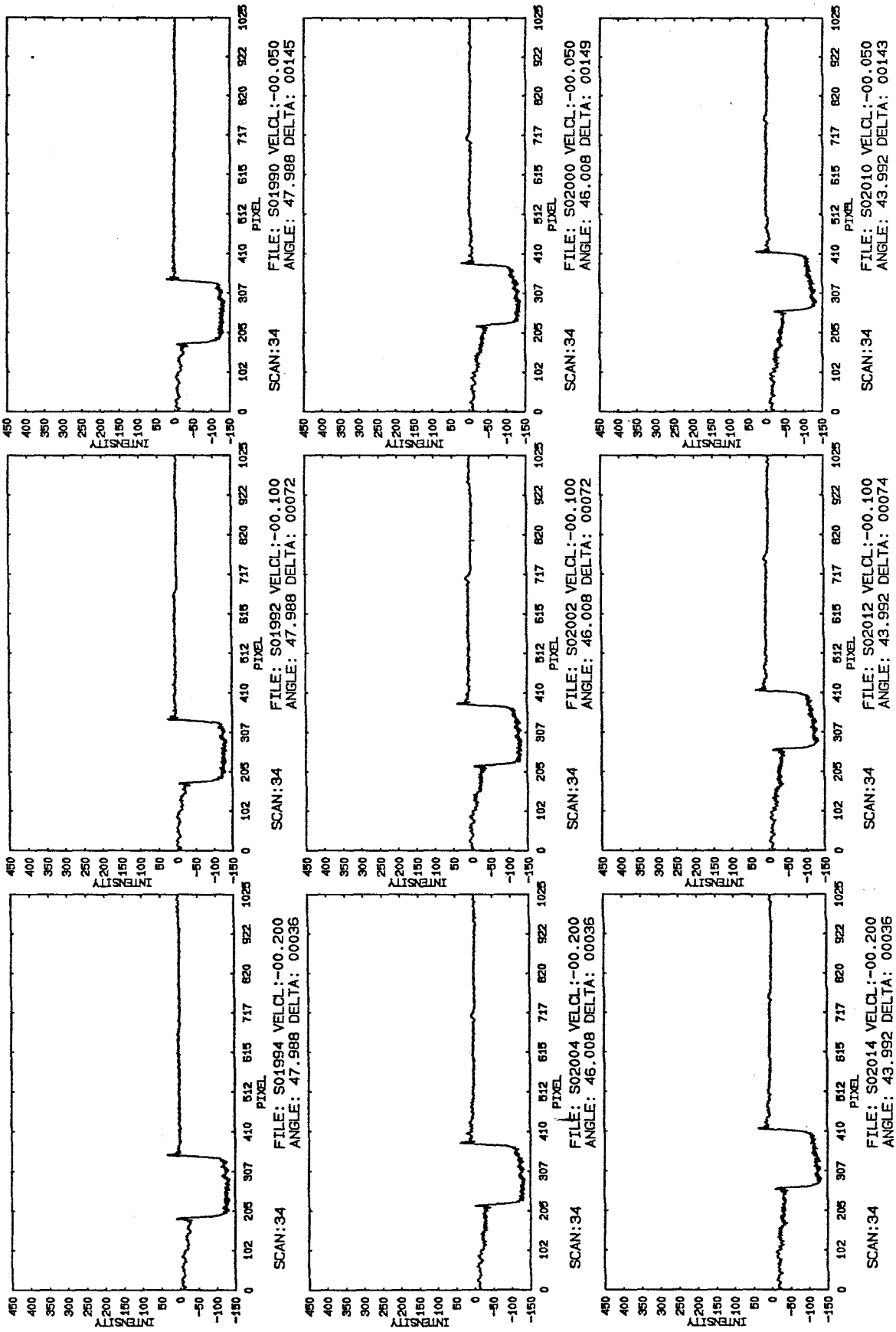
INTENSITY
PIXEL
SCAN:34
FILE: S01990 VELCL:-00.050
ANGLE: 47.988 DELTA: 00145
FILE: S01992 VELCL:-00.100
ANGLE: 47.988 DELTA: 00072
FILE: S01994 VELCL:-00.200
ANGLE: 47.988 DELTA: 00036
FILE: S02000 VELCL:-00.050
ANGLE: 46.008 DELTA: 00149
FILE: S02002 VELCL:-00.100
ANGLE: 46.008 DELTA: 00072
FILE: S02004 VELCL:-00.200
ANGLE: 46.008 DELTA: 00036
FILE: S02010 VELCL:-00.050
ANGLE: 43.992 DELTA: 00143
FILE: S02012 VELCL:-00.100
ANGLE: 43.992 DELTA: 00074
FILE: S02014 VELCL:-00.200
ANGLE: 43.992 DELTA: 00036

Figure 63

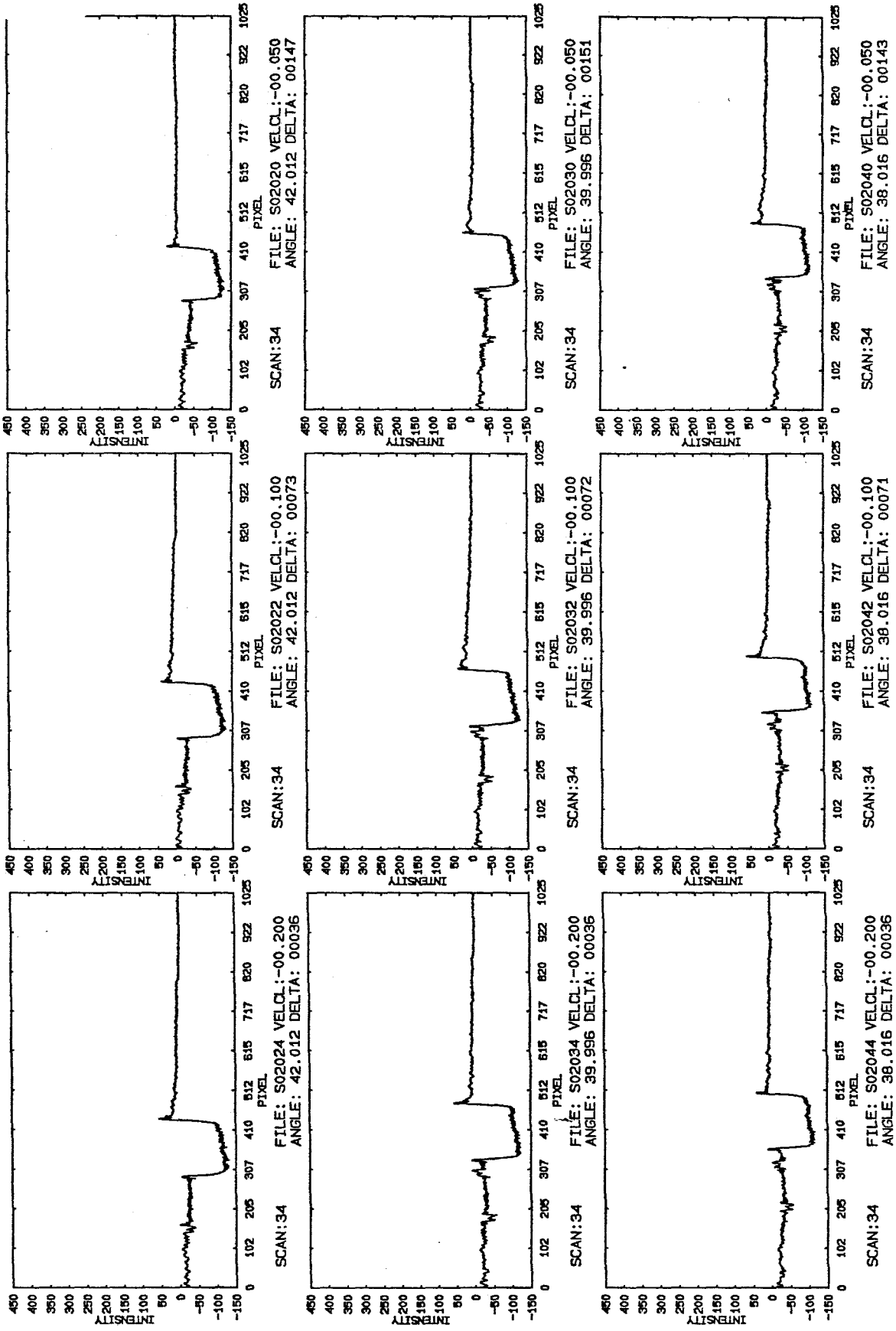
INTENSITY
PIXEL
SCAN:34
FILE: S02020 VELCL:-00.050
ANGLE: 42.012 DELTA: 00147
FILE: S02022 VELCL:-00.100
ANGLE: 42.012 DELTA: 00073
FILE: S02024 VELCL:-00.200
ANGLE: 42.012 DELTA: 00036
FILE: S02030 VELCL:-00.050
ANGLE: 39.996 DELTA: 00151
FILE: S02032 VELCL:-00.100
ANGLE: 39.996 DELTA: 00072
FILE: S02034 VELCL:-00.200
ANGLE: 39.996 DELTA: 00036
FILE: S02040 VELCL:-00.050
ANGLE: 38.016 DELTA: 00143
FILE: S02042 VELCL:-00.100
ANGLE: 38.016 DELTA: 00071
FILE: S02044 VELCL:-00.200
ANGLE: 38.016 DELTA: 00036

Figure 64

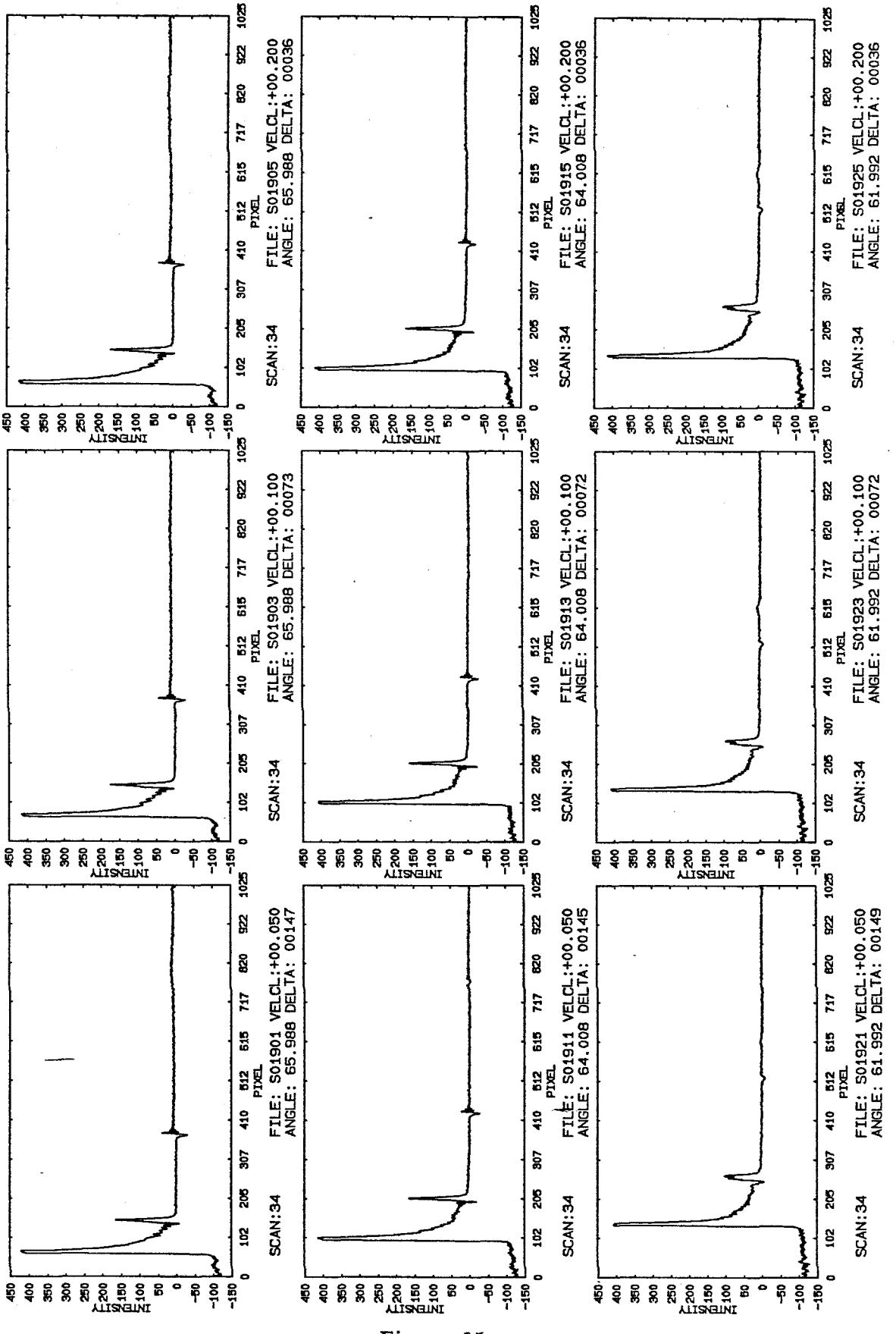
INTENSITY
PIXEL
SCAN:34
FILE: S01901 VELCL:+00.050
ANGLE: 65.988 DELTA: 00147
FILE: S01903 VELCL:+00.100
ANGLE: 65.988 DELTA: 00073
FILE: S01905 VELCL:+00.200
ANGLE: 65.988 DELTA: 00036
FILE: S01911 VELCL:+00.050
ANGLE: 64.008 DELTA: 00145
FILE: S01913 VELCL:+00.100
ANGLE: 64.008 DELTA: 00072
FILE: S01915 VELCL:+00.200
ANGLE: 64.008 DELTA: 00036
FILE: S01921 VELCL:+00.050
ANGLE: 61.992 DELTA: 00149
FILE: S01923 VELCL:+00.100
ANGLE: 61.992 DELTA: 00072
FILE: S01925 VELCL:+00.200
ANGLE: 61.992 DELTA: 00036

Figure 65

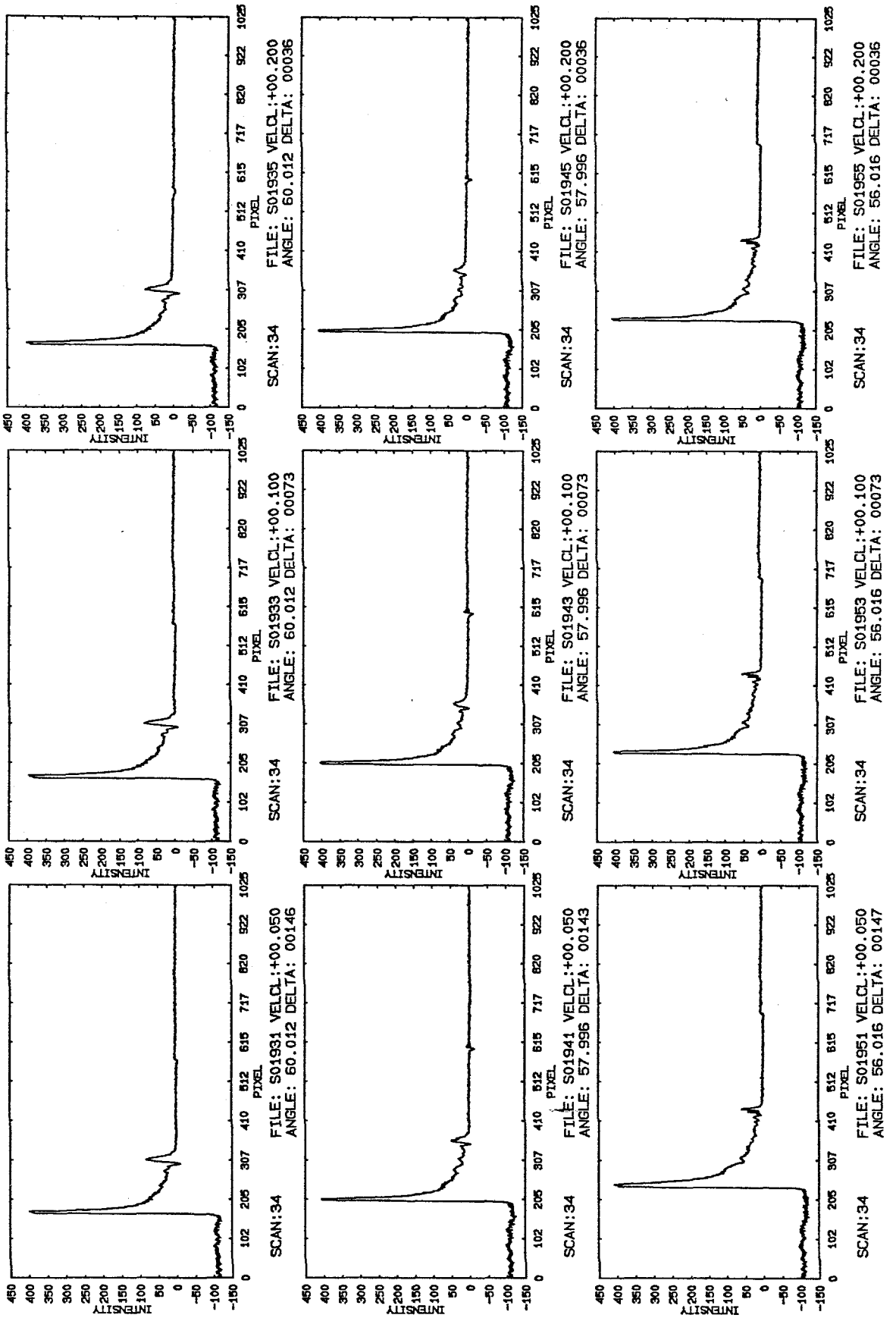
INTENSITY
PIXEL
SCAN:34
FILE: S01931 VELCL:+00.050
ANGLE: 60.012 DELTA: 00146
FILE: S01933 VELCL:+00.100
ANGLE: 60.012 DELTA: 00073
FILE: S01935 VELCL:+00.200
ANGLE: 60.012 DELTA: 00036
FILE: S01941 VELCL:+00.050
ANGLE: 57.996 DELTA: 00143
FILE: S01943 VELCL:+00.100
ANGLE: 57.996 DELTA: 00073
FILE: S01945 VELCL:+00.200
ANGLE: 57.996 DELTA: 00036
FILE: S01951 VELCL:+00.050
ANGLE: 56.016 DELTA: 00147
FILE: S01953 VELCL:+00.100
ANGLE: 56.016 DELTA: 00073
FILE: S01955 VELCL:+00.200
ANGLE: 56.016 DELTA: 00036

Figure 66

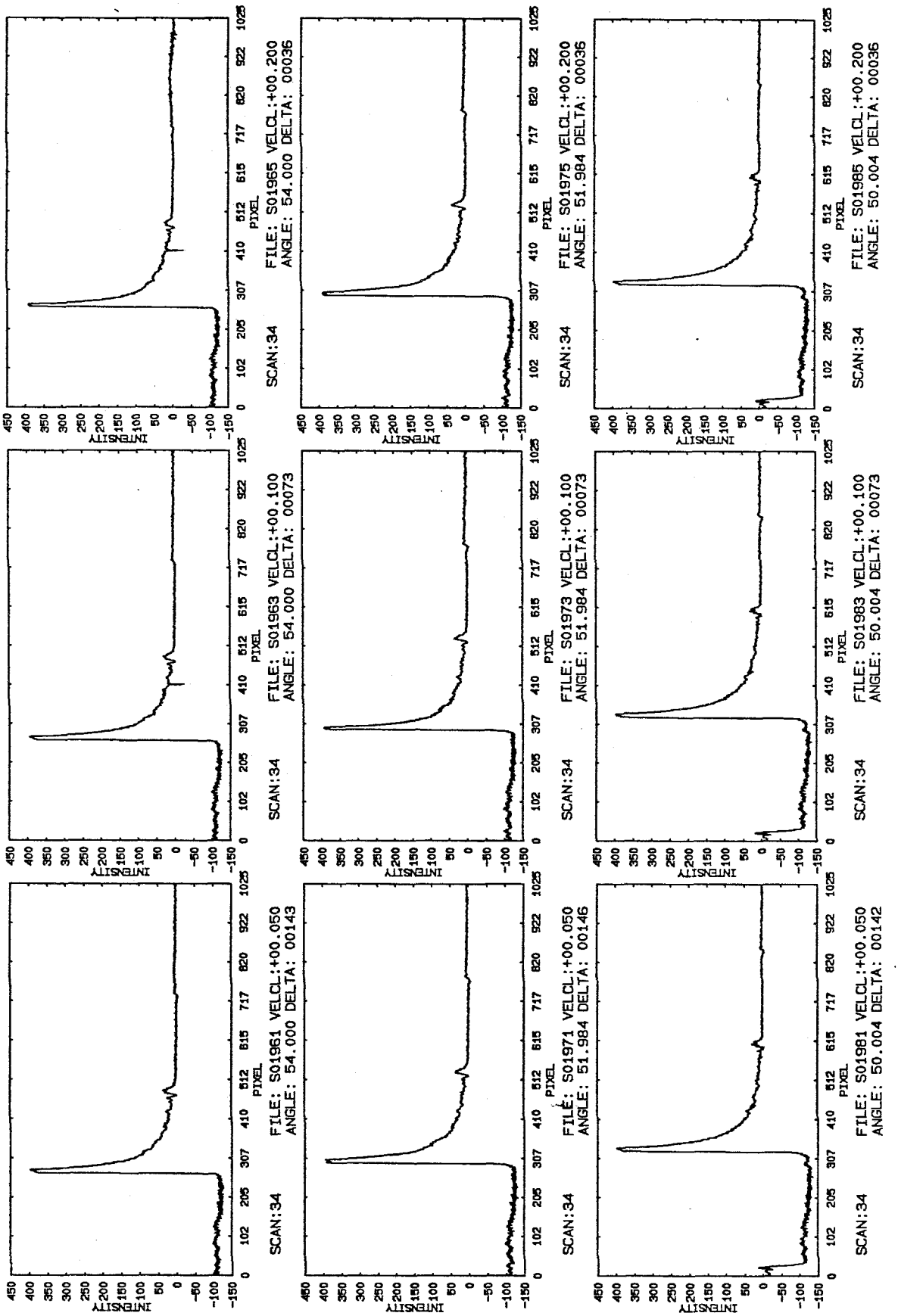
INTENSITY
PIXEL
SCAN:34
FILE: S01961 VELCL:+00.050
ANGLE: 54.000 DELTA: 00143
FILE: S01963 VELCL:+00.100
ANGLE: 54.000 DELTA: 00073
FILE: S01965 VELCL:+00.200
ANGLE: 54.000 DELTA: 00036
FILE: S01971 VELCL:+00.050
ANGLE: 51.984 DELTA: 00146
FILE: S01973 VELCL:+00.100
ANGLE: 51.984 DELTA: 00073
FILE: S01975 VELCL:+00.200
ANGLE: 51.984 DELTA: 00036
FILE: S01981 VELCL:+00.050
ANGLE: 50.004 DELTA: 00142
FILE: S01983 VELCL:+00.100
ANGLE: 50.004 DELTA: 00073
FILE: S01985 VELCL:+00.200
ANGLE: 50.004 DELTA: 00036

Figure 67

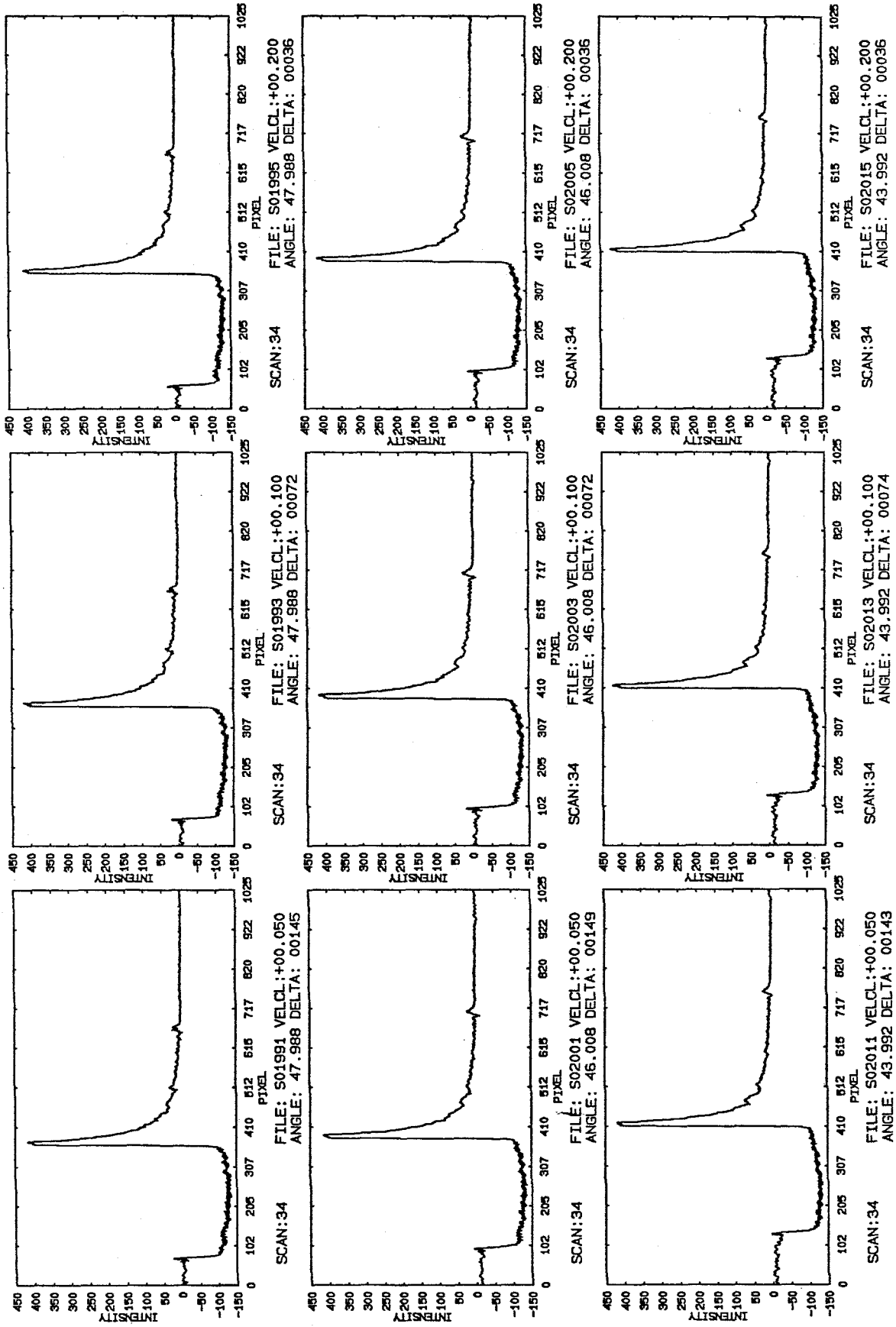
INTENSITY
PIXEL
SCAN:34
FILE: S01995 VELCL:+00.200
ANGLE: 47.988 DELTA: 00036
FILE: S01993 VELCL:+00.100
ANGLE: 47.988 DELTA: 00072
FILE: S01991 VELCL:+00.050
ANGLE: 47.988 DELTA: 00145
FILE: S02005 VELCL:+00.200
ANGLE: 46.008 DELTA: 00036
FILE: S02003 VELCL:+00.100
ANGLE: 46.008 DELTA: 00072
FILE: S02001 VELCL:+00.050
ANGLE: 46.008 DELTA: 00149
FILE: S02015 VELCL:+00.200
ANGLE: 43.992 DELTA: 00036
FILE: S02013 VELCL:+00.100
ANGLE: 43.992 DELTA: 00074
FILE: S02011 VELCL:+00.050
ANGLE: 43.992 DELTA: 00143

Figure 68

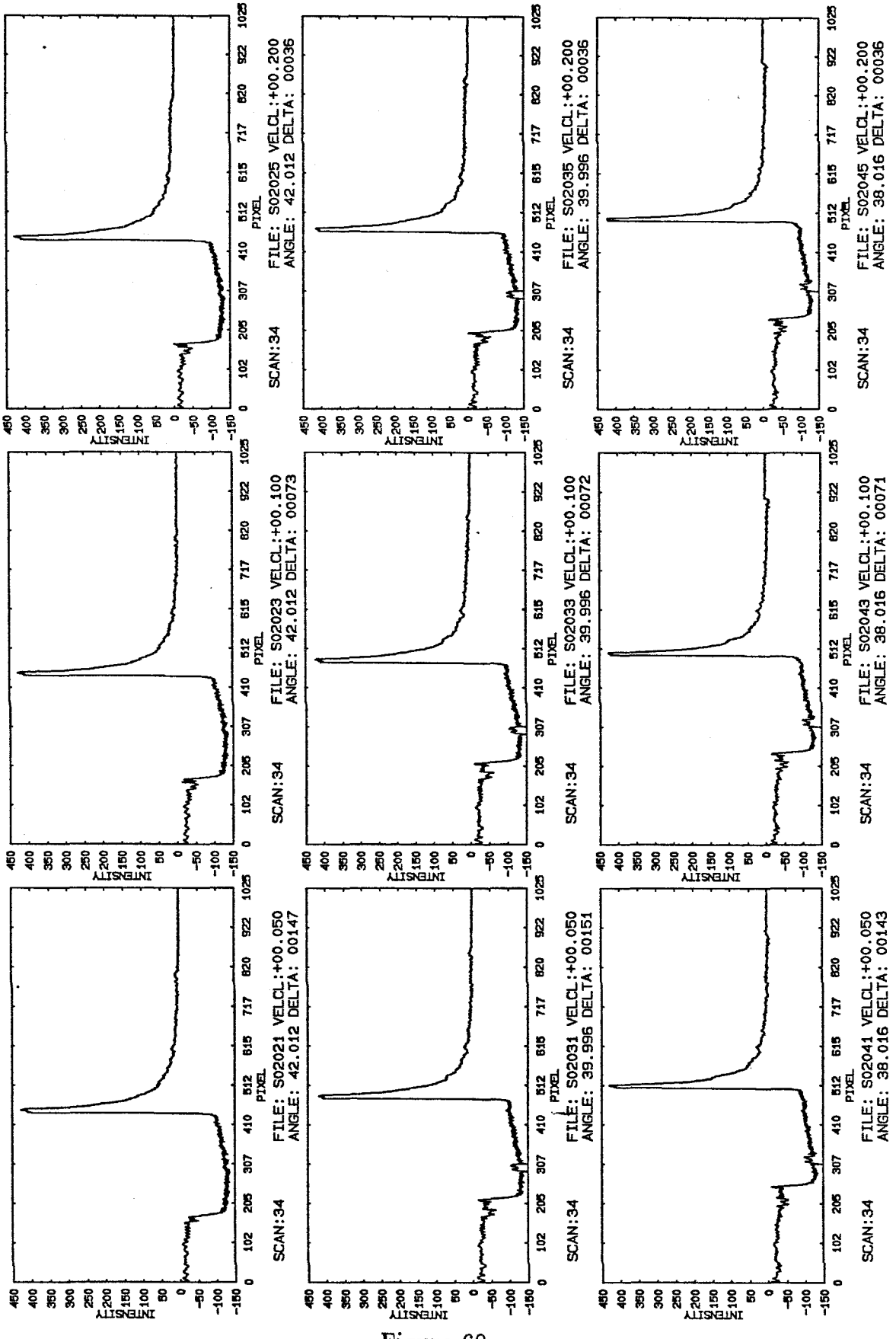
INTENSITY
PIXEL
SCAN:34
FILE: S02021 VELCL:+00.050
ANGLE: 42.012 DELTA: 00147
FILE: S02031 VELCL:+00.050
ANGLE: 39.996 DELTA: 00151
FILE: S02041 VELCL:+00.050
ANGLE: 38.016 DELTA: 00143
FILE: S02023 VELCL:+00.100
ANGLE: 42.012 DELTA: 00073
FILE: S02033 VELCL:+00.100
ANGLE: 39.996 DELTA: 00072
FILE: S02043 VELCL:+00.100
ANGLE: 38.016 DELTA: 00071
FILE: S02025 VELCL:+00.200
ANGLE: 42.012 DELTA: 00036
FILE: S02035 VELCL:+00.200
ANGLE: 39.996 DELTA: 00036
FILE: S02045 VELCL:+00.200
ANGLE: 38.016 DELTA: 00036

Figure 69

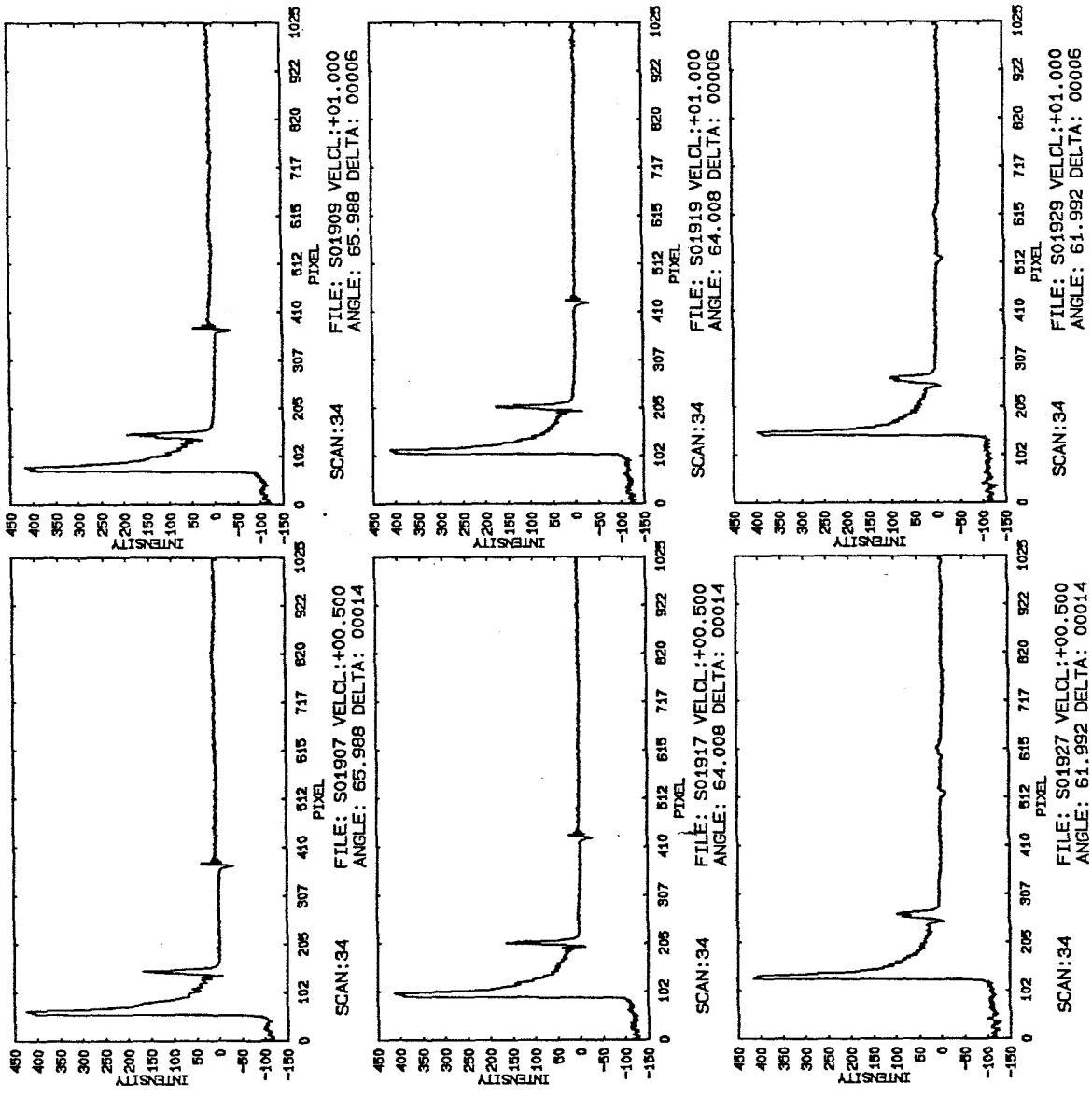
INTENSITY
PIXEL
SCAN:34
FILE: S01907 VELCL:+00.500
ANGLE: 65.988 DELTA: 00014
FILE: S01909 VELCL:+01.000
ANGLE: 65.988 DELTA: 00006
FILE: S01917 VELCL:+00.500
ANGLE: 64.008 DELTA: 00014
FILE: S01919 VELCL:+01.000
ANGLE: 64.008 DELTA: 00006
FILE: S01927 VELCL:+00.500
ANGLE: 61.992 DELTA: 00014
FILE: S01929 VELCL:+01.000
ANGLE: 61.992 DELTA: 00006

Figure 70

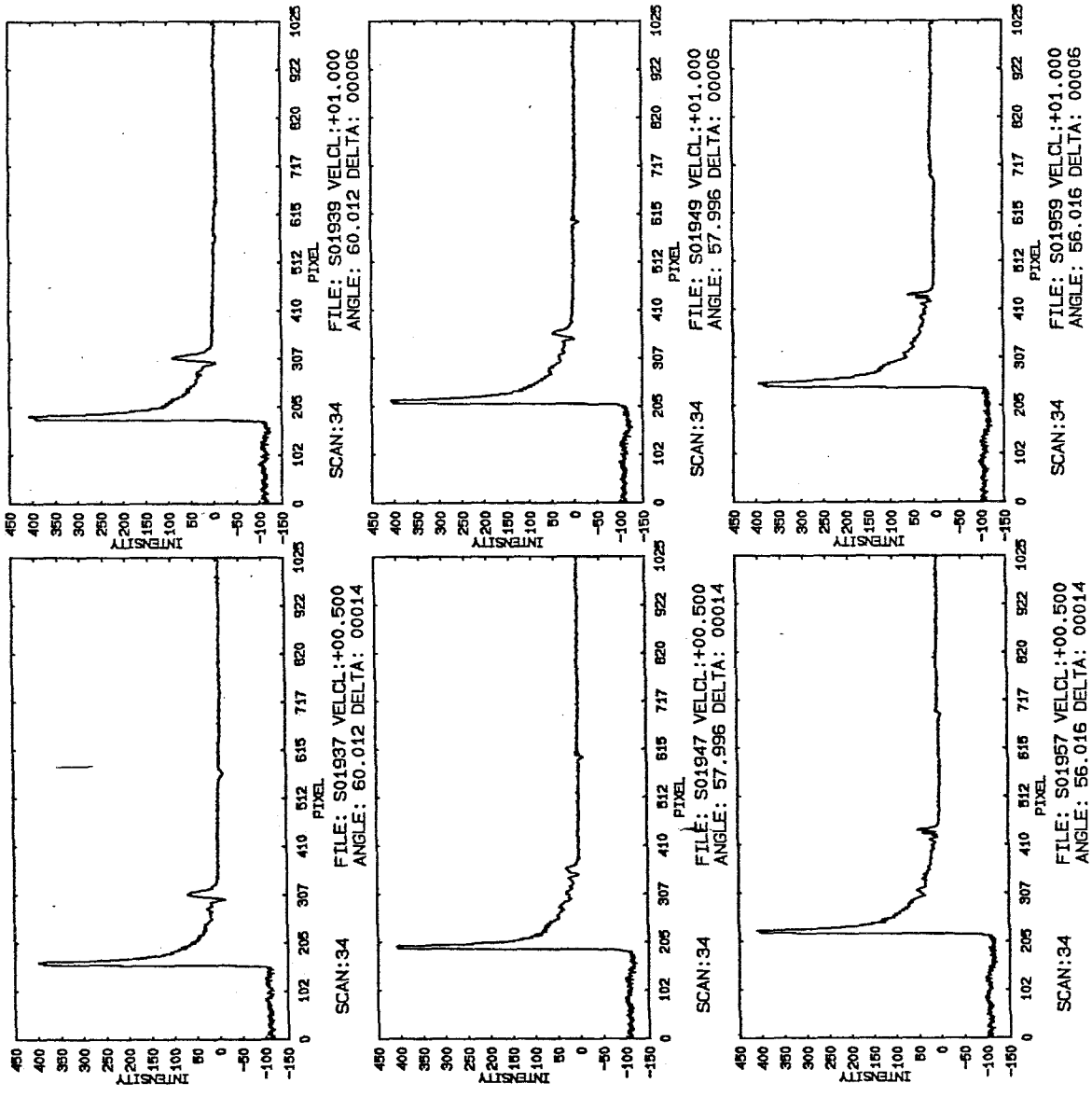
INTENSITY
PIXEL
SCAN:34
FILE: S01937 VELCL:+00.500
ANGLE: 60.012 DELTA: 00014
FILE: S01939 VELCL:+01.000
ANGLE: 60.012 DELTA: 00006
FILE: S01947 VELCL:+00.500
ANGLE: 57.996 DELTA: 00014
FILE: S01949 VELCL:+01.000
ANGLE: 57.996 DELTA: 00006
FILE: S01957 VELCL:+00.500
ANGLE: 56.016 DELTA: 00014
FILE: S01959 VELCL:+01.000
ANGLE: 56.016 DELTA: 00006

Figure 71

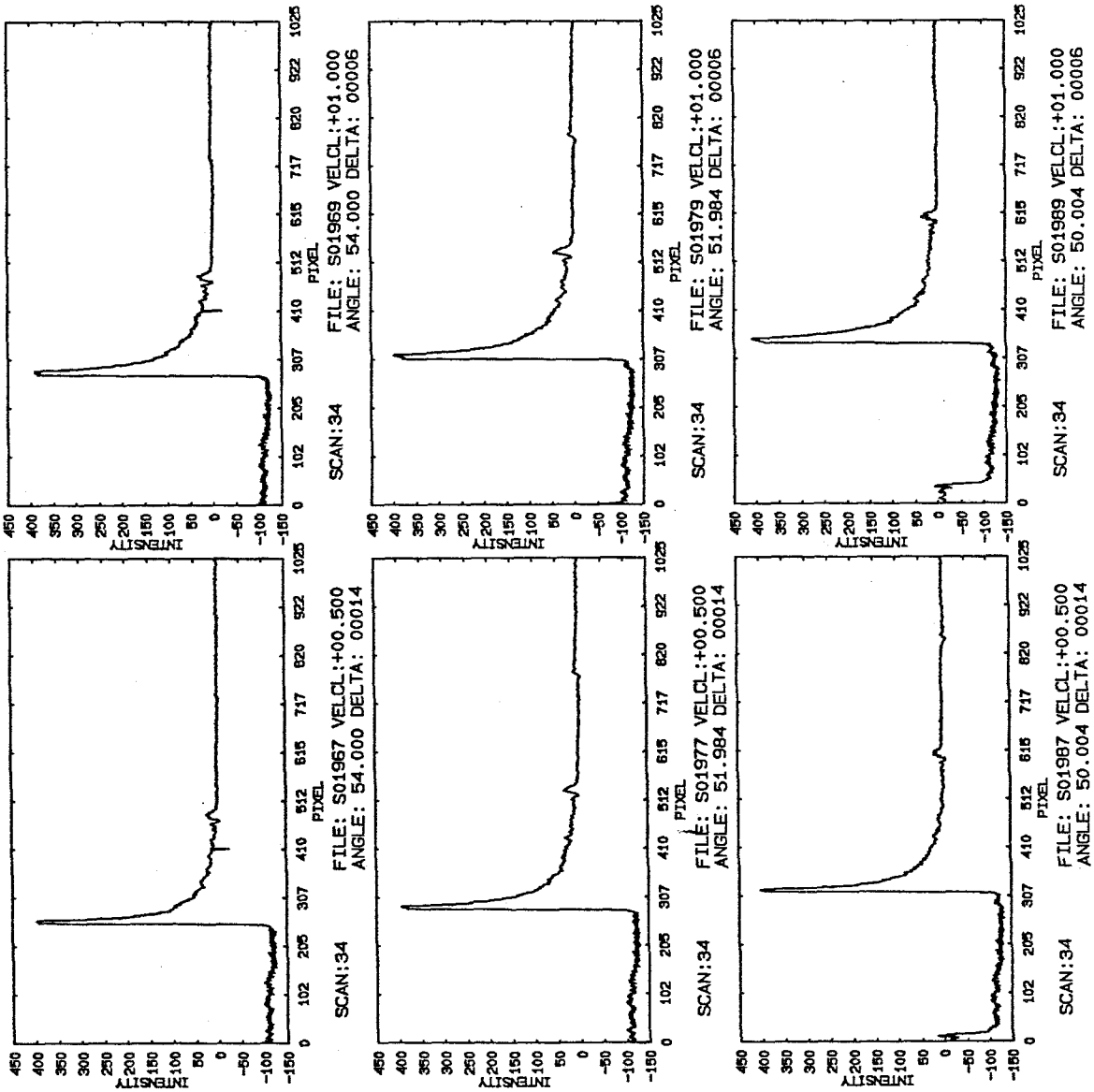
INTENSITY
PIXEL
SCAN:34
FILE: S01967 VELCL:+00.500
ANGLE: 54.000 DELTA: 00014
FILE: S01969 VELCL:+01.000
ANGLE: 54.000 DELTA: 00006
FILE: S01977 VELCL:+00.500
ANGLE: 51.984 DELTA: 00014
FILE: S01979 VELCL:+01.000
ANGLE: 51.984 DELTA: 00006
FILE: S01987 VELCL:+00.500
ANGLE: 50.004 DELTA: 00014
FILE: S01989 VELCL:+01.000
ANGLE: 50.004 DELTA: 00006

Figure 72

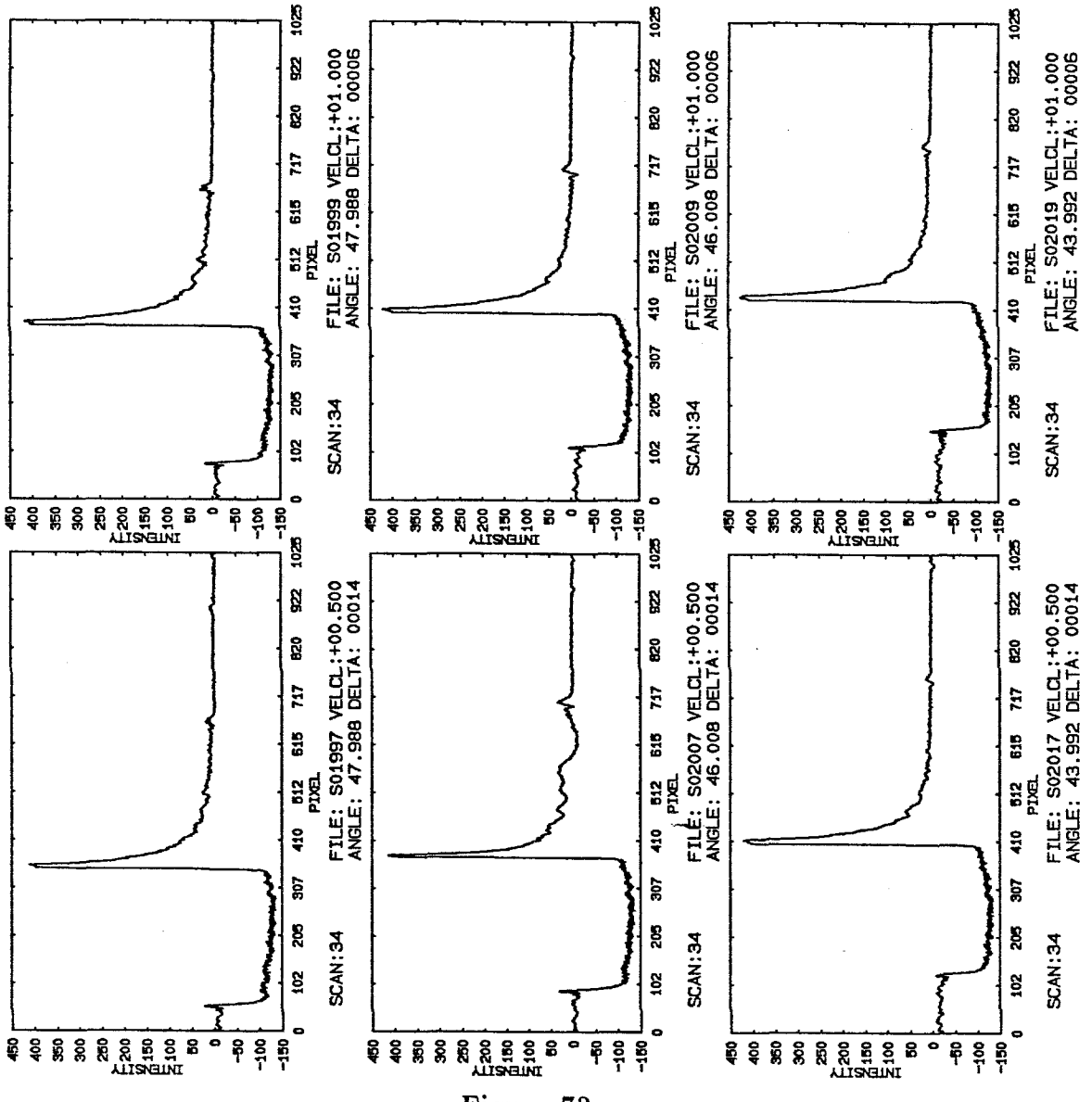
INTENSITY
PIXEL
SCAN:34
FILE: S01997 VELCL:+00.500
ANGLE: 47.988 DELTA: 00014
FILE: S01999 VELCL:+01.000
ANGLE: 47.988 DELTA: 00006
FILE: S02007 VELCL:+00.500
ANGLE: 46.008 DELTA: 00014
FILE: S02009 VELCL:+01.000
ANGLE: 46.008 DELTA: 00006
FILE: S02017 VELCL:+00.500
ANGLE: 43.992 DELTA: 00014
FILE: S02019 VELCL:+01.000
ANGLE: 43.992 DELTA: 00006

Figure 73

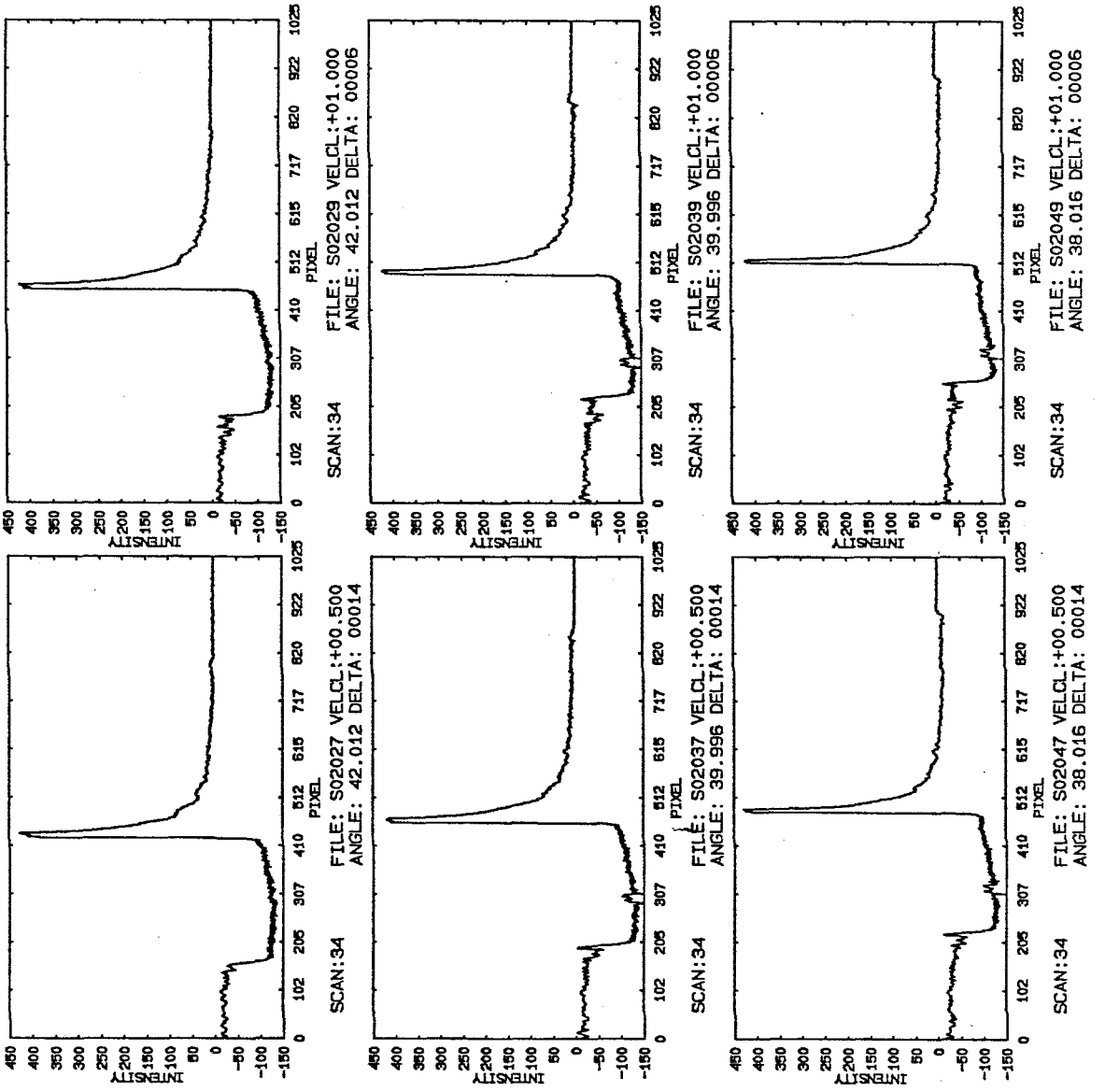
INTENSITY
PIXEL
SCAN:34
FILE: S02027 VELCL:+00.500
ANGLE: 42.012 DELTA: 00014
FILE: S02029 VELCL:+01.000
ANGLE: 42.012 DELTA: 00006
FILE: S02037 VELCL:+00.500
ANGLE: 39.996 DELTA: 00014
FILE: S02039 VELCL:+01.000
ANGLE: 39.996 DELTA: 00006
FILE: S02047 VELCL:+00.500
ANGLE: 38.016 DELTA: 00014
FILE: S02049 VELCL:+01.000
ANGLE: 38.016 DELTA: 00006

Figure 74

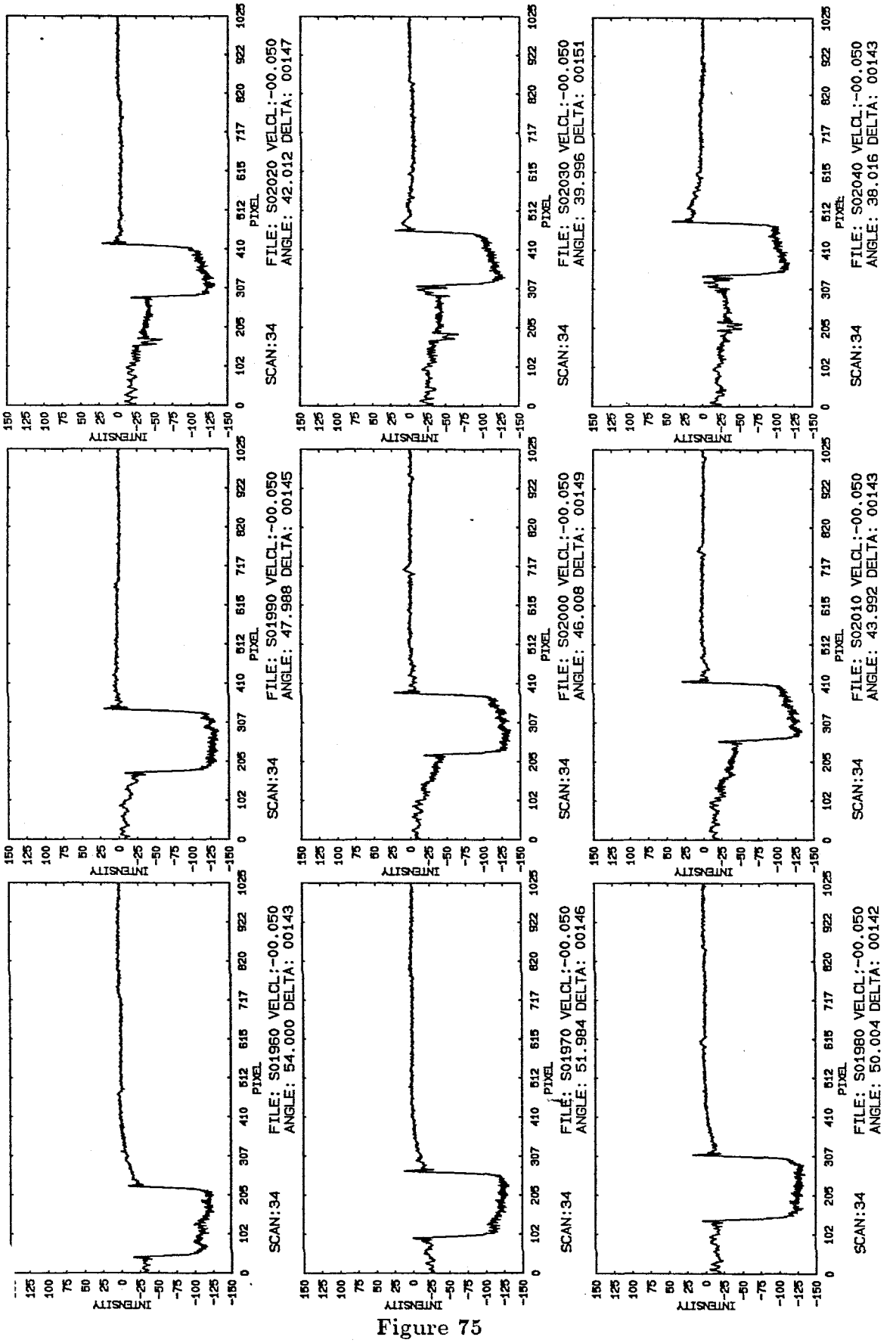
INTENSITY
PIXEL
SCAN:34
FILE: S01960 VELCL:-00.050
ANGLE: 54.000 DELTA: 00143
FILE: S01970 VELCL:-00.050
ANGLE: 51.984 DELTA: 00146
FILE: S01980 VELCL:-00.050
ANGLE: 50.004 DELTA: 00142
FILE: S01990 VELCL:-00.050
ANGLE: 47.988 DELTA: 00145
FILE: S02000 VELCL:-00.050
ANGLE: 46.008 DELTA: 00149
FILE: S02010 VELCL:-00.050
ANGLE: 43.992 DELTA: 00143
FILE: S02020 VELCL:-00.050
ANGLE: 42.012 DELTA: 00147
FILE: S02030 VELCL:-00.050
ANGLE: 39.996 DELTA: 00151
FILE: S02040 VELCL:-00.050
ANGLE: 38.016 DELTA: 00143

Figure 75

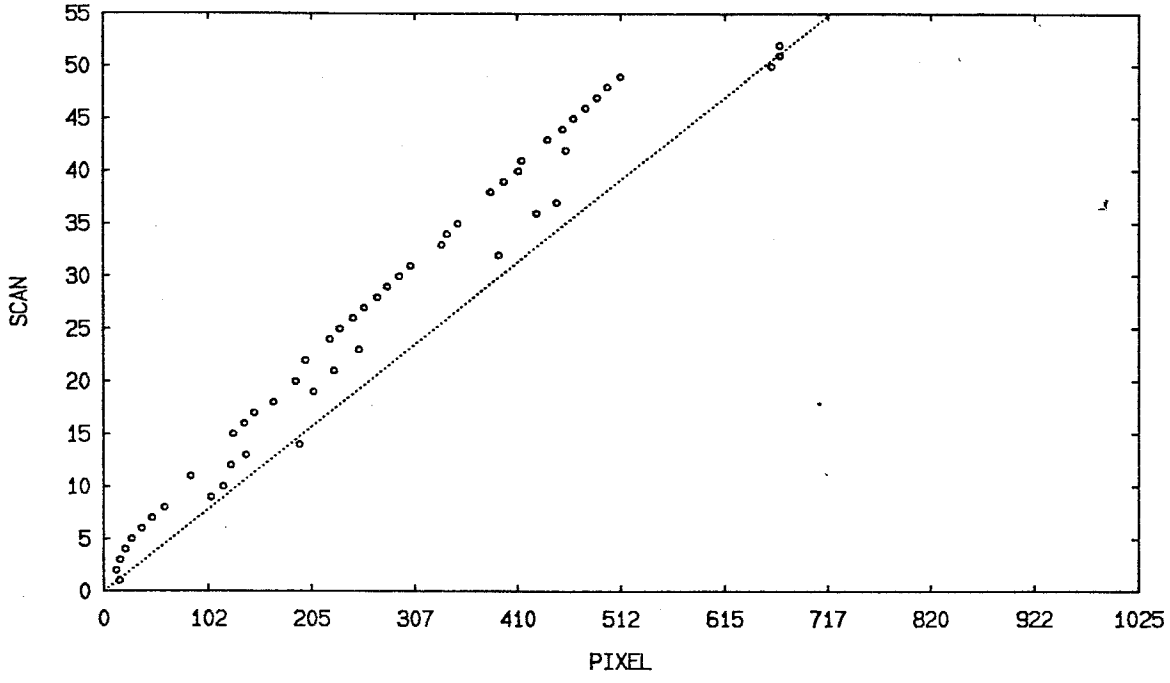

RISE 01-MAR-90 14:44:11 UPR: NONANE LWR: FRMIDE PLATE:29.900
1,52, 1 MOTOR: V00.017 A010.000 D00211633 H- DELAY:00000
FILE: S01990 VELCL:-00.050 ANGLE: 47.988 DELTA: 00145 NUMDEL: 00052

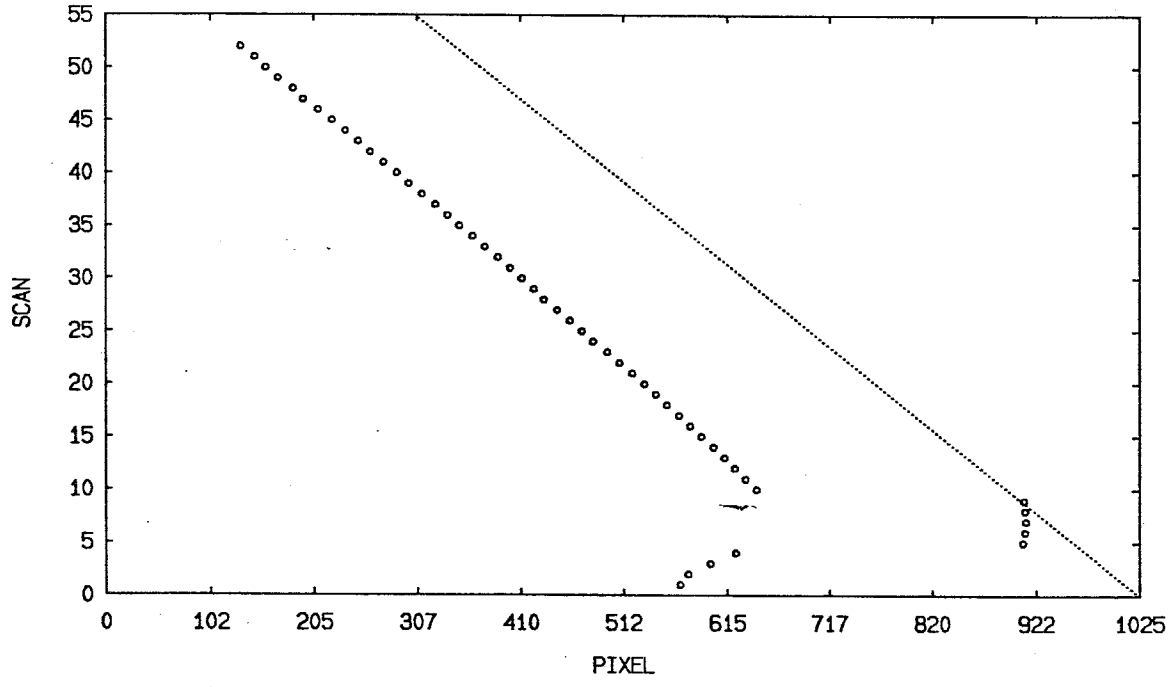

RISE 01-MAR-90 14:44:13 UPR: NONANE LWR: FRMIDE PLATE:29.900
1,52, 1 MOTOR: V00.017 A010.000 D00211633 H+ DELAY:00000
FILE: S01991 VELCL:+00.050 ANGLE: 47.988 DELTA: 00145 NUMDEL: 00052

Figure 76

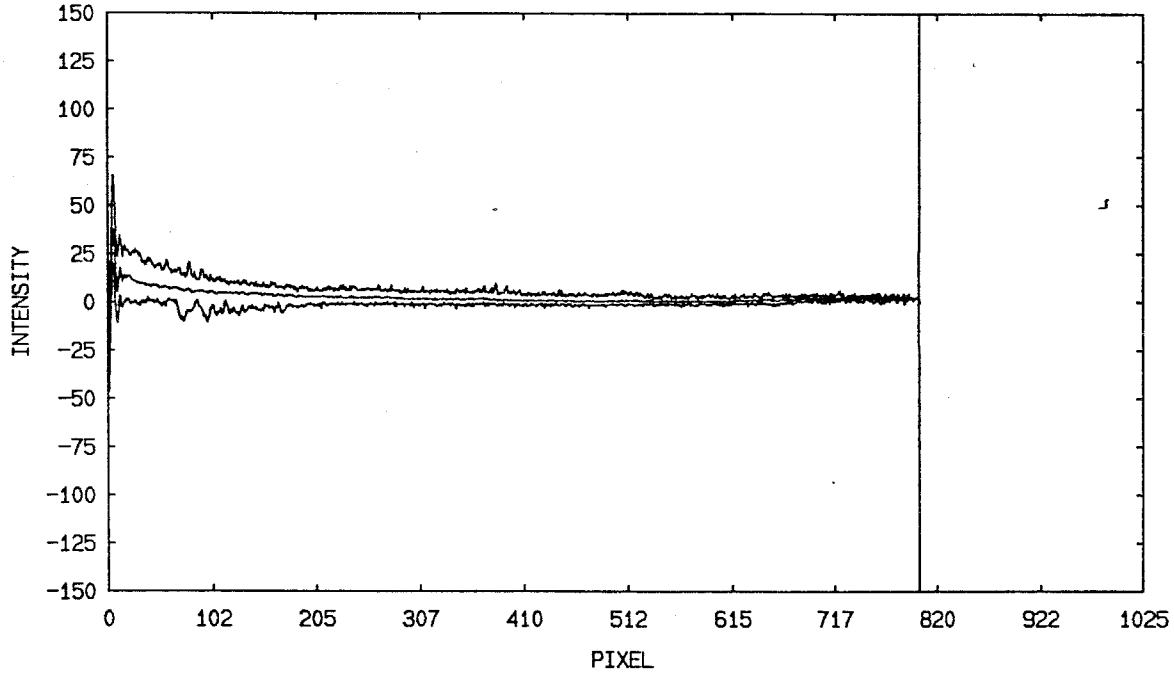

24,31 01-MAR-90 14:44:11 UPR: NONANE LWR: FRMIDE PLATE:29.900
38,39 MOTOR: V00.017 A010.000 D00211633 H- DELAY:00000
44,48 FILE: S01990 VELCL:-00.050 ANGLE: 47.988 DELTA: 00145 NUMDEL: 00052

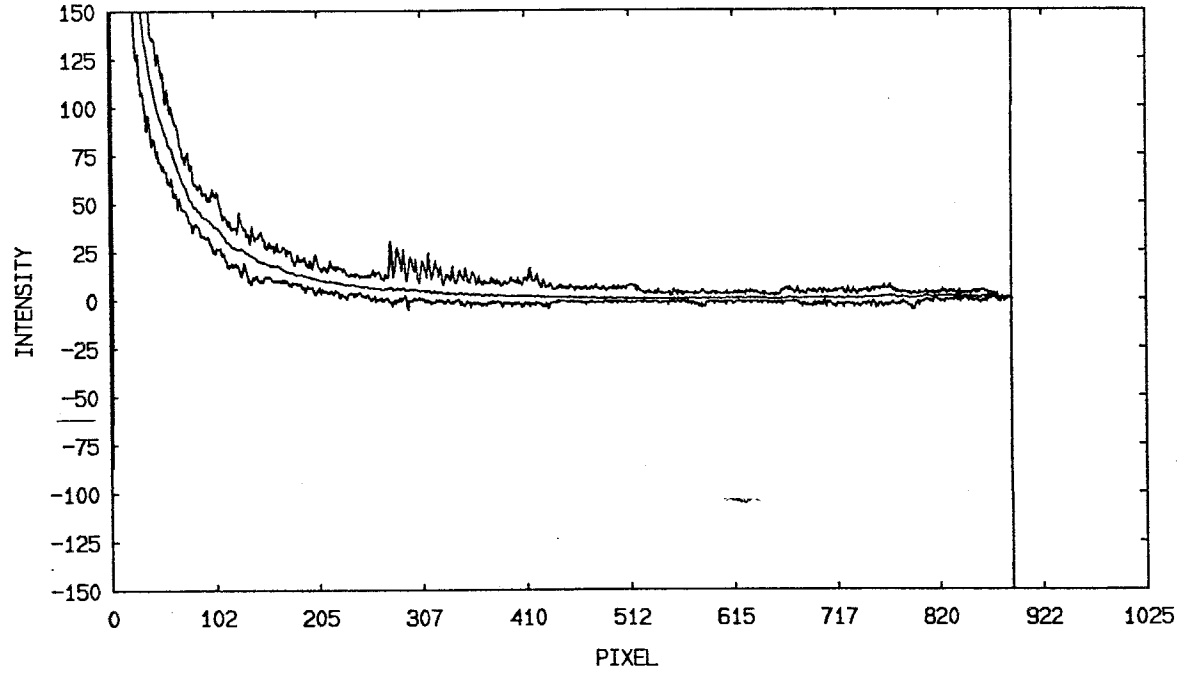

32,52 01-MAR-90 14:44:13 UPR: NONANE LWR: FRMIDE PLATE:29.900
0, 0 MOTOR: V00.017 A010.000 D00211633 H+ DELAY:00000
0, 0 FILE: S01991 VELCL:+00.050 ANGLE: 47.988 DELTA: 00145 NUMDEL: 00052

Figure 77

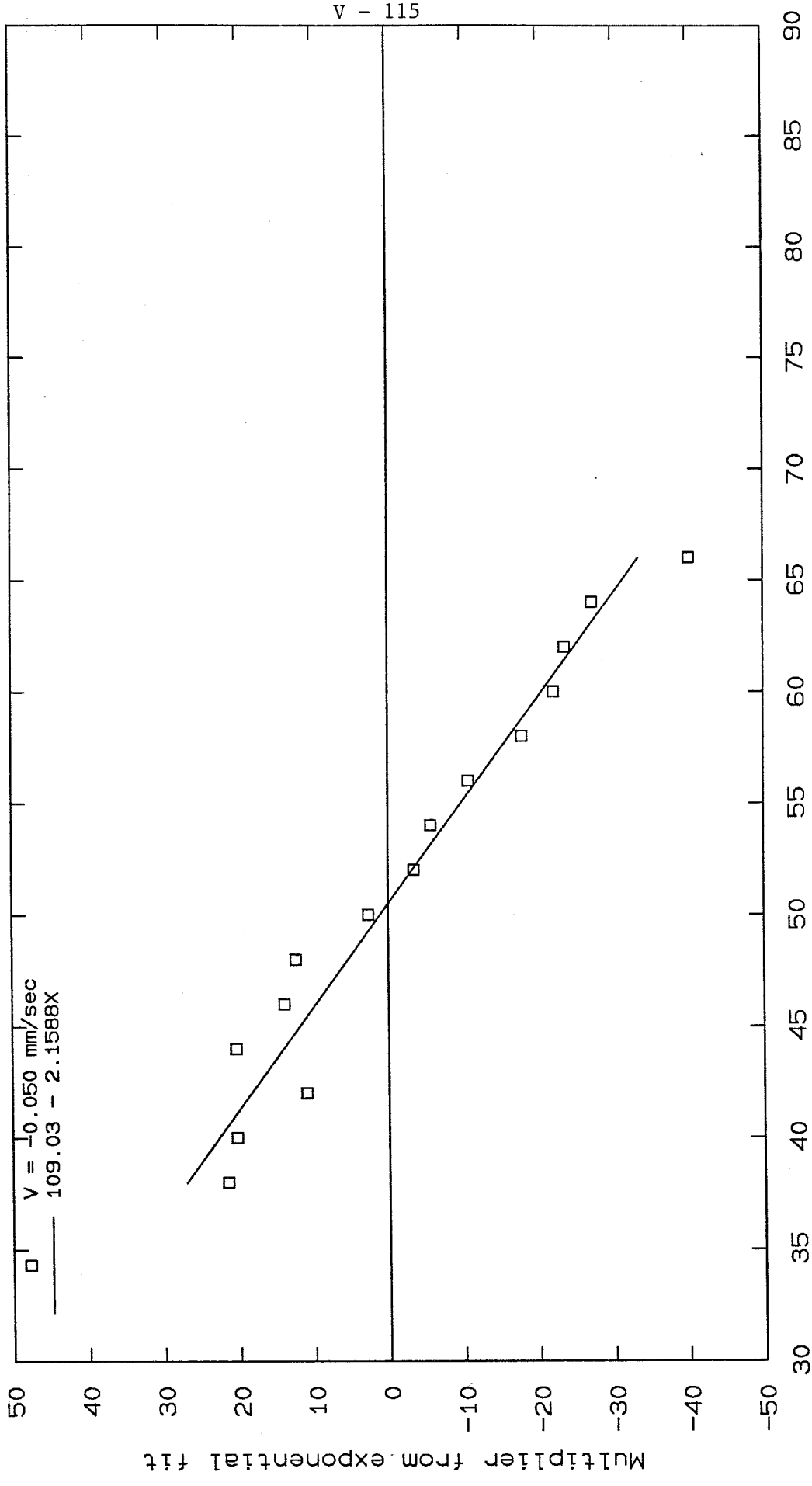

Figure 78 Multiplier from exponential fit vs. plate angle for receding velocities

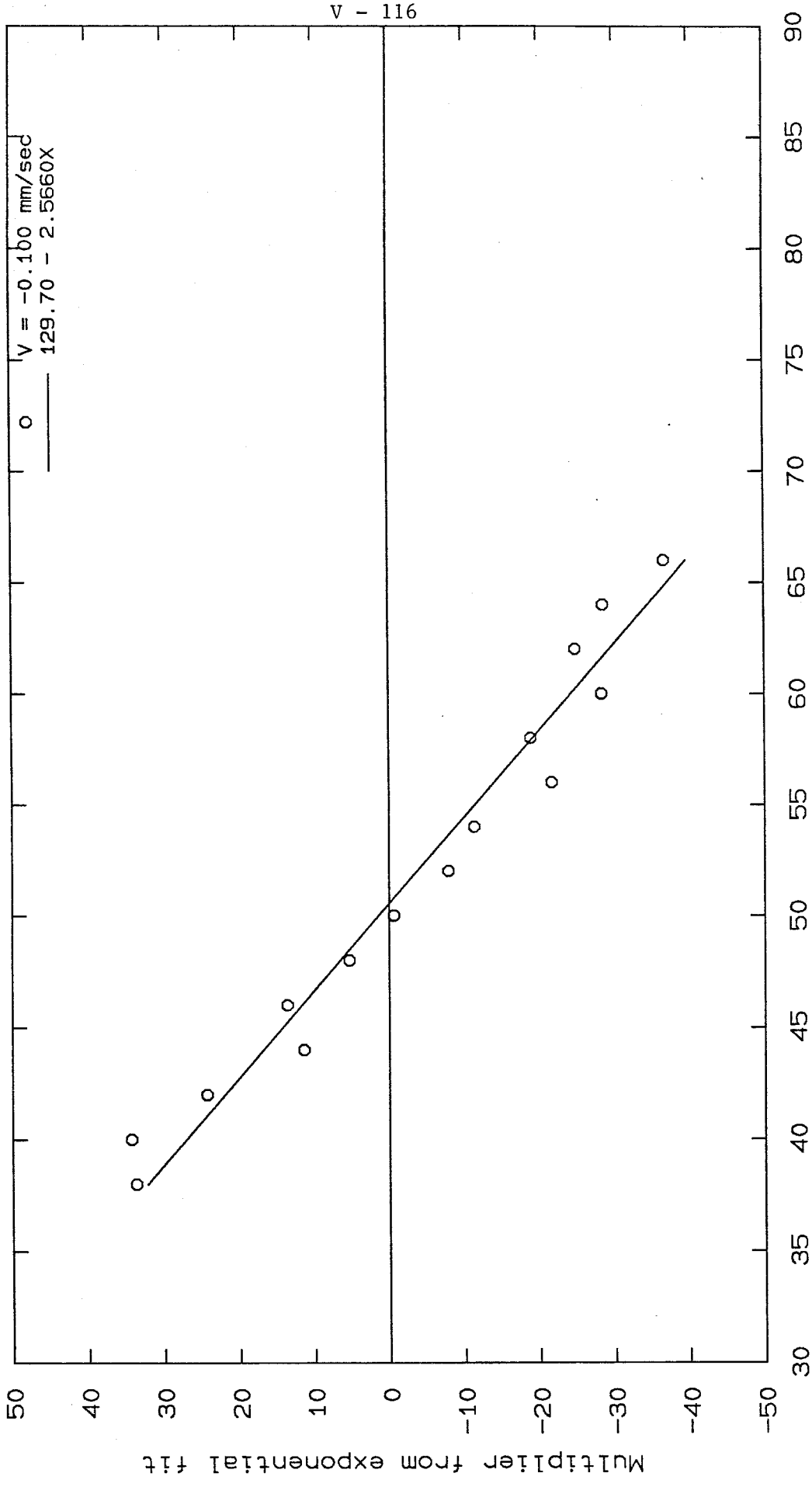

Figure 79 Multiplier from exponential fit vs. plate angle for receding velocities

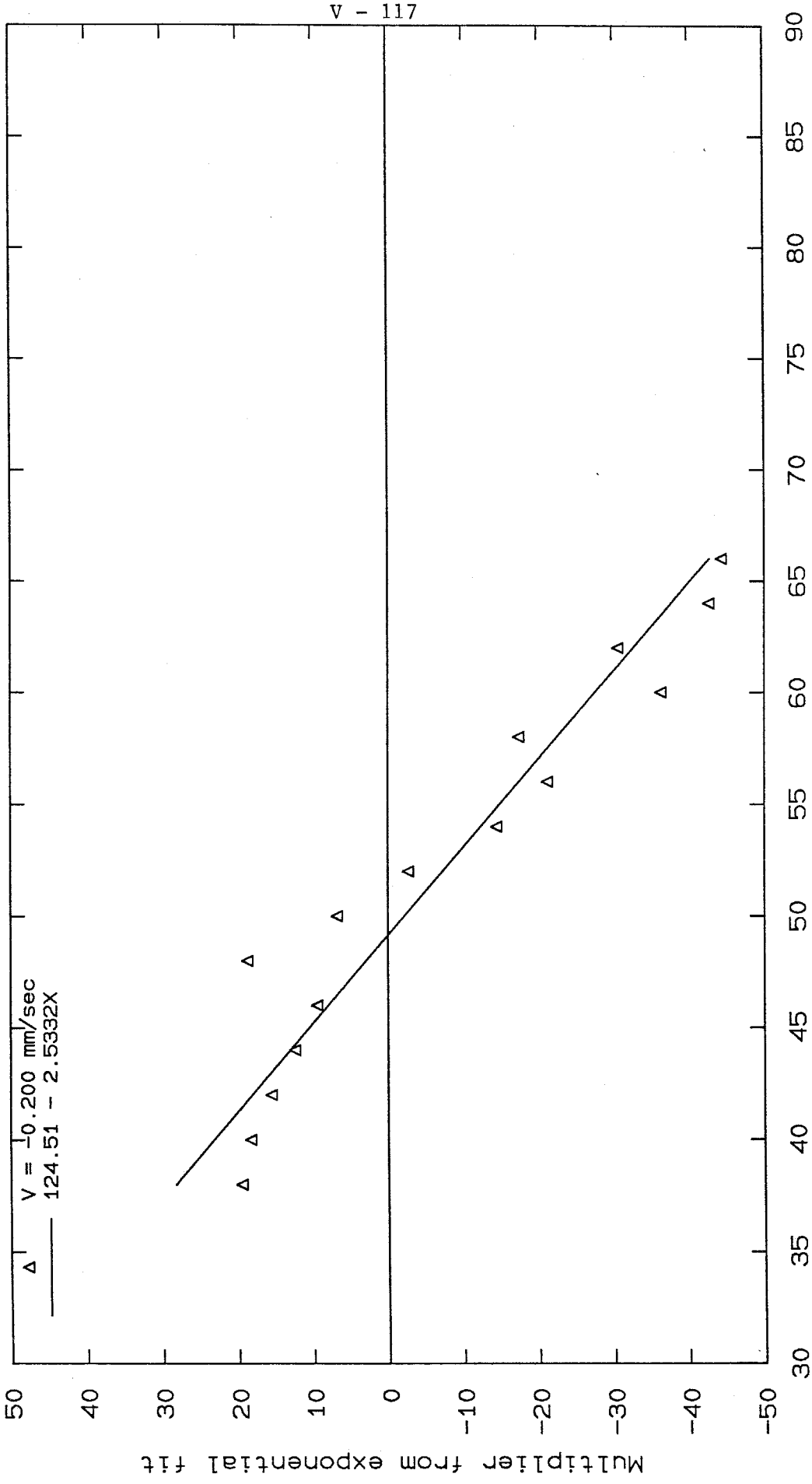

Figure 80 Multiplier from exponential fit vs. plate angle for receding velocities

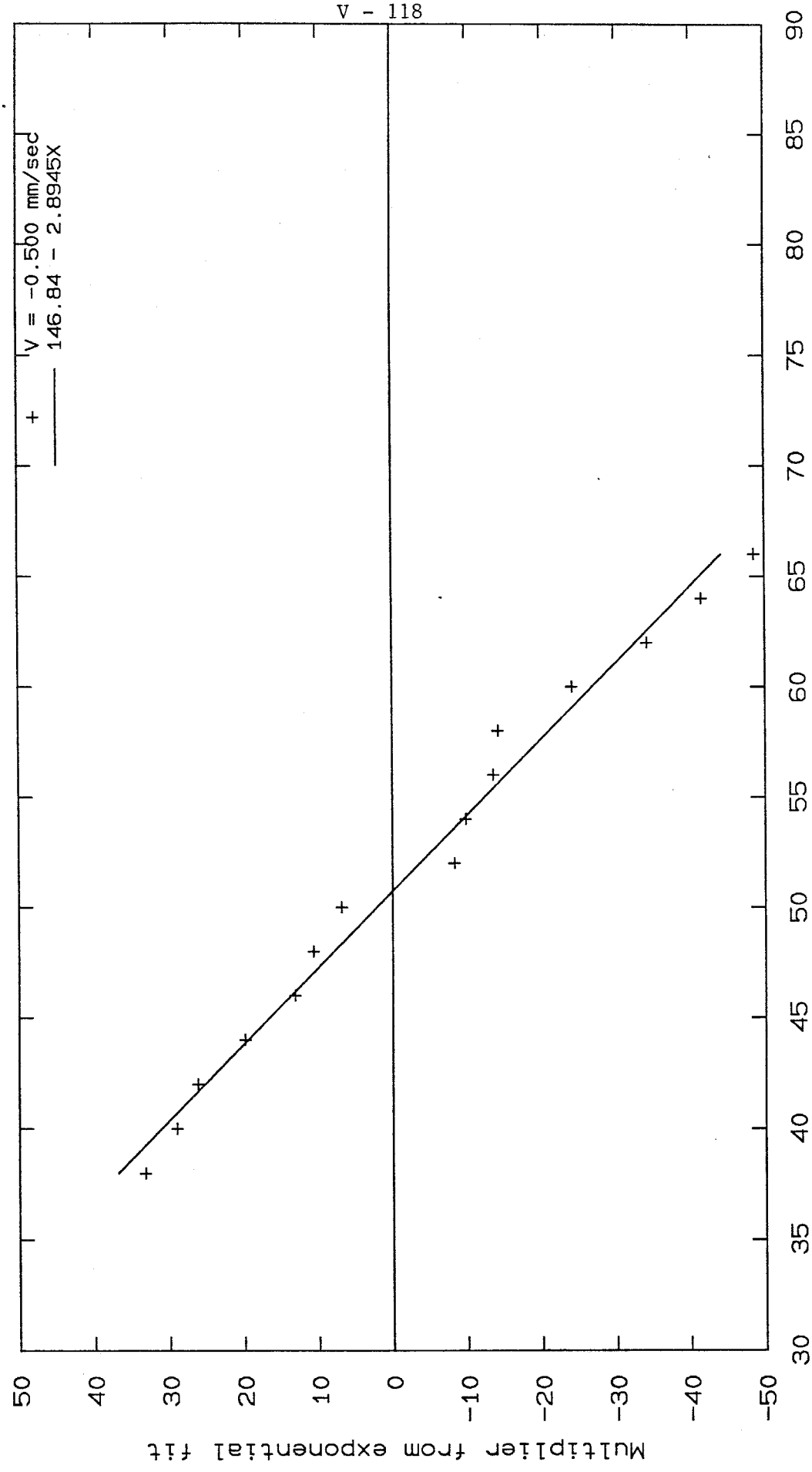

Figure 81 Multiplier from exponential fit vs. plate angle for receding velocities

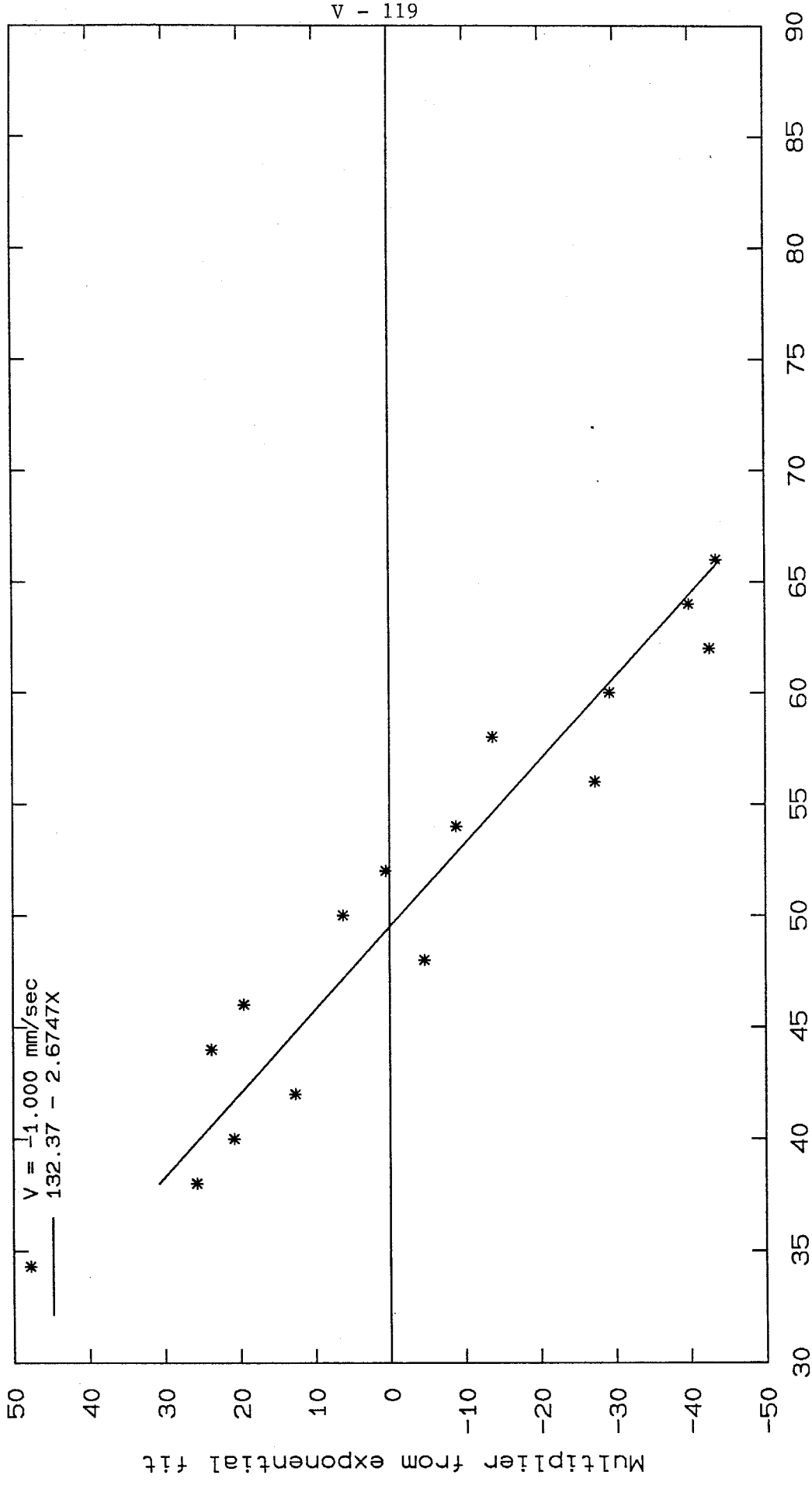

Figure 82 Multiplier from exponential fit vs. plate angle for receding velocities

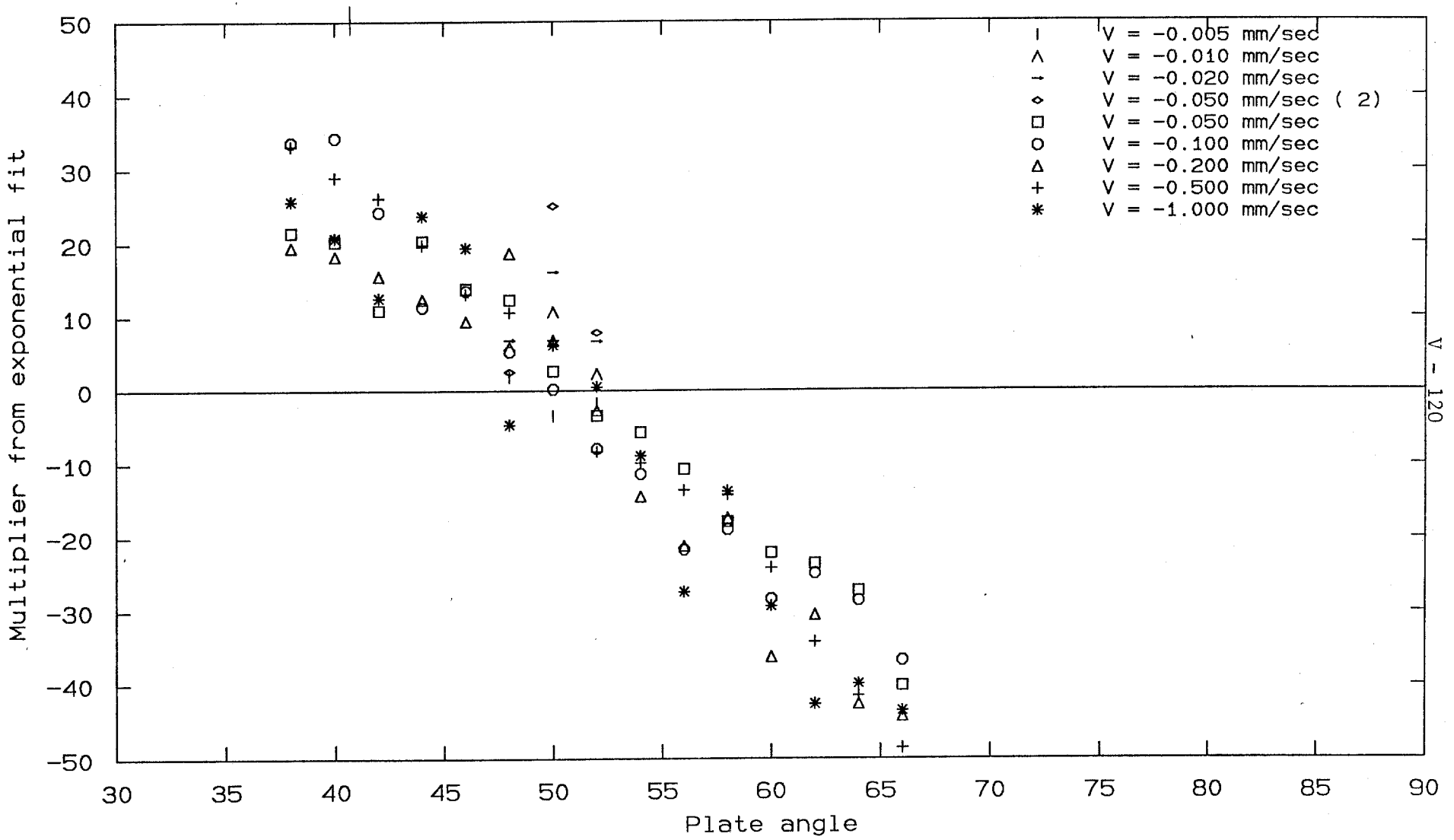

Figure 83 Multiplier from exponential fit vs. plate angle for receding velocities

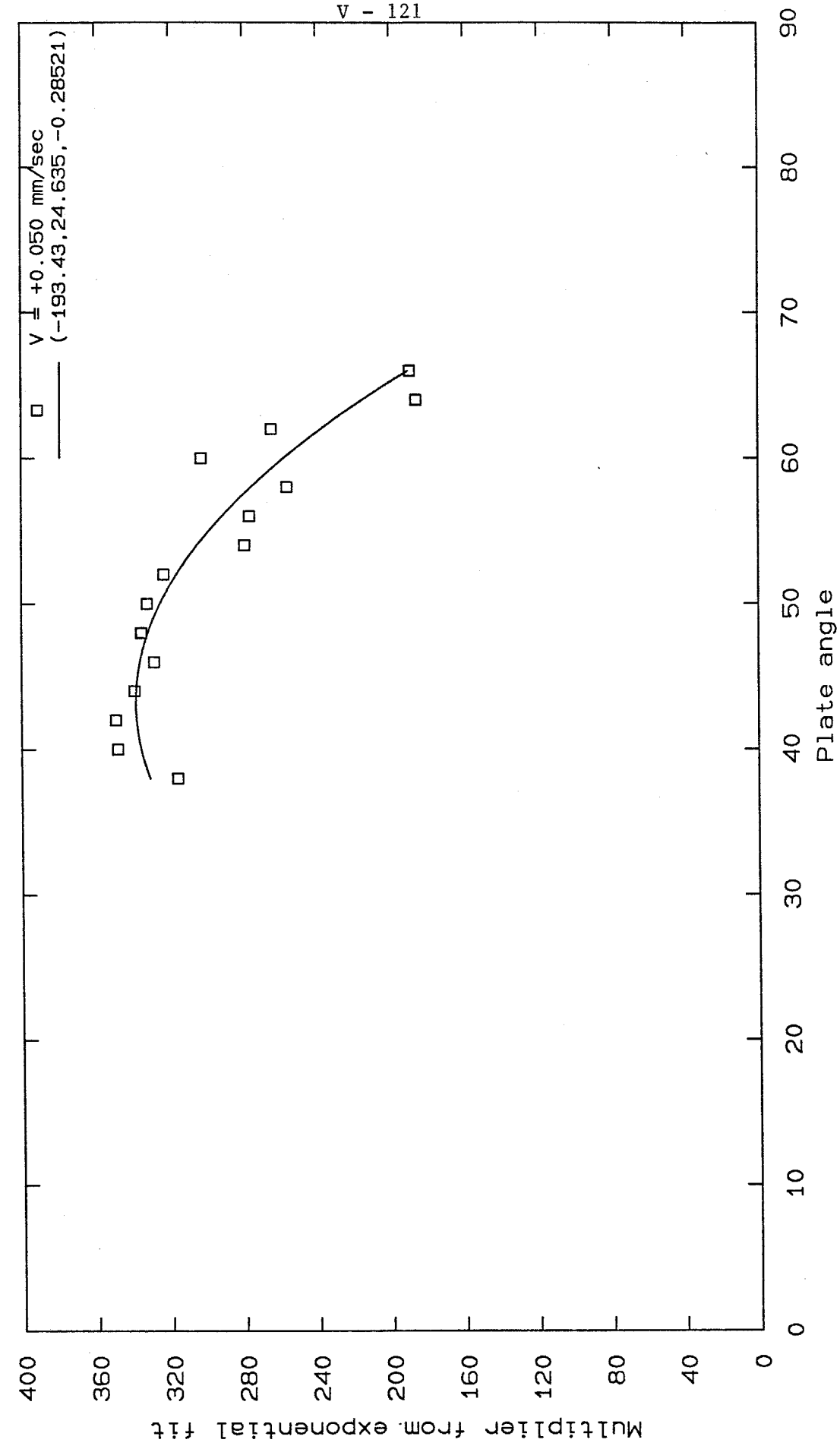

Figure 84 Multiplier from exponential fit vs. plate angle for advancing velocities

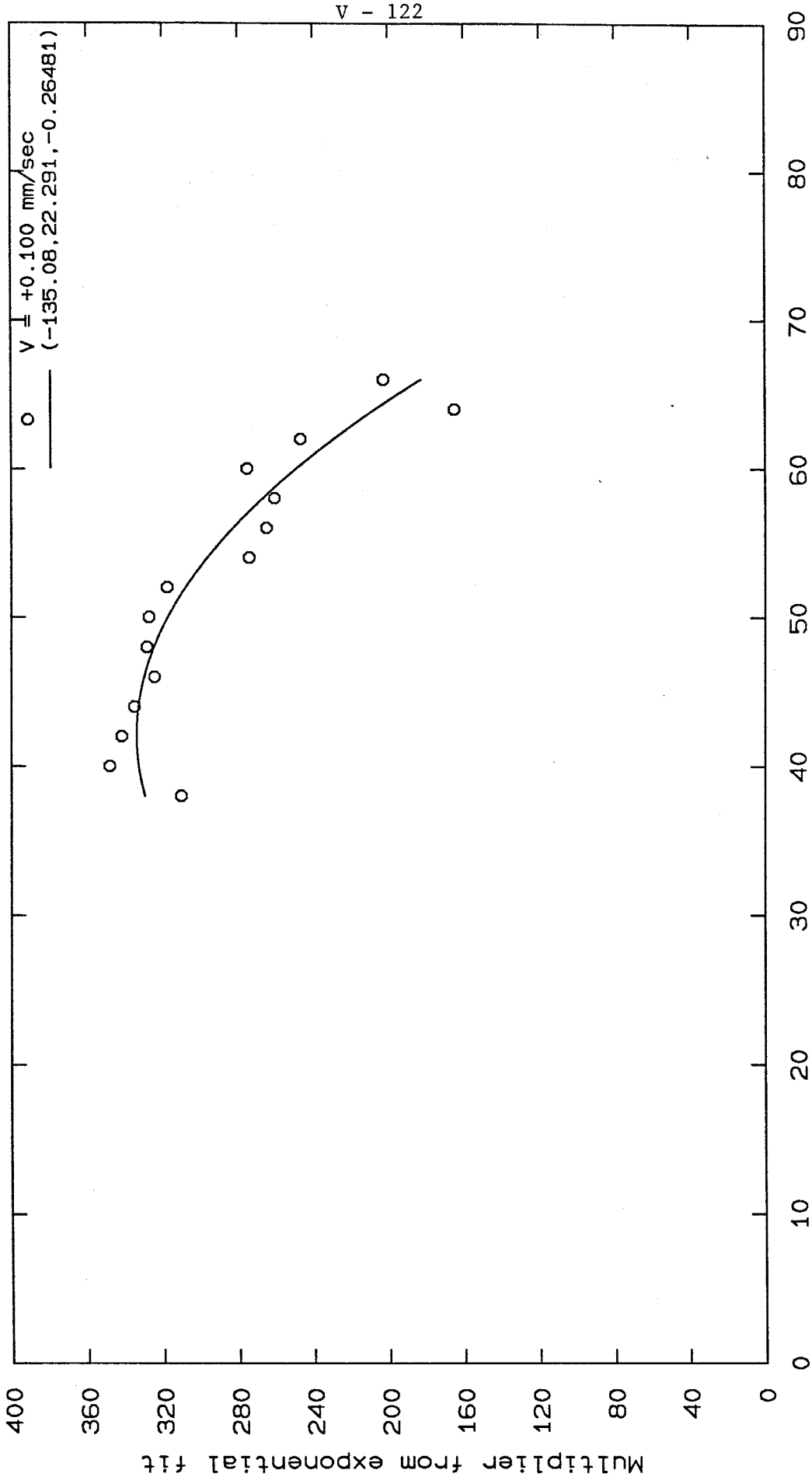

Figure 85 Multiplier from exponential fit vs. plate angle for advancing velocities

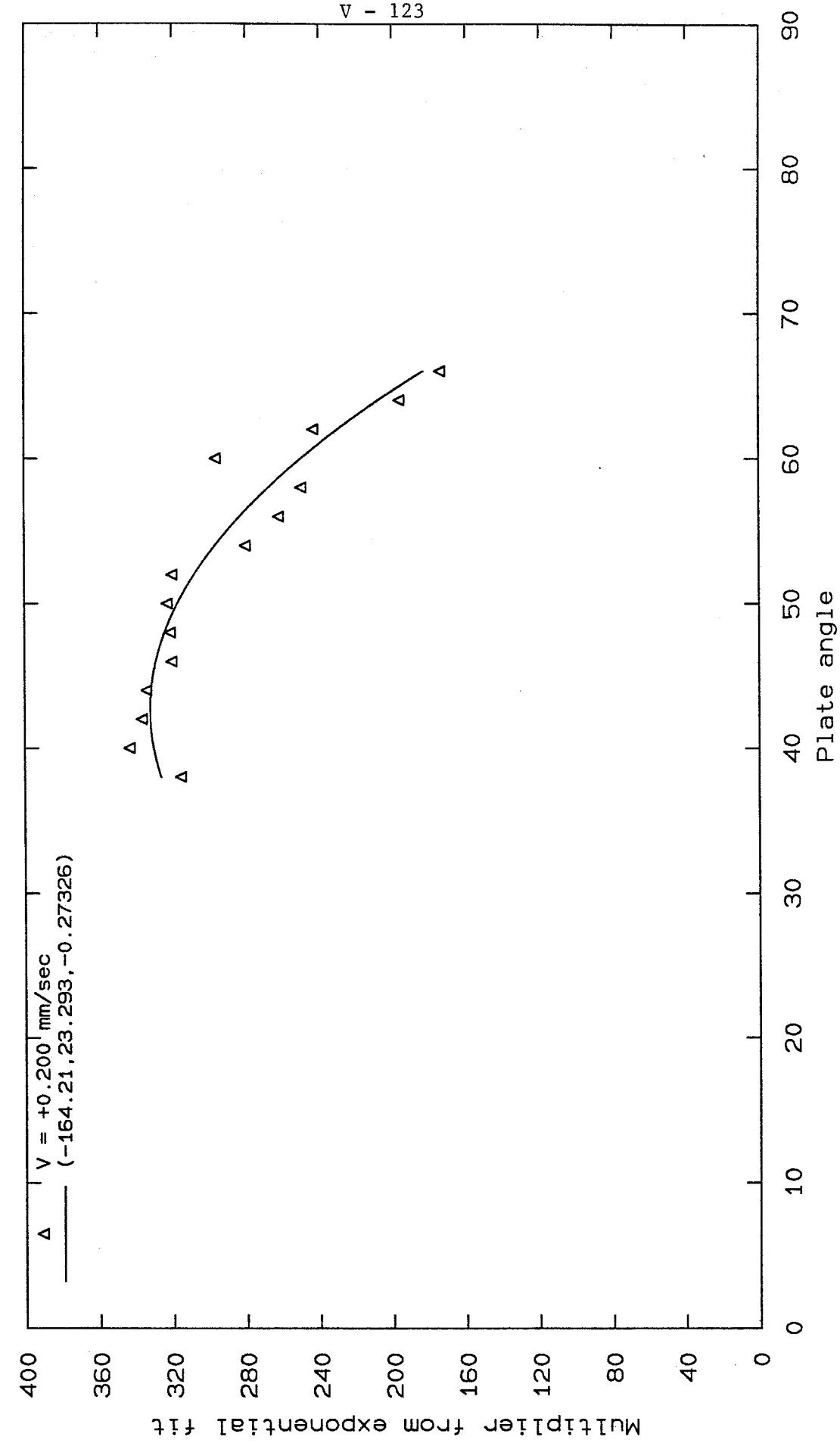

Figure 86 Multiplier from exponential fit vs. plate angle for advancing velocities

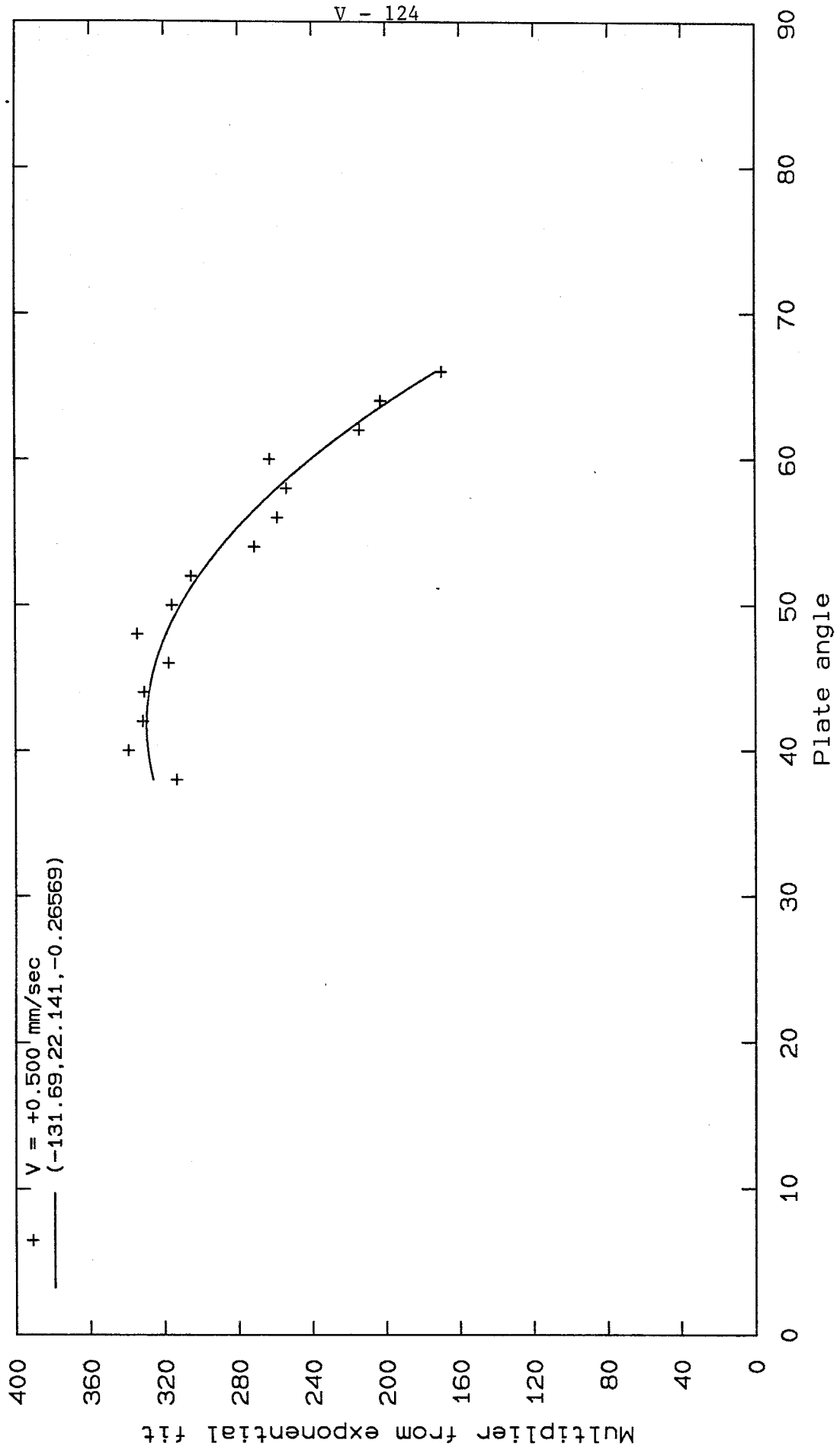

Figure 87 Multiplier from exponential fit vs. plate angle for advancing velocities

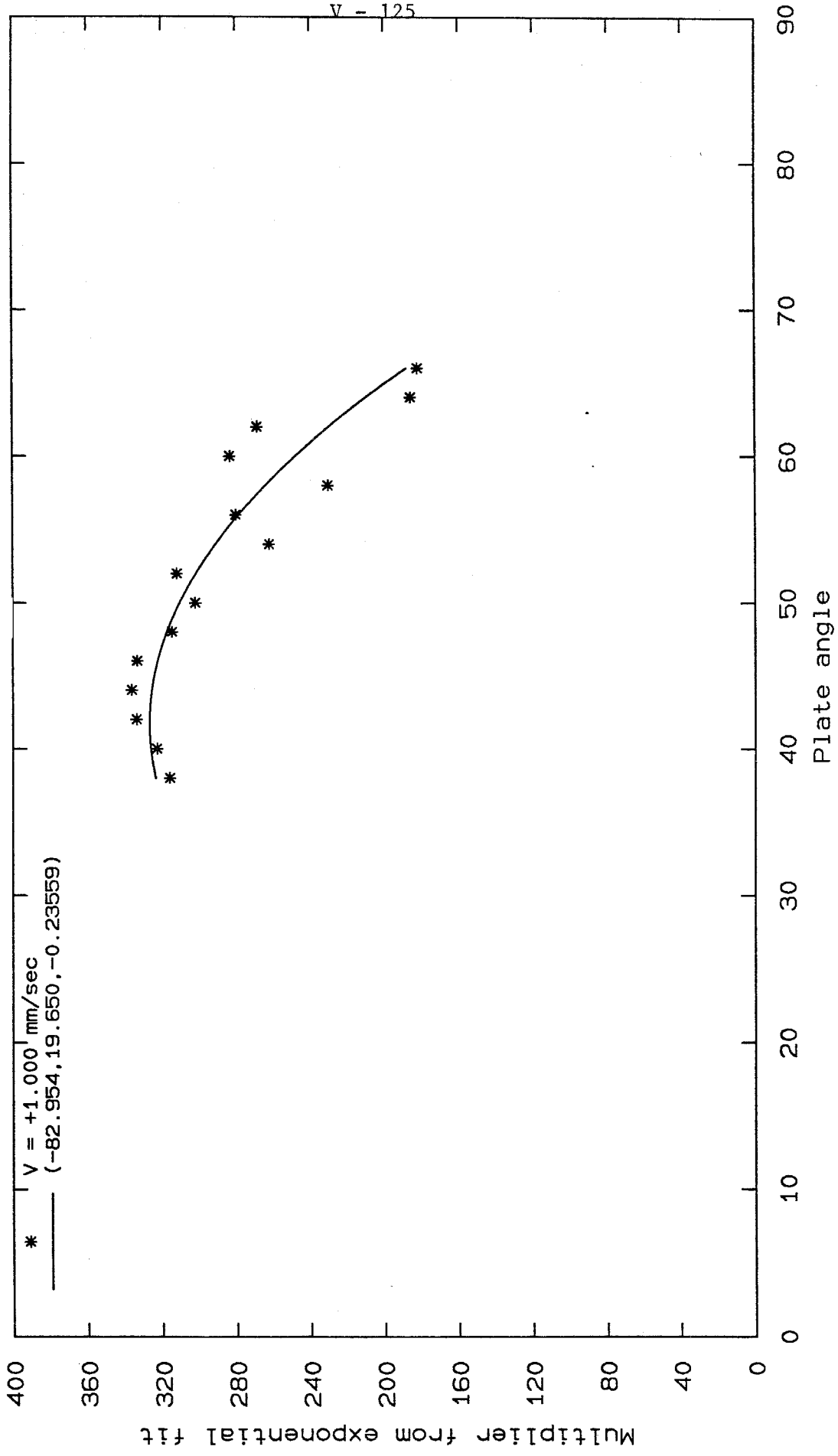

Figure 88 Multiplier from exponential fit vs. plate angle for advancing velocities

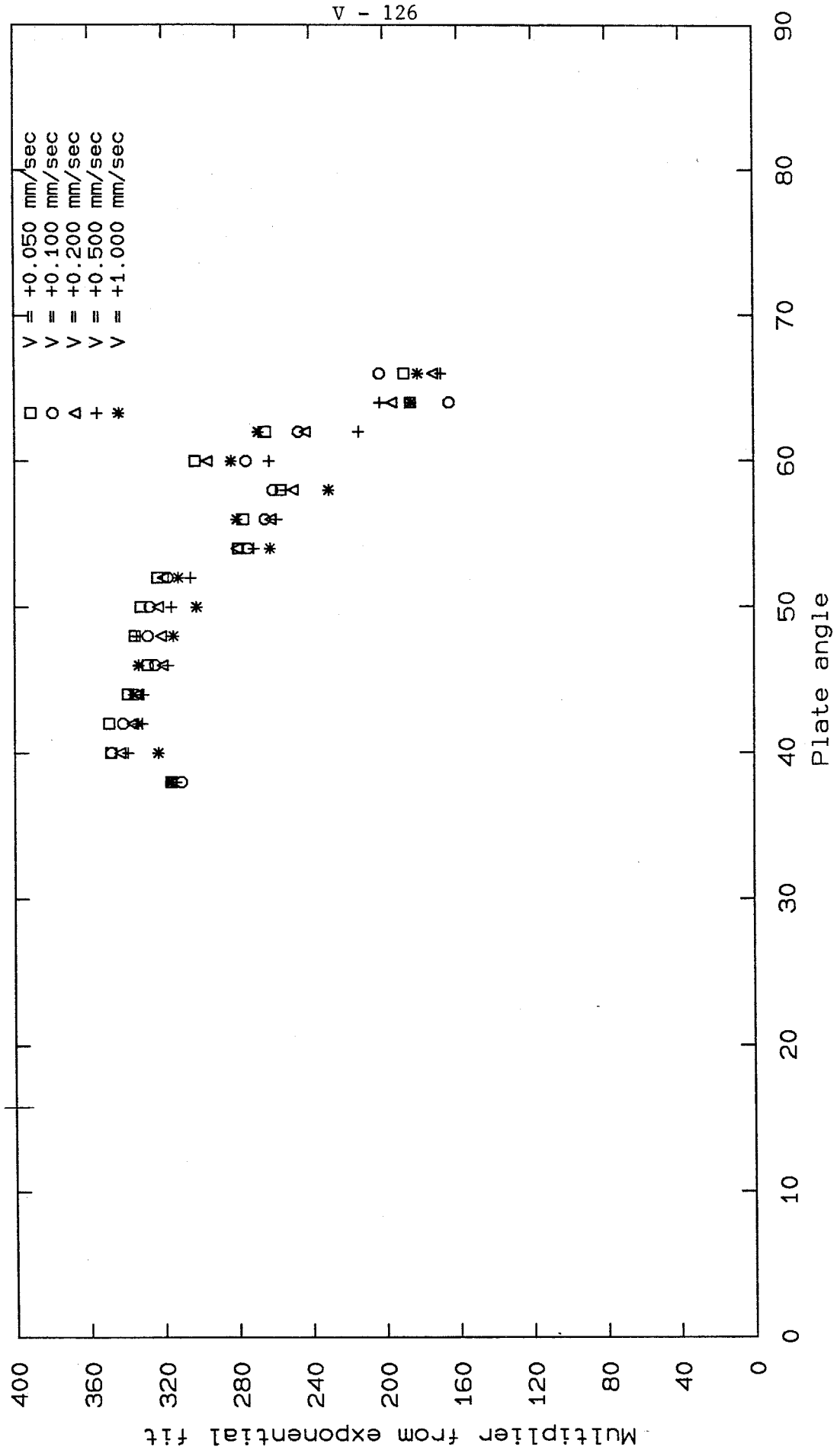

Figure 89 Multiplier from exponential fit vs. plate angle for advancing velocities

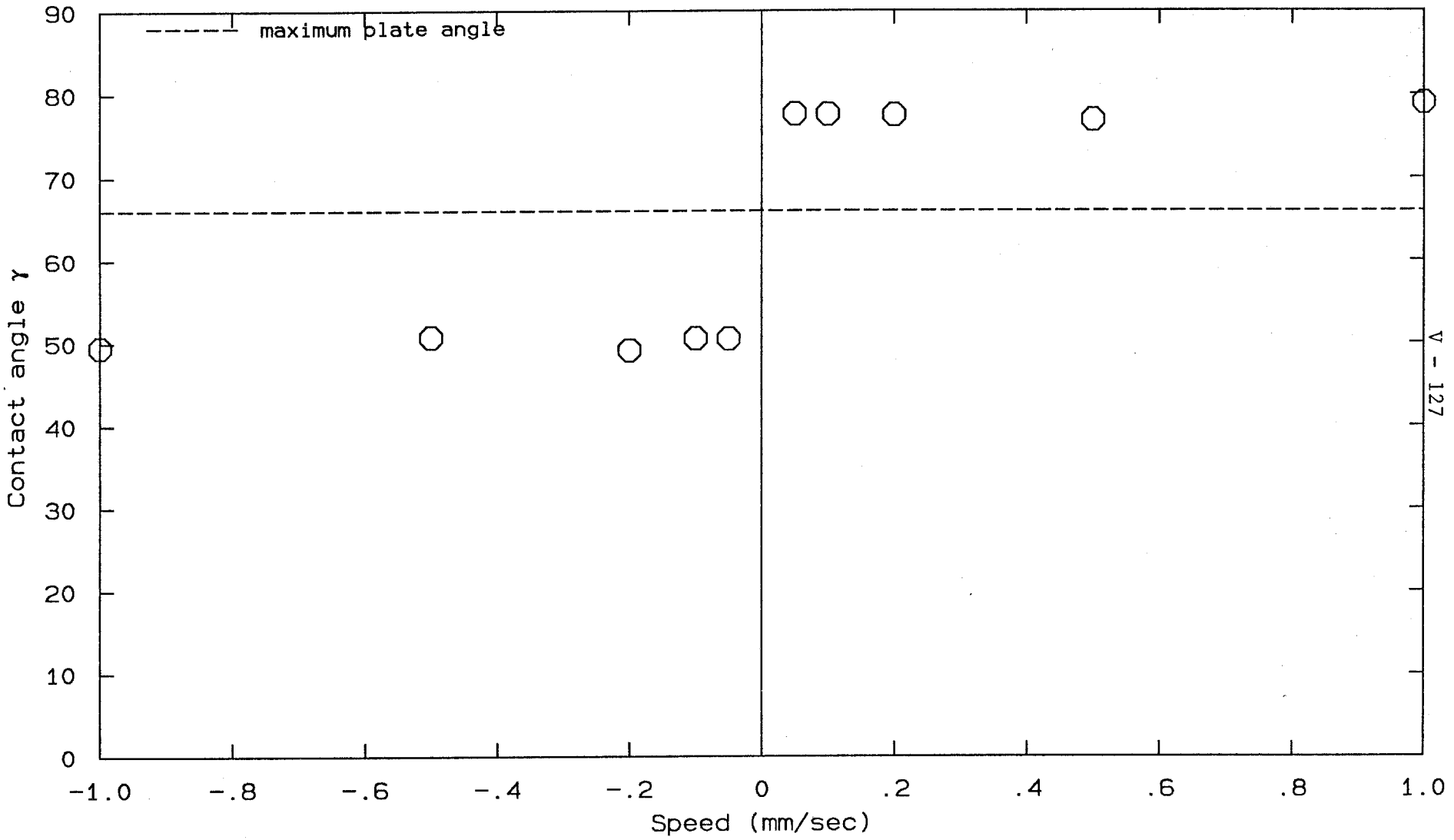

Figure 90
Contact angle vs. velocity for nonane/formamide (glass plate soaked in nonane)